Interference Between Majorana States in the "Neutrinoless Double Beta Decay" at Colliders

Phenomenology of Heavy Neutral Leptons

September 2022

Author **Jonathan Schubert**
Supervisor **Assoc. Prof. Oleg Ruchayskiy**

A Thesis submitted in partial fulfilment of the requirements for the degree of Master of Science

UNIVERSITY OF COPENHAGEN

FACULTY OF SCIENCE

NIELS BOHR INSTITUTE

Interference Between Majorana States in the "Neutrinoless Double Beta Decay" at Colliders

Phenomenology of Heavy Neutral Leptons

Abstract Heavy neutral leptons (HNLs) are hypothetical particles able to explain several puzzles of fundamental physics, chiefly neutrino oscillations. Being *sterile* with respect to Standard Model interactions, these particles admit Majorana masses. This mass term allows for processes violating the Standard Model lepton number. Hence, such processes become a "smoking gun" signature of HNLs, pursued by many experiments. In this work we demonstrate that if HNLs are the sole origin of neutrino masses, destructive interference between Majorana states suppresses the same sign di-lepton signal at colliders. In the phenomenologically interesting case of large HNL couplings, such a suppression stems from mutually cancelling contributions of several HNLs akin to their contributions to neutrino masses. Nevertheless, the signal can be much larger than naively expected. We also identify parts of the parameter space of such realistic HNL models where the lepton number violating signal is maximised at the Large Hadron Collider and Future Circular Collider (LHC) in the hadron-hadron phase (FCC-hh). Our results are obtained within the effective W approximation which allows for analytic treatment and gives clear dependence on the model parameters. Subsequently, they are rescaled to detector level Montecarlo simulations. For the LHC, the parameter bounds on the HNL's mixing to the Standard Model leptonic sector expected from our results are not competitive with Electroweak Precision Tests, improving only slightly on other collider based searches. For the FCC-hh we find a potential improvement on indirect bounds for HNLs with masses in the TeV range, with strong improvement on other collider based searches. Although approximate, our results are expected to be good estimates of discovery potential. Exact exclusion limits on HNL parameters warrant further investigation.

Jonathan Schubert
Msc. in Particle Physics, September 2022
Supervisor: Assoc. Prof. Oleg Ruchayskiy

University of Copenhagen
Faculty of Science
Niels Bohr Institute
Blegdamsvej 17
2100 København Ø

Acknowledgements

First and foremost, I would like to express my sincere gratitude to my supervisor Oleg Ruchayskiy, without whom this thesis would not have been possible; not only for his instrumental guidance and helpful advice with respect to the topic, but also for his insights into the world of research as a whole. I will be sure to take the almost proverbial pieces of candid wisdom making up the "Ruchayskiy guide to research" with me on my future path. Thank you for a stimulating year under your tutelage.

I would like to extend my thanks to Inar Timiryasov and Kevin Urquía Calderón from the HNL phenomenology group at NBI for many fruitful discussions on the topic of this thesis and other subjects.

Further, I would like to acknowledge the constructive comments by Richard Ruiz and Benjamin Fuks on the analysis presented in this thesis.

Thanks also go to my office mates Katinka Wandall-Christensen, Marie-Louise Riis, Edis Tireli and Mads Hyttel for bouncing off ideas randomly popping up and the good vibes. An extra big thank-you to my friends Mathias Labonte and Arnau Morancho Tarda for making sure we take enough coffee breaks to 'stay productive'.

Finally, I would like to express my profound gratitude to Maria Sadlik for her encouragement and her invaluable presence in my life, and to my parents for their unwavering support and unconditional love. I cannot begin to verbalise the impact you have had on this work.

Contents

Introduction

1

At the time of writing this thesis, the Standard Model of particle physics is the most fundamental well-established theory describing our universe on the smallest scales. Despite the phenomenal success the Standard Model has had in predicting experimentally confirmed high energy physics phenomena, there are a number of *observed* phenomena that it can not explain. Among the most stark of these shortcomings are

1. Neutrino oscillations
2. Baryon asymmetry of the universe
3. Dark matter
4. Inflation of the early universe
5. Dark energy
6. Gravity

In order to explain these phenomena, many extensions to the Standard Model have been forwarded. One of these with the potential to explain at least points 1–3 of the shortcomings listed above is the introduction of *heavy neutral leptons*.[1]

There is currently a plethora of experimental efforts underway aiming at the discovery of this class of particles. While there are some theoretical considerations at what energy scales these ultra-weakly interacting particle could be produced, the parameter space is fairly unrestricted. As direct detection experiments are restricted in their maximal production energy, researchers are looking to processes in which heavy neutral leptons contribute or interact *virtually*. In such processes they hope to find traces of heavy neutral leptons with *masses above the electroweak scale*. One of such *indirect processes* is the equivalent of the *neutrinoless double beta decay at high energy hadron colliders*.

The goal of this thesis is to describe this process in a neutrino theory that can be reconciled with existing experimental neutrino data. Furthermore, it aims at highlighting the importance of assuming realistic neutrino scenarios when analysing *indirect processes* in general.

[1] The νMSM discussed in Section 1.2.3 also promises to explain inflation with the Standard Model Higgs as the inflaton.

1.1 Standard Model

Before diving into the theory behind heavy neutral leptons and how they fit into the Standard Model, this section is meant to give a brief summary of the framework in which this extension would be embedded. The following brief overview will take inspiration from much more profound introductions to the topic [1, 2].

1.1.1 General Structure

The Standard Model of particle physics (SM, also known as the Glashow-Weinberg-Salam model) was first formulated in the framework of quantum field theory in the 1960s [3–5]. With the discovery of the Higgs boson in 2011 [6, 7], all predicted particles of the SM have been experimentally confirmed, and predicted values have been met with exceptional accuracy.[2] The SM is the result of decades of research in particle physics culminating in this description of all known forces — with the exception of gravity — in a quantum field gauge theory.

In a nutshell, the Standard Model can be divided into three subcategories:

- Fermionic matter content of quarks (q), leptons (ℓ), neutrinos ($\nu_{(\ell)}$)[3]
- Force mediating gauge bosons (gluon g, photon γ, weak force mediators W, Z)
- Higgs boson h responsible for generating SM masses through *Higgs mechanism*

The well known graphic representation of this is shown on the left panel of Fig. 1.2.

Standard Model Lagrangian

More *fundamentally*, the model is described by the non-abelian (Yang-Mills [10]) $SU(3)_c \times SU(2)_\mathrm{L} \times U(1)_\mathrm{Y}$ gauge group. The $SU(3)_c$ part describes quantum chromodynamics (QCD), while $SU(2)_\mathrm{L} \times U(1)_\mathrm{Y}$ describes the *electroweak sector*. The interaction — and self interaction — of the associated gauge fields in this theory are described by the Lagrangian

$$\mathcal{L}_\mathrm{gauge} = -\frac{1}{4} G^{i\mu\nu} G^i_{\mu\nu} - \frac{1}{4} W^{j\mu\nu} W^j_{\mu\nu} - \frac{1}{4} B^{\mu\nu} B_{\mu\nu}, \tag{1.1}$$

[2] However, a few notable anomalies — that we will not cover in detail in this work — have been recently raised in the electroweak sector (namely $(g_\mu - 2)$ at Fermilab [8] and W mass at CDF [9]) further highlighting the fact that the model is not yet complete beyond doubt.

[3] When necessary we will distinguish between up-like $u_\alpha \leftrightarrow$ (up, charm, top) and down-like $d_\alpha \leftrightarrow$ (down, strange, bottom) quarks.

with an implicit summation over i and j. Here, $G^{i\mu\nu}$ $(SU(3)_c)$, $W^{i\mu\nu}$ $(SU(2)_\mathrm{L})$ and $B^{\mu\nu}$ $(U(1))_\mathrm{Y})$ are the fields in the adjoint representation

$$\begin{aligned} G^{i\mu\nu} &= \partial^\mu G^{i\nu} - g_s f_{ijk} G^{j\mu} G^{k\nu} \\ W^{i\mu\nu} &= \partial^\mu W^{i\nu} - g\varepsilon_{ijk} W^{j\mu} W^{k\nu} \\ B^{\mu\nu} &= \partial^\mu B^\nu - \partial^\nu B^\mu \end{aligned} \tag{1.2}$$

with $G^{i\mu}$, $W^{i\mu}$,and B^μ being the fields in the fundamental representations, while g_s (f) and g (ε) are the respective coupling (structure) constants of strong $(SU(3)_c)$ and electroweak $(SU(2)_\mathrm{L})$ interactions. In addition to this, we add the fermionic matter content of

$$\mathcal{L}_f = \sum_{\alpha=1,2,3} \left(\sum_{\mathcal{F}=Q_\mathrm{L},L_\mathrm{L}} \bar{\mathcal{F}}_\alpha i \not{D} \mathcal{F}_\alpha + \sum_{f=u_\mathrm{R},d_\mathrm{R},\ell_\mathrm{R}} \bar{f}_\alpha i \not{D} f_\alpha \right), \tag{1.3}$$

where the fermionic indices are implicit and α is used as a generation index. The $SU(2)_\mathrm{L}$ doublets $Q_\mathrm{L} = (u_\mathrm{L}, d_\mathrm{L})$ and $L_\mathrm{L} = (\ell_\mathrm{L}, \nu_\mathrm{L})$ are the left-chiral projections $\psi_\mathrm{L} = (1-\gamma_5)/2\psi$, while the right chiral fields $u_\mathrm{R}, d_\mathrm{R}, \ell_\mathrm{R}$ are singlets under this transformation. We highlight, the *absence of a right handed neutrino singlet* ν_R in this model. Further, we have used the covariant derivative

$$D_\mu = \partial_\mu + i g_s \frac{\lambda^i}{2} G^i_\mu + i g \frac{\sigma^j}{2} W^j_\mu + i g' q_\mathrm{Y} B_\mu, \tag{1.4}$$

with g' being the coupling constant associated with $U(1)_\mathrm{Y}$, q_Y being the hypercharge and λ^i (σ^i) the Gell-Mann (Pauli) matrices.

So far we have established a functioning massless gauge theory, describing matter content and interactions. In reality, however, particles are known to be massive. This is a crucial point in the formulation of the SM as the introduction of masses typically breaks gauge invariance. This problem is circumvented by the *Higgs mechanism* [11–13], which generates fermion and boson masses while preserving gauge invariance. Here, a complex scalar field H is introduced transforming as a $SU(2)_\mathrm{L}$ doublet (H^+, H^0), so that we add

$$\mathcal{L}_H = (D^\mu H)^\dagger D_\mu H - V(H) \tag{1.5}$$

to the SM Lagrangian, where $V(H) = \mu^2 H^\dagger H + \lambda (H^\dagger H)^2$ is a Higgs potential.[4] This

[4] Note that only for $\mu^2 < 0$ there will be spontaneous symmetry breaking, while $\lambda > 0$ is required by vacuum stability. We further note that this ad-hoc potential is often referred to as a tree level potential, and indeed higher order terms might be significant (e.g. [14, 15]). Further, the presence of heavy right-handed neutrinos can alter the shape of this potential in certain scenarios (see e.g. [16] for a review).

field couples to left-right fermion pairs (u, d, ℓ) through Yukawa couplings $F^f_{\alpha\beta}$

$$\mathcal{L}_{\text{Yuk}} = -\sum_{\alpha\beta}\left(F^u_{\alpha\beta}\left(Q^\dagger_{\text{L}\alpha}\tilde{H}\right)u^\dagger_{\text{R}\beta} + F^d_{\alpha\beta}\left(Q^\dagger_{\text{L}\alpha}H\right)d^\dagger_{\text{R}\beta} + F^\ell_{\alpha\beta}\left(L^\dagger_{\text{L}\alpha}H\right)\ell^\dagger_{\text{R}\beta}\right) + \text{h.c.} \quad (1.6)$$

where $\tilde{H} = \varepsilon H^*$ and again α, β are generation indices. We note that since there is no right chiral neutrino component in the SM, neutrinos cannot attain a Yukawa coupling. Combining all the above Lagrangians, we can write out the full *Standard Model Lagrangian*

$$\mathcal{L}_{\text{SM}} = \mathcal{L}_{\text{gauge}} + \mathcal{L}_f + \mathcal{L}_H + \mathcal{L}_{\text{Yuk}}. \quad (1.7)$$

Higgs Mechanism - Spontaneous Symmetry Breaking

As alluded to in the previous part, SM masses are generated by Spontaneous Symmetry Breaking of the electroweak sector (EWSB) — the Higgs Mechanism. In this process, the gauge invariance of $SU(2)_{\text{L}} \times U(1)_{\text{Y}}$ is broken spontaneously, where the Higgs doublet assumes its non-zero *vacuum expectation value* (VEV) $\langle H \rangle$. Formally, there exists more than one possible VEV, but as they can all be obtained from one another by a suitable gauge transformation, choosing a particular VEV corresponds to fixing a gauge. Most commonly, the chosen VEV corresponds to the unitary gauge, where

$$H = \frac{1}{\sqrt{2}}\begin{pmatrix} 0 \\ v + h \end{pmatrix}. \quad (1.8)$$

Here, $v = \sqrt{-\mu^2\lambda^{-1}}$ and h being a hermitian field — the physical Higgs scalar as we see it in detectors.

Under the above symmetry breaking we find

$$\mathcal{L}_H \to m_W^2 W^{+\mu} W^-_\mu + \tfrac{1}{2} m_z^2 Z^\mu Z_\mu + h\text{-terms}. \quad (1.9)$$

Thus, EWSB successfully generates the massive gauge bosons W and Z with

$$m_W = \tfrac{1}{2} g_W v, \text{ and} \qquad m_z = \frac{m_W}{\cos\theta_W}, \quad (1.10)$$

where θ_W is the Weinberg angle $\tan^{-1}(g'/g_W)$. Meanwhile, a third gauge field A remains massless, describing the interactions of quantum electrodynamics. Furthermore, we have

$$\mathcal{L}_{\text{Yuk}} \to -\sum_{\alpha,\beta}\sum_{f=u,d,\ell} m^f_{\alpha\beta}\bar{f}_{\text{L}\alpha}f_{\text{R}\beta} + h\text{-terms} \quad (1.11)$$

with — potentially non-diagonal — Dirac masses $m^f_{\alpha\beta} = \frac{v}{2}\left(F^f_{\alpha\beta}\right)^*$.[5] In this way, EWSB also generates the masses of the SM fermionic matter content.

1.1.2 Neutrinos

First proposed in Wolfgang Pauli's famous 1930 letter to the "radioactive ladies and gentlemen" [19], and later named and described more thoroughly by Enrico Fermi in 1933 [20], it took until 1956 until the neutrino's eventual discovery by Reines and Cowan jr. [21].[6] Shortly after Wu [22] experimentally showed parity violation in the β-decay of ^{60}CO. This, in combination with the consequent neutrino helicity measurements by Goldhaber [23], led people to believe that neutrinos are massless and left-helical.

It is for this reason that in the formulation of the SM neutrinos decidedly seem to be the "odd-one-out", lacking a right chiral component. As we saw in Section 1.1.1, this means that in the Standard Model, neutrinos cannot attain mass through the Higgs mechanism. Indeed, precision experiments on β-decays [24] and cosmological bounds (see [25] and references therein) indicate that neutrino masses are smaller than $\mathcal{O}$(eV). However, there is reason to believe that they cannot be exactly 0, a phenomenon known as *neutrino oscillations*.

Neutrino Oscillations

When the flux of solar electron neutrinos was first observed in 1968 by the Homestake experiment [26], it was found that significantly fewer of them reached the earth from the sun than predicted by the standard solar model at the time [27]. More than 30 years later, the SNO experiment [28] definitively showed that the missing

[5] The fact that mass and flavour basis do not necessarily align is well-established for quarks where the rotation between the bases is described by the Cabibbo-Kobayashi-Maskawa (CKM) matrix [17, 18]. In weak interactions this leads to a possible conversion of quark flavour. As we will see in Section 1.1.2, this fact also plays an important role in our understanding of massive neutrinos.

[6] Given that Pauli was concerned that he had "postulated a particle that could not be detected", 20 years does not seem like an excessively long time. It should, however, give some perspective on what time scales to expect before we discover the even more elusive heavy neutral leptons experimentally.

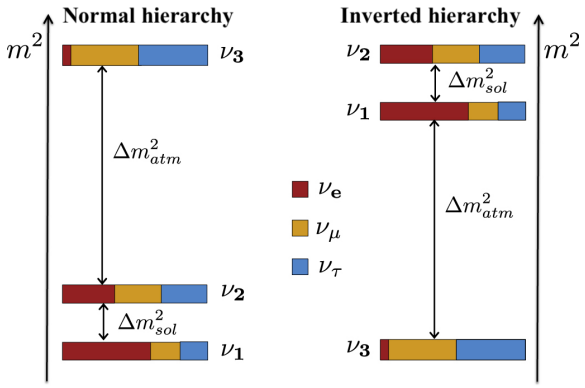

Figure 1.1: Schematic representation of neutrino mass splitting for normal (left) and inverted (right) hierarchy taken from [36].

electron neutrinos had been transformed into muon and tau neutrinos.[7] This, along with measurements on atmospheric neutrinos by the Superkamiokande in 1998 [31], provided experimental evidence for the phenomenon of neutrino oscillations, first proposed by Pontecorvo [32, 33]. Since then, many more experiments have observed neutrino flavour changes (see [16] for an overview), the common explanation for which is the *standard-3-scenario* (S3S, see [34] for a review).

In the S3S, one assumes 3 massive neutrinos. Just like in the case of quarks, the neutrino mass term is not diagonal in the basis of weak interactions that the Standard Model neutrinos can undergo. Thus, these flavour eigenstates $\nu_{L\ell}$ (again with $\ell = e, \mu, \tau$) are superpositions of the mass eigenstates ν_i with masses $m_{\nu i}$. The rotation between the two bases is described by the Pontecorvo-Maki-Nakagawa-Sakata (PMNS) matrix U_{PMNS} [33, 35]. If such a neutrino flavour package propagates with a given momentum, each non-degenerate mass eigenstate of its decomposition will have different energy, causing the individual wave function to oscillate with different frequencies. This causes a change in superposition of the mass eigenstates in time and, thus, along the neutrino packages trajectory.

To account for the oscillations measured, one needs two mass splittings in the neutrino mass basis. However (so far) experiments can only resolve the absolute value of these mass differences giving rise to two possible hierarchies of neutrino masses [36]. The mass splittings measured from atmospheric (Δm^2_{atm}) and solar (Δm^2_{sol}) neutrinos is shown schematically in Fig. 1.1 for normal and inverted hierarchy. Importantly,

[7] It should be noted that oscillation of freely propagating neutrinos does not account for this deficit, but works hand in hand with the Mikheyev Smirnov Wolfenstein effect [29, 30] describing resonant flavour transitions inside the sun — also requiring small neutrino masses.

this also does not include information about the absolute mass scale of neutrinos.

Hence, it is imperative that neutrinos have mass to explain neutrino oscillations, but as we saw in Section 1.1.1, this is not possible in the Standard Model. Hence, in order to explain neutrino oscillations, the Standard Model has to be extended.[8] One natural way to this is by including a Right chiral counterpart to the Standard Model neutrino, giving rise to the theory of *heavy neutral leptons*.

1.2 Heavy Neutral Leptons

In the previous section we saw the necessity of extending the Standard Model to accommodate light neutrino masses with a non-zero mass splitting. The arguably simplest extension to the SM to allow for light neutrino masses is the introduction of right handed singlet states — the heavy neutral leptons (HNLs). In this section, we will discuss the mechanism responsible for light neutrino masses in such models — the *type-I seesaw mechansim* — introduce certain theoretical considerations and present some common models of the extended neutrino sector.[9] Again, this introduction will be inspired by previous works on the subject [34, 40–42], while keeping a consistent naming convention throughout the thesis.

1.2.1 Type-I Seesaw Mechanism

We recall that the leptonic sector of the Standard Model contains three generations of left chiral $SU(2)_\mathrm{L}$ doublets $L_{\mathrm{L}\alpha}$ and right chiral $SU(2)_\mathrm{L}$ singlets $\ell_{\mathrm{R}\alpha}$. In the type-I seesaw [43–46] this is extended by a set of $\mathcal{N}$ right handed singlets $\nu_{\mathrm{R}I}$. For these uncharged singlet states it is admissible to add *Majorana mass terms* M_I [47], where the mass scale is not fixed and can range from $\sim$ eV to 10^{15} GeV.[10] The

[8] If light neutrinos are Majorana neutrinos one can also introduce them in an effective field theory approach through a Weinberg operator [37] without introducing new degrees of freedom to the Standard Model [34]. However, this does not yield a UV complete theory.

[9] Given the name, it is obvious that this is not the only mechanism of its kind to explain neutrino masses. The type-II seesaw mechanism (c.f. [38]) considers the introduction of new scalars, while the type-III seesaw (c.f. [39]) extends the SM by $SU(2)_\mathrm{L}$ triplets.

[10] This term is not profoundly motivated other than — as a dimension 3 — being a relevant term, and all other terms of this category being included in the Standard Model. It is arguably following the logic of "what is not forbidden must occur".

Lagrangian before electroweak symmetry breaking reads

$$\mathcal{L}_{\text{seesaw}} = \mathcal{L}_{\text{SM}} + \frac{i}{2}\nu_{\text{R}I}^{\dagger}\bar{\sigma}^{\mu}\partial_{\mu}\nu_{\text{R}I} - (F_{\alpha I})^{*}\left(L_{\alpha}\cdot\tilde{H}\right)^{\dagger}\nu_{\text{R}I} - \frac{M_I}{2}\nu_{\text{R}I}^{T}\nu_{\text{R}I} + h.c. \tag{1.12}$$

Here, $I = 1,\ldots,\mathcal{N}$, $L_{\alpha} = \begin{pmatrix}\nu_{\alpha}\\ l_{\alpha}\end{pmatrix}\text{L}$, where $\alpha = e,\mu,\tau$ and $\tilde{H}_a = \varepsilon_{ab}H_b^{*}$, where H is the Higgs doublet. After EWSB, this can be written as $H = \frac{1}{\sqrt{2}}\begin{pmatrix}0\\ v\end{pmatrix}$, where v is the Higgs' vacuum expectation value. And so $\left(L_{\alpha}\cdot\tilde{H}\right) = \frac{v}{\sqrt{2}}\nu_{L\alpha}$ after EWSB. The terms

$$\mathcal{L}_D = -\left(F_{\alpha I}^{\nu}\right)^{*}\frac{v}{\sqrt{2}}\nu_{L\alpha}^{\dagger}\nu_{\text{R}I} + h.c. \tag{1.13}$$

are equivalent to Dirac mass terms with $(m_D)_{\alpha I} = \frac{v}{\sqrt{2}}\left(F_{\alpha I}\right)^{*}$, resulting in the non-diagonal, complex, symmetric Dirac-Majorana mass matrix

$$\mathcal{L}_{\text{DM}} = -\frac{1}{2}\begin{pmatrix}\bar{\nu_{\text{L}}} & \bar{\nu_{\text{R}}^{c}}\end{pmatrix}\begin{pmatrix}0 & m_D\\ m_D^{T} & M_M\end{pmatrix}\begin{pmatrix}\nu_{\text{L}}^{c} & \nu_{\text{R}}\end{pmatrix} + h.c.\,, \tag{1.14}$$

where $M_M = \text{diag}(M_1,\ldots,M_{\mathcal{N}})$. In the *seesaw limit* $m_D \ll M_M$ (in terms of their eigenvalues), the mass matrix in Eq. (1.14) can be brought into approximate block diagonal form with submatrices

$$\begin{aligned} m_{\alpha\beta} &= -\sum_{I}\frac{(m_D)_{\alpha I}\,(m_D)_{\beta I}}{M_I}, \text{ and}\\ m_{IJ} &= M_I\delta_{IJ}. \end{aligned} \tag{1.15}$$

Additionally diagonalising $m_{\alpha\beta}$ by unitary transformation and redefining fields, we can rewrite Eq. (1.14) as

$$\mathcal{L}_{\text{DM}} = -\frac{m_i}{2}\left(\text{n}_i\text{n}_i + \text{n}_i^{\dagger}\text{n}_i^{\dagger}\right), \tag{1.16}$$

with $i = 1,\ldots 3+\mathcal{N}$, showcasing the existence of $3+\mathcal{N}$ Majorana states in this model — three light neutrino mass states ν_i with masses $m_{\nu i}$ and $\mathcal{N}$ heavy mass states N_I with masses $m_{\text{N}I}$.[11] It is, furthermore, useful to define the mixing angle

$$V_{\alpha I} = F_{\alpha I}\frac{v}{M_I} = \frac{(m_D)_{\alpha I}}{m_{\text{N}I}} \tag{1.17}$$

[11] The relationship between $m_{\alpha\beta}$ and $diag(m_{\nu 1}, m_{\nu 2}, m_{\nu 3})$ is given exactly by the PMNS matrix, which we use in writing out Eq. (1.18).

as small parameter.[12] Combining the relations above we find the *seesaw formula*

$$\left(U^{\dagger}\mathrm{diag}(m_{\nu 1}, m_{\nu 2}, m_{\nu 3})U\right)_{\alpha\beta} = \sum_{I} V_{\alpha I} V_{\beta I} m_{\mathrm{N}I}, \tag{1.18}$$

with U being the PMNS matrix introduced in Section 1.1.2 and $\alpha = (e, \mu, \tau)$.

In this framework, the minimal number of HNLs required to generate the two separate neutrino mass states necessary for neutrino oscillations is two [48].

Remarks on Parameter Space Bounds

Even though the seesaw relation in Eq. (1.18) is derived under the assumption

$$\text{Type-I seesaw:} \quad |V_{\alpha I}| < 1, \tag{1.19}$$

for large HNL masses, $m_{\mathrm{N}_I} \gtrsim v$, the requirement of perturbativity of the model described by Eq. (1.12), $|F_{\alpha I}| < 1$ becomes more restrictive than Eq. (1.19). Indeed, owing to Eq. (1.17) we get:

$$\text{Perturbativity:} \quad |V_{\alpha I}| < \frac{v}{M_I}. \tag{1.20}$$

The conditions in Eqs. (1.19) and (1.20) were used in Chapter 3 when deriving the maximal number of events produced at colliders Fig. 3.6.[13]

It should also be noted that a type-I seesaw model produces light neutrino masses of the order $m \sim |V|^2 m_{\mathrm{N}_1}$. This defines a minimal mixing angle, admissible for an HNL generating neutrinos compatible with neutrino oscillation data, commonly referred to as the *seesaw line*

$$|V|^2_{\mathrm{seesaw}} = \frac{\sqrt{|\Delta m^2_{\mathrm{atm}}|}}{m_{\mathrm{N}}}. \tag{1.21}$$

1.2.2 Violation of Lepton Number

By introducing the Majorana mass term in Eq. (1.12), breaking the SM lepton number becomes possible. This is due to Majorana neutrinos (ν_{R}) being their own anti particle (ν^c_{R}), and this term connecting the two at Lagrangian level. However, if there

[12] To make the notation more readable, we will sometimes write $V_{\ell \mathrm{N}}$ instead of $V_{\alpha I}$.

[13] Notice that in a model as described in Section 2.2, this requirement will be imposed on the heavier of the two HNLs and entail a limit on $V_{\ell 1}$ through Eq. (1.23).

exists a correlation between the mixing of different N_I with active neutrinos in order to account for small neutrino masses, non-trivial cancellations may suppress lepton number violating (LNV) with respect to lepton number conserving (LNC) processes [49–51]. In such models with approximate HNL mass degeneracy, there exists an approximate $U(1)$ symmetry relating the individual mixings and naturally allowing for mixing angles above the seesaw line [52–57]. In case of an exact symmetry (exact mass degeneracy), lepton number is exactly conserved. However, accidental breaking of this symmetry (potentially responsible for small neutrino masses[14]) may lead to HNL oscillations, possibly implying significant fractions of LNV/LNC process rates (see e.g. [59–61]).

In a degenerate two HNL model, one may realise such a symmetry by imposing

$$V_{\alpha 1} = iV_{\alpha 2}. \tag{1.22}$$

In the limit of exact mass degeneracy (*Dirac limit*), the two HNLs will combine into a single Dirac particle and as described above, lepton number is exactly conserved. For a quasi-degenerate two HNL model ($m_{\mathrm{N}1} \simeq m_{\mathrm{N}2}$) the combination of two HNLs still behaves in many ways as a Dirac-particle and is hence known as a *quasi-Dirac* (or pseudo-Dirac) pair [51]. Manifestly, this scenario results in small neutrino masses (by virtue of the seesaw relation Eq. (1.18)). An exact cancellation can be parametrised by a mass ratio r_{N} with

$$m_{\mathrm{N}2} = r_{\mathrm{N}} m_{\mathrm{N}1} \quad \text{and} \quad V_{\alpha 1} = i r_{\mathrm{N}}^{-1/2} V_{\alpha 2}. \tag{1.23}$$

We will refer to the class of models obeying this relation as *quasi-Dirac-like* (qDl). We note that for large r_{N}, radiative corrections to neutrino masses can be sizeable [50, 62–64] and that such cancellations arguably involve a high degree of fine tuning [63], making such models theoretically less appealing.

1.2.3 Neutrino Sector Models

In this section we will briefly introduce neutrino sector models established to address the unexplained phenomena in the introduction of this chapter. As the seesaw formula Eq. (1.18) leaves a great many degrees of freedom to the sterile neutrino parameters, theories have been put forward to explain multiple of the Standard

[14] Other schemes include the classical low-scale seesaws (see Section 1.2.1) and neutrino masses generated as radiative corrections (see e.g. [58]).

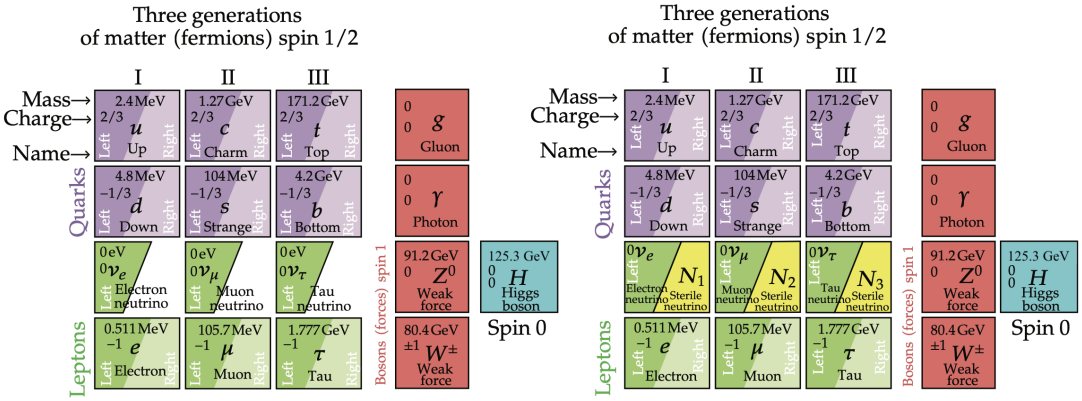

Figure 1.2: Particles of the Standard Model (left) and the νMSM (right). This graphic was taken from Gninenko et al.'s motivation paper for the SHiP experiment[67] and slightly altered to include the measured value of Higgs mass [68].

Models observational shortcomings at the same time.[15] One phenomenon many of these theories address is baryon asymmetry of the universe (BAU) — the fact that astronomical searches see more baryonic matter than antibaryonic matter in the observable universe.

Neutrino Minimal Standard Model

One such model of HNLs is the *neutrino minimal standard model* (νMSM [49, 65], see [66] for a review), which features $\mathcal{N} = 3$ sterile neutrinos. Arguably, introducing three right chiral neutrinos reestablishes symmetry between the quark and leptonic sector of the SM, which is shown in Fig. 1.2. As discussed above, three HNLs are capable of describing neutrino oscillations.

The lightest of the HNLs N_1 represents a dark matter candidate. The requirement here, is that it must not be too light (must be keV range or above), as dictated by the Tremaine-Gunn bound [69], and Pauli exclusion principle (applies to fermionic dark matter). Simultaneously, it must not be too heavy or strongly coupled, so that it can be stable — with respect to decays — on time scales comparable to the age of the universe. This greatly suppresses N_1s contribution in the seesaw of Eq. (1.18), effectively decoupling it from this mechanism. In spite of its ultra weak coupling, N_1

[15] In fact the number of free parameters in this theory are $7\mathcal{N} - 3$ (with $\mathcal{N}$ HNL generations), only $3 + 2n$ (with $2 \leq n \leq 3$ being the number of massive light neutrinos) are defined by the LHS. Further, only five of these (two mass splittings and three neutrino mixing angles) can be constrained with light neutrino oscillation data (see Fig. 1.1).

could have been generated resonantly [70] in sufficiently large quantities in the early universe.

The two heavier neutrinos N_2 and N_3 generate the lion's share of the light neutrino masses similarly to a qDL pair Eq. (1.23). Their mixing angles are sizeable, so that they decay quick enough not to undermine resonant dark matter production.[16] The masses $m_{N2,3}$ lie in a range of 1–100 GeV to allow BAU to originate at the right temperatures which allow it to survive — i.e. circumventing washout [72]. Furthermore, these masses need to be highly degenerate in order to cause significant enough CP-violation to explain BAU through leptogenesis.[17]

Akhmedov-Rubakov-Smirnov Models

If one drops the requirement of explaining dark matter through right handed neutrinos, the requirement on mass degeneracy of HNLs in order to explain BAU relaxes considerably. This class of models is commonly referred to as the Akhmedov-Rubakov-Smirnov (ARS) model [73–75]. Similarly to the νMSM, HNL mass degeneracy resonantly enhances leptogenesis in the ARS as well. However, due to this model being less restricted in terms of the exact sequence in which processes occur in the early universe, leptogenesis is also possible for non-degenerate HNLs [76]. Furthermore, such models can feature HNLs with masses up to 70 TeV [77].

1.3 Motivation for Same Sign Di-Lepton Searches

As discussed in Section 1.2.2, lepton number violation is possible if neutrinos (and/or HNLs) are of Majorana nature, making LNV signals the *smoking gun signature* of such models. Here, we will introduce one of the most extensively studied of such signatures, the neutrinoless double-β decay ($0\nu\beta\beta$).

1.3.1 Decay Measurements

In atoms, this LNV decay mode emits two leptons of the same charge, while simultaneously converting two neutrons into two protons (see Fig. 1.3). By studying the decay rate, one can draw conclusions on the Majorana particles, shown here with

[16] Indeed they can be seizable enough to be testable at LHC energies [71].
[17] In the language of Eq. (1.23) this corresponds to $rN - 1 < 10^{-4}$ for $m_{N2,3} = 100\,\text{GeV}$ [65].

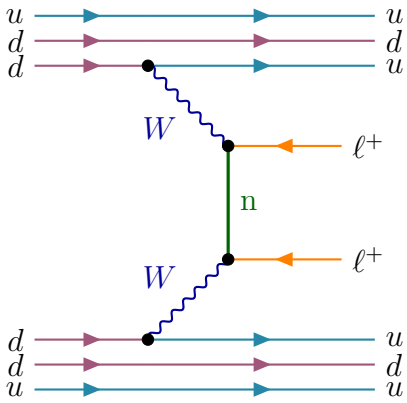

Figure 1.3: Feynman diagram of the neutrinoless double beta decay. This process is allowed exclusively by the Majorana fermion(s) n sitting at its heart.

n, enabling this process (see [78, 79] and [80, 81] for recent reviews). One of the main appeals of investigating $0\nu\beta\beta$ is that it is fully reconstructible. That is to say, there are no neutrinos in the final state, so that an event can be detected without further assumptions. Experiments have to reject background due to cosmic rays, environmental radioactivity and contamination of the potential $0\nu\beta\beta$ isotopes [82]. In principle, however, a single detection would manifest the Majorana nature of the neutrino. To the author's knowledge, as of publication of this thesis, no detection has been reported, with measured lower bounds on half lives as large as 10^{26} yr. This puts strong bounds on the HNL parameter spectrum [83–85].

1.3.2 At Hadron Colliders

At pp colliders, there exists a high energy equivalent to $0\nu\beta\beta$, namely $pp \to \ell^\pm\ell^\pm jj$ In this case the final QCD product is not stable and causes jet cascades in a detector. In the direct equivalent, the LNV is mediated by a Majorana particle in the t (and u) channel (shown in Fig. 1.4a) which we will refer to as W *boson fusion* (WBF). This process has enjoyed some theoretical attention in the past [97–101], while it was only recently investigated experimentally [86]. There also exists a (Drell-Yan) process sharing the same $pp \to \ell^\pm\ell^\pm jj$ signature (see Fig. 1.4b and [102, 103]), which has been studied quite thoroughly experimentally [87–96]. Despite their same collider signature, the two processes do not add coherently as the quark initial and final states are different.

Due to the higher energy at colliders, $pp \to \ell^\pm\ell^\pm jj$ would be able to resolve the

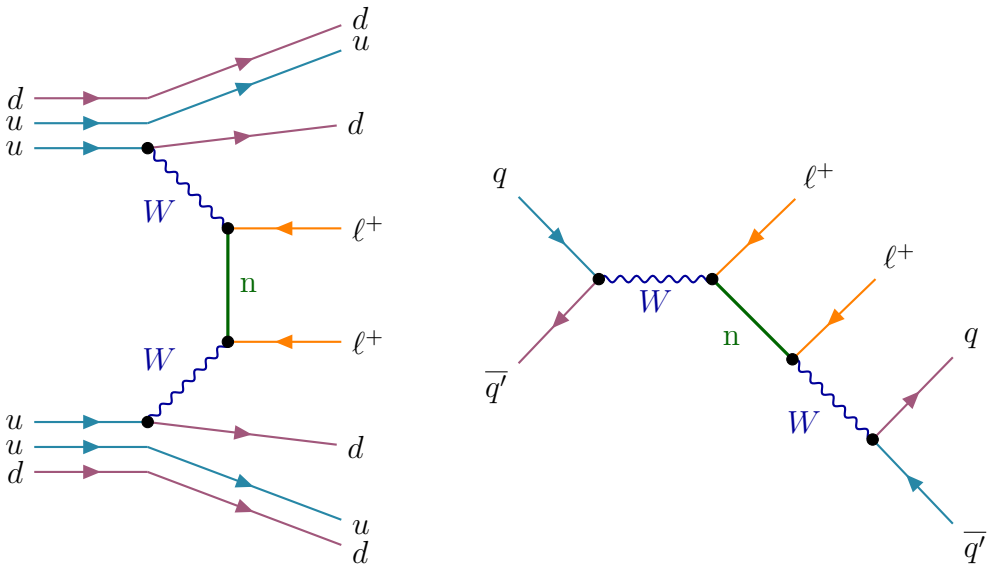

(a) WBF process, reminiscent of $0\nu\beta\beta$ decay, used to interpret same-sign lepton searches in [86].

(b) Drell-Yan process, used to interpret same-sign lepton searches in [87–96].

Figure 1.4: Two kinds of processes leading to same-sign leptons plus jets signatures in pp collisions, where n represents both light and heavy Majorana states. Vector boson fusion process with Majorana particles in t-channel is shown in panel (a). Drell-Yan process with Majorana particles in s-channel is shown in panel (b). The contribution from two processes add incoherently due to the antiquarks in the final state of process (b) compared to (a).

effects of more massive HNLs than $0\nu\beta\beta$-decay experiments. Furthermore, also these processes do not have any missing energy and, thus, portray valuable candidates for HNL collider searches — which manifests itself in a wealth of past works on this subject. As in the Drell-Yan (DY) process, the HNL can go on-shell in the narrow width approximation [104, 105] — hence, interference between Majorana states does not occur at amplitude level — the results of such studies can admissibly be performed in the phenomenological HNL model [40, 106] with free parameters of a single HNL generation. In case of the WBF process, the Majorana states are necessarily off-shell as they only exist in the t (u) channel of the process and thus, will interfere at amplitude level. Therefore, it is necessary to employ a neutrino sector model that is restricted by its predictions. In this study, we will be presenting results for models with one or two HNLs that result in small (tree level) neutrino masses. For one HNL, this corresponds to a mixing angle along the see-saw line and for an HNL pair we invoke a model with symmetry protected small neutrino masses.

As we will see, the latter can be well approximated by an HNL pair obeying the qDl conditions of Eq. (1.23).

1.4 Effective Vector Boson Approximation

In this thesis we will use the *effective vector boson approximation* (EVA) to generalise vector boson scattering cross sections to the case of hadron-hadron collisions at colliders. This is motivated by the fact that at interactions in the TeV range, the (polarised) gauge bosons of the Standard Model (see Section 1.1.1) can be viewed as part of a protons parton sea [107, 108]. In this way, the approximation is a generalisation of the well known parton distribution functions (PDFs) relying on the asymptotic freedom of QCD [109–111] (see e.g. [112] for a review) and equivalent to the better known effective photon (also known as Weizsäcker-Williams) approximation [113, 114]. We will give a brief sketch of the derivation and an overview here, taking inspiration from literature on the subject [108, 115–117].

1.4.1 Quark Level

In analogy to the Weizsäcker-Williams Approximation which derives the effective number of photons in an electron, we start by deriving the *effective number of polarised vector bosons* in a quark. To this effect, we consider the amplitude of a polarised massive vector boson (MVB, V) to scatter off a quark with energy E_q to form a final state X. For transversal polarisation, this is

$$\mathcal{A}_{\mathrm{T}}(V_{\mathrm{T}} + q \to X) = \varepsilon^i \cdot M\sqrt{E_q}\,, \text{ with } i = 1, 2\,, \tag{1.24}$$

the MVB polarisation vector ε^i_μ, M_μ describing the effective coupling of the $V-q-X$ vertex. In the lab frame of the quark, where k_{V0} is the MVB energy, this leads to the polarised differential cross section

$$\mathrm{d}\sigma_{\mathrm{T}}(V_{\mathrm{T}} + q \to X) = \frac{1}{16 k_{V0}\eta} \sum_{i=1}^{2} |\varepsilon^i \cdot M|^2 \mathrm{d}\Gamma, \tag{1.25}$$

where $\mathrm{d}\Gamma$ is the Lorentz-invariant phase space element, and $\eta = \sqrt{1 - m_V^2\, k_V^{-2}}$. Generalising this to the process

$$q_1 + q_2 \to V_\lambda \to q_1' + X \tag{1.26}$$

with polarisation λ and *neglecting the longitudinal* contributions to this process leads to

$$\begin{aligned} &iA_{\mathrm{T}}(\mathrm{q}_1 + \mathrm{q}_2 \to \mathrm{V}_\mathrm{t} \to \mathrm{q}_1' + \mathrm{X}) \\ &\qquad = \sum_{i=1}^{2} \bar{u}\left(p'\right)\left(C_\mathrm{V} + C_\mathrm{A}\gamma_5\right)\varepsilon_i u(p)\varepsilon_i \cdot M\sqrt{E_\mathrm{q}}\left(\frac{1}{\left(p-p'\right)^2 - m_V^2}\right), \end{aligned} \tag{1.27}$$

where the p is the incoming momentum of q_1 and p' the outgoing momentum of q'. For

$$\begin{aligned} \mathrm{V} = W \text{ we have} \quad & C_\mathrm{V} = -C_\mathrm{A} = g/2\sqrt{2}, \\ \text{and for } V = Z \quad & C_\mathrm{V} = \left(\mathrm{g}/\cos\theta_\mathrm{w}\right)\left(\frac{1}{2}T_{3L} - Q\sin^2\theta_\mathrm{w}\right), \\ & C_\mathrm{A} = -\left(\mathrm{g}/\cos\theta_\mathrm{w}\right)\left(\frac{1}{2}T_{3L}\right), \end{aligned} \tag{1.28}$$

where θ_w is the Weinberg angle, $g = \alpha/\sin\theta_w$, T_{3L} the third component of weak isospin of q_1, and α the electric charge.[18]

Averaging over spin and azimuthal angle, one can find the transversally polarised cross section

$$\begin{aligned} &\sigma_\mathrm{T}(q_1 + q_2 \to V_\mathrm{T} \to q' + X) \\ &\qquad = \int \frac{\mathrm{d}^3p'}{(2\pi)^3}\frac{C_V^2 + C_A^2}{8EE'}\frac{\mathrm{d}\Gamma}{(k_V^- M_V^2)^2}\left(\sin^2\theta'\frac{E_q^2 E'^2}{|\mathbf{k}|^2} - \frac{k^2}{2}\right)\sum_{i=1}^{2}|\varepsilon^i \cdot M|^2, \end{aligned} \tag{1.29}$$

where E (E') denotes the energy of q_1 (q'). The *main approximation* now consists in replacing the transverse current $|\varepsilon^i \cdot M|^2$ and the phase space element $\mathrm{d}\Gamma$ by their values at $k_V^2 \to m_V^2$ and $\theta' \to 0$. This makes the EVA a *small-angle approximation*. In this approximation we can rewrite Eq. (1.29) as

$$\begin{aligned} &\sigma_\mathrm{T}(q_1 + q_2 \to V_\mathrm{T} \to q' + X) = \\ &\qquad \frac{C_V^2 + C_A^2}{2\pi^2}\int \mathrm{d}k_{V0}\,\mathrm{d}\theta'\sin\theta'\frac{k_{V0}E'\eta}{E(k^2 - m_V^2)^2}\sigma_\mathrm{T}(V_\mathrm{T} + q_2 \to X), \end{aligned} \tag{1.30}$$

with $k^2 = 2EE'(\cos\theta' - 1)$, and $\sigma_\mathrm{T}(V_\mathrm{T} + q_2 \to X)$ from Eq. (1.25).

Now, Eq. (1.30) has the form of a parton folding function if we define the distribution function $f_{V/q}^{\mathrm{Trans.}}$ such that

$$\sigma_\mathrm{T}(q_1 + q_2 \to V_\mathrm{T} \to q' + X) = \int_{x_\mathrm{min}}^{1} \mathrm{d}x\, f_{V/q}^{\mathrm{Trans.}}(x)\sigma_\mathrm{T}(V_\mathrm{T} + q_2 \to X). \tag{1.31}$$

[18] For a detailed explanation of these couplings and their relationships see section 21.4 of [118].

Here, we have changed the integration variable to the Björken-x, which is the partonic momentum fraction $x = k_V/p_1$. This quark level transversal distribution function is written as

$$\begin{aligned} f_{V/q}^{\text{Trans.}}(x) =& \frac{C_{\text{V}}^2 + C_{\text{A}}^2}{8\pi^2 x}\left[\frac{-x^2}{1 + m_V^2/\left(4E_q^2(1-x)\right)} + \frac{2x^2(1-x)}{m_V^2/E_q^2 - x^2}\right. \\ &+ \left(x^2 + \frac{x^4(1-x)}{\left(m_V^2/E_q^2 - x^2\right)^2}\left(2 + \frac{m_V^2}{E_q^2(1-x)}\right) - \frac{x^2}{\left(m_V^2/E_q^2 - x^2\right)^2}\frac{m_V^4}{2E^4}\right) \\ &\left.\times \log\left(1 + \frac{4E_q^2(1-x)}{m_V^2}\right) + x^4\left(\frac{2-x}{m_V/E_q^2 - x^2}\right)^2 \log\frac{x}{2-x}\right]\eta, \\ \text{with } \eta =& \sqrt{1 - \frac{m_V^2}{x^2 E_q^2}}, \end{aligned} \tag{1.32}$$

quark sub-energy E_q, and coefficients $C_{\text{A}}, C_{\text{V}}$ as given in Eq. (1.28).

Under the same approximations, one can analogously derive a quark level distribution function for longitudinally polarised MVB

$$\begin{aligned} f_{V/q}^{\text{Long.}}(x) =& \frac{C_{\text{V}}^2 + C_{\text{A}}^2}{\pi^2}\frac{1-x}{x}\frac{\eta}{(1+\eta)^2} \\ &\times\left\{\frac{1 - x - m_V^2\left(8E_q^2\right)^{-1}}{1 - x + m_V^2/\left(4E_q^2\right)} - \frac{m_V^2}{4E_q^2}\frac{1 + 2(1-x)^2}{(1-x) + m_V^2\left(4E_q^2\right)^{-1}}\frac{1}{m_V^2/E_q^2 - x^2}\right. \\ &- \frac{m_V^2}{4E_q^2}\frac{x^2}{2(1-x)\left(x^2 - m_V^2/E_q^2\right)^2}\left[(2-x)^2\log\frac{x}{2-x}\right. \\ &\left.\left. - \left(\left(x - \frac{m_V^2}{E_q^2 x}\right)^2 - \left(2(1-x) + x^2\right)\right)\log\left(1 + \frac{4E_q^2(1-x)}{m_V^2}\right)\right] \right. \\ &- \frac{m_V^2}{8E_q^2}\frac{x}{\sqrt{x^2 - m_V^2/E_q^2}}\left(\frac{2}{x^2 - m_V^2/E_q^2} + \frac{1}{1-x}\right) \\ &\left.\times\left(\log\frac{2 - x - \sqrt{x^2 - m_V^2/E_q^2}}{2 - x + \sqrt{x^2 - m_V^2/E_q^2}} - \log\frac{x - \sqrt{x^2 - m_V^2/E_q^2}}{x + \sqrt{x^2 - m_V^2/E_q^2}}\right)\right\}, \end{aligned} \tag{1.33}$$

using the same notation as in Eq. (1.32).

1.4.2 Proton Level

Equipped with the polarised quark level distribution functions for the massive vector bosons (VDF) as given in Eqs. (1.32) and (1.33), we can now extend this to find the corresponding proton level parton distribution functions for MVB. To this end, we fold the quark level VDFs with the PDFs $f_{q/p}$ of the relevant quarks q_{rel} for the MVB's production, yielding

$$f^{\lambda}_{V/p}(x) = \sum_{q_{\text{rel}}} \int_{\xi_{\min}}^{1} \frac{\mathrm{d}\xi}{\xi} f_{q/p}(\xi) f^{\lambda}_{V/q}(x/\xi), \tag{1.34}$$

where $\lambda = \mathrm{L}, \mathrm{T}$ is the MVB polarisation.

Due to the approximations taken, the MVB in the EVAs are real particles. Thus, we find a first limit on ξ, namely $m_V E_q^{-1} < \xi$. As the MVB can, further, carry maximally the full momentum of its mother-quark, another lower limit is given by $x < \xi$. The maximum of these two limits determines $\xi_{\min}$ in Eq. (1.34).

Factorisation Theorem

Let us consider pp a scattering sub-process

$$a + b \to X \tag{1.35}$$

of two massive partons a, b with masses m_a, m_b. We will denote the centre of mass energy as $M^2_{ab} = (p_a + p_b)^2$ and the minimal invariant mass for X to occur as m^2_X. As a is a parton of p, Process (1.35) can be generalised to

$$a + p \to X + Y. \tag{1.36}$$

Given proton level PDFs $f_{a/p}$ we can write[19]

$$\sigma_{ap\to X+Y} = \int_{x_{\min}} \mathrm{d}x\, f_{a/p}(x) \sigma_{ab\to X}. \tag{1.37}$$

Since

$$M^2_{ab} = (p_a + p_b)^2 = m_a^2 + m_b^2 + x s_{ap}, \tag{1.38}$$

we find a minimum value

$$x^{\min} = \frac{M^2_{ab} - m_a^2 - m_b^2}{s_{ap}} \quad \text{and} \quad s^{\min}_{ap} = m^2_X + m^2_Y. \tag{1.39}$$

[19] Of course this is only valid in case $pb \to X + Y$ does not add coherently with other parton channels.

If the intermediate particles of the PDFs have to be allowed to go on shell we have $s_{ap}^{\min} = \max(m_X^2 + m_Y^2, 2m_b^2)$.

Extending this again to

$$pp \to X + Y + Z, \tag{1.40}$$

we find the lower bounds

$$\begin{aligned} x_1^{\min} &= \frac{s_{ap}^{\min}}{s_{pp}} = \frac{\max(m_X^2 + m_Y^2, 2m_b^2)}{s_{pp}} \\ x_2^{\min} &= \frac{\max(m_X^2, m_a^2)}{s_{bp}} = \frac{\max(m_X^2 + m_Z^2, 2m_a^2)}{x_1 s_{pp}}, \end{aligned} \tag{1.41}$$

assuming on-shell partons. As the assignment of the partons a, b to the individual protons is arbitrary, we find

$$\sigma_{pp\to X+Y+Z}(s) = \int_{x_1^{\min}}^1 \int_{x_2^{\min}}^1 \mathrm{d}x_1\, \mathrm{d}x_2\, f_{a/p}(x_1) f_{b/p}(x_2) \sigma_{ab\to X} + (a \leftrightarrow b) \tag{1.42}$$

which is known as the *factorisation theorem*.[20] This theorem establishes a simple way of calculating approximate pp-scattering cross sections from those of its partonic subprocesses.

Parton Distribution Functions of the Effective W Approximation

As they will be of importance to this work, we present the parton distribution functions for polarised W^+ bosons at the relevant centre of mass energies in Fig. 1.5. The underlying quark level WDFs are Eqs. (1.32) and (1.33). These are folded with the quarks' recommended PDFs for the LHC by Martin et al. [119] according to Eq. (1.34).

[20] Note that this is a slightly adjusted version of the theorem presented by Ruiz [117], to accommodate parton masses $m_{a,b}$.

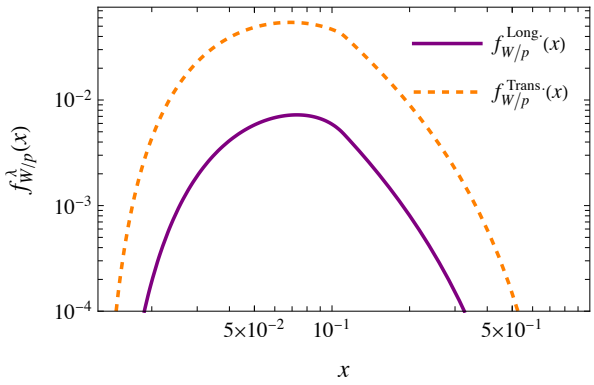

(a) $\sqrt{s_{\text{LHC}}} = 13\,\text{TeV}$

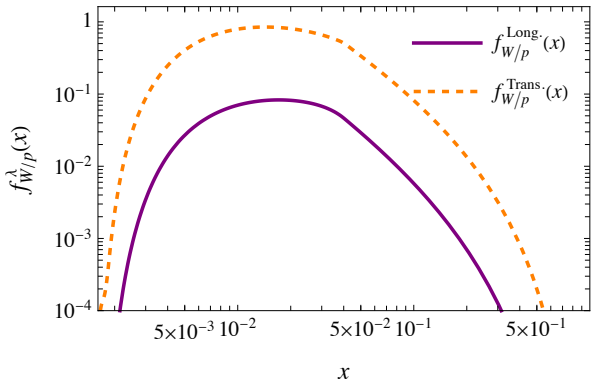

(b) $\sqrt{s_{\text{FCC}}} = 100\,\text{TeV}$

Figure 1.5: Parton distribution functions for polarised W^+ in the effective W approximation as prescribed by Dawson [108] at LHC (a) and expected FCC centre of mass energy (b). The underlying quark parton distribution functions used were taken from Martin et al. [119].

Same Sign WW Scattering

2

In order to study more complicated processes like W boson fusion in $pp \to \ell^\pm\ell^\pm jj$ scattering, it is imperative to first understand the lepton number violating process at its heart, $W^\pm W^\pm \to \ell^\pm\ell^\pm$ scattering. In the following we will study the interplay of light and heavy contributions in this process for the case of one (Section 2.1) and two (Section 2.3) heavy neutral leptons. We will also discuss the process in the quasi-Dirac-like approximation of the two HNL case (Section 2.2), which we will rely on for further analysis.

As a standard value for the centre of mass energy for this chapter, we will choose the expectation value of the invariant mass of the WW system in WBF at LHC energy $\sqrt{s_{\text{LHC}}} = 13\,\text{TeV}$. Using the parton distribution functions of the effective W approximation (see Fig. 1.5). We find for the longitudinal case

$$\begin{aligned} E[M_{\text{WW}}^2] &= \frac{s_{\text{LHC}} \int_0^1 \int_0^1 \mathrm{d}x_1\, \mathrm{d}x_2\, (x_1+x_2)^2 f_{p/W}^{\text{long.}}(x_1) f_{p/W}^{\text{long.}}(x_2)}{4 \int_0^1 \int_0^1 \mathrm{d}x_1\, \mathrm{d}x_2\, f_{p/W}^{\text{long.}}(x_1) f_{p/W}^{\text{long.}}(x_2)} \\ &= 490^2\,\text{GeV}^2, \end{aligned} \tag{2.1}$$

which is well in agreement with typical values for M_{WW} in the Montecarlo simulation of WBF by Fuks et al. [101]. At this energy, the results are applicable to all $\ell = e, \mu, \tau$, since for all generations the lepton masses m_ℓ will always be small compared to the typical energies off the process ($m_\ell^2 \ll |t|_{\text{min}}, M_{\text{WW}}^2$). The lepton mass can thus safely be set to 0 for the following discussion.

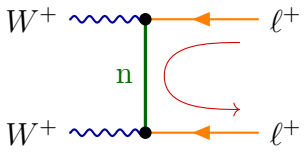

Figure 2.1: Feynman Diagram of the two same sign W-bosons to two same sign leptons in the mass basis. Here n represents both heavy (N) and light (ν) mass eigenstates.

2.1 Single Heavy Neutral Lepton Model

A common model employed in phenomenological searches for HNLs is the phenomenological type-I seesaw [106, 40]. This model features a single isolated HNL, where mixing angle and HNL mass are treated as free parameters. In the following, we will investigate what the single HNL case looks like in a model, where this HNL is the generation mechanism of the light neutrino masses. This will occur inevitably by the seesaw relation Eq. (1.18). To this end we will employ a toy model, where we will approximate the light mass states as a single light mass state with PMNS-like mixing of 1.[1] As a requirement we set that the light neutrino mass be 1 eV, which is roughly compatible with recent upper limits on neutrino masses from measurements on β decays [24]. To this end, we set the mixing angle

$$\left|V_{\ell \mathrm{N}}^2\right| = \left|\frac{m_\nu}{m_\mathrm{N}}\right| = \frac{1\,\mathrm{eV}}{m_\mathrm{N}} \tag{2.2}$$

guaranteeing the above requirement through Eq. (1.18).

2.1.1 Amplitude Level

The Feynman diagram of the process $W^+W^+ \to \ell^+\ell^+$ is given by Fig. 2.1. The Feynman rules for lepton number violating processes involving Majorana fermions are well documented [120–122]. According to the algorithmic process established by Denner et al. [121], the partial amplitude associated with the Feynman diagram shown in Fig. 2.1 is given by

$$i\mathcal{A}_{\mathrm{n},p^2} = -\frac{i}{2}g^2\mathcal{U}_{\ell\mathrm{n}}^2\left(\overline{u}_{\mathrm{f}2}\gamma^\alpha P_R\frac{\not{p}+m_\mathrm{n}}{p^2-m_\mathrm{n}^2}\gamma^\beta P_L v_{\mathrm{f}1}\right)\varepsilon_{\mathrm{i}1,\alpha}\varepsilon_{\mathrm{i}2,\beta}, \tag{2.3}$$

[1] In the single HNL case all generated light neutrino masses will be the same, so that we can choose to use a PMNS-like mixing of 1 with a single light mass state without loss of generality.

where p is the momentum associated with the Majorana propagator and $\frac{i}{\sqrt{2}} g \mathcal{U}_{\ell \mathrm{n}} P_L$ is the $W\ell\mathrm{n}$ vertex value. It is useful to define

$$\begin{aligned} J^{\alpha\beta}\left(p^2, m\right) &= \gamma^\alpha P_R \frac{\not{p} + m}{p^2 - m^2} \gamma^\beta P_L \\ &= \gamma^\alpha \frac{m}{p^2 - m^2} \gamma^\beta P_L, \end{aligned} \tag{2.4}$$

where in the last step we used the configuration of chiral projectors cancelling $\not{p}$ in the numerator. At tree level, this structure is universal to all lepton number violating processes facilitated by a Majorana fermion and we will thus refer to it from now on as the LNV current.

The full amplitude of the scattering process then is given by

$$\begin{aligned} i\mathcal{A} = \quad & -\frac{i}{2} g^2 \varepsilon_{\mathrm{i}1,\alpha} \varepsilon_{\mathrm{i}2,\beta} \overline{u}_{\mathrm{f}2} \left(V_{\ell\mathrm{N}}^2 J^{\alpha\beta}(t, m_\mathrm{N}) + J^{\alpha\beta}(t, m_\nu) \right) v_{\mathrm{f}1} \\ & + (t \leftrightarrow u,\, \mathrm{f}1 \leftrightarrow \mathrm{f}2) \\ = \quad & -\frac{i}{2} g^2 \varepsilon_{\mathrm{i}1,\alpha} \varepsilon_{\mathrm{i}2,\beta} \overline{u}_{\mathrm{f}2} \left(V_{\ell\mathrm{N}}^2 J^{\alpha\beta}(t, m_\mathrm{N}) + J^{\alpha\beta}(t, -V_{\ell\mathrm{N}}^2 m_\mathrm{N}) \right) v_{\mathrm{f}1} \\ & + (t \leftrightarrow u,\, \mathrm{f}1 \leftrightarrow \mathrm{f}2)\,. \end{aligned} \tag{2.5}$$

In case $V_{\ell\mathrm{N}}^4 m_\mathrm{N}^2 \ll |p^2|$, we see that

$$\begin{aligned} & V_{\ell\mathrm{N}}^2 J^{\alpha\beta}(p^2, m_\mathrm{N}) + J^{\alpha\beta}(p^2, -V_{\ell\mathrm{N}}^2 m_\mathrm{N}) \\ & \qquad = -V_{\ell\mathrm{N}}^2 \frac{m_\mathrm{N}^2}{p^2} \left(J^{\alpha\beta}(p^2, m_\mathrm{N}) - \frac{\gamma^\alpha \gamma^\beta P_L}{m_\mathrm{N}} \sum_{n=1}^{\infty} \left(-\frac{V_{\ell\mathrm{N}}^4 m_\mathrm{N}^2}{p^2} \right)^n \right) \\ & \qquad = -V_{\ell\mathrm{N}}^2 \frac{m_\mathrm{N}^2}{p^2} J^{\alpha\beta}(p^2, m_\mathrm{N}) + \mathcal{O}\left(\left(\frac{V_{\ell\mathrm{N}}^2 m_\mathrm{N}^2}{p^2} \right)^2 \right). \end{aligned} \tag{2.6}$$

This approximation corresponds to the first order expansion in $V_{\ell\mathrm{N}}$ in the flavour basis (see Fig. E.2).

As it is explicitly proportional to the light neutrino mass according to the seesaw relation Eq. (1.18), the amplitude disappears for vanishing light neutrino masses as described by Kersten-Smirnov [50]. However, we see that there exists a regime ($V_{\ell\mathrm{N}}^4 m_\mathrm{N}^2 \ll |p^2| \ll m_\mathrm{N}^2$), where the light neutrino contribution to the amplitude dominates that of the HNL.

For $m_{\mathrm{N}}^2 \ll |p^2|$ we find

$$\begin{aligned} V_{\ell\mathrm{N}}^2 J^{\alpha\beta}(p^2, m_{\mathrm{N}}) + J^{\alpha\beta}(p^2, -V_{\ell\mathrm{N}}^2 m_{\mathrm{N}}) \\ &= -V_{\ell\mathrm{N}}^2 \frac{m_{\mathrm{N}}}{p^2} \gamma^\alpha \gamma^\beta P_L \sum_{n=1}^{\infty} (1 + \left(-V_{\ell\mathrm{N}}^4\right)^n) \left(\frac{m_{\mathrm{N}}^2}{p^2}\right)^n \\ &= -\frac{V_{\ell\mathrm{N}}^2 m_{\mathrm{N}}}{m_{\mathrm{N}}^2} \left(\frac{m_{\mathrm{N}}^2}{p^2}\right)^2 \gamma^\alpha \gamma^\beta P_L + \mathcal{O}\left(\left(\frac{m_{\mathrm{N}}^2}{p^2}\right)^3, V_{\ell\mathrm{N}}^6\right), \end{aligned} \tag{2.7}$$

which vanishes significantly faster for large p^2 than the isolated HNL

$$V_{\ell\mathrm{N}}^2 J^{\alpha\beta}(p^2, m_{\mathrm{N}}) = \frac{V_{\ell\mathrm{N}}^2 m_{\mathrm{N}}}{m_{\mathrm{N}}^2} \frac{m_{\mathrm{N}}^2}{p^2} \gamma^\alpha \gamma^\beta P_L + \mathcal{O}\left(\left(\frac{m_{\mathrm{N}}^2}{p^2}\right)^2\right). \tag{2.8}$$

This means that at large p^2 the LNV current $J^{\alpha\beta}$ is suppressed by the cancellation of light and heavy mass states.[2] As shown in Appendix C this inherent cancellation does not occur for lepton flavour violating processes.

2.1.2 Observables

To better understand what this means in practice, let us now look at the physical observables of this process. To avoid ambiguity, we will limit ourselves to the case of $W^+W^+ \to e^+e^+$ scattering. However, the results should be applicable to all combinations of $\ell^+\ell'^+$ final states given that the relevant parameters (m_ℓ, m_{ν_ℓ}) are negligible when compared to the other parameters of the process (m_{N}, M_{WW}, t).

It should be noted here that we will be using the first flavour basis expansion (see Eq. (2.7)) to calculate the observables of the full theory. This is motivated by the fact that the assumed light neutrino mass will fulfil the requirement of $m_\nu^2 \ll |p^2|$ in all cases, since

$$\begin{aligned} 1\,\mathrm{eV}^2 \gtrsim m_\nu^2 \ll |t|_{\min} &= \frac{m_W^4}{M_{\mathrm{WW}}^2} + \mathcal{O}\left(\left(\frac{m_W^2}{M_{\mathrm{WW}}^2}\right)^2\right) \\ &= 13^2\,\mathrm{GeV}^2 \quad \text{for } \sqrt{M_{\mathrm{WW}}^2} = 490\,\mathrm{GeV}. \end{aligned} \tag{2.9}$$

We stress that this approximation needs to be handled with care, as it produces unphysical results when the expansion in Eq. (2.6) does not hold.

[2] This seems to suggest that it is impossible to observe LNV processes in the s-channel at high energies. However as mentioned in Section 1.2.2, HNL oscillations of a quasi-Dirac HNL pair potentially allow for sizeable lepton number violation.

Differential Cross Section

Figure 2.2 shows the differential cross section of $W^\pm W^\pm \to \ell^\pm \ell^\pm$ scattering as a function of the Mandelstam variable $-t$ for $m_\mathrm{N} = 150\,\mathrm{GeV}$ (for other HNL masses find Fig. E.3). In the logarithmic representation it is not easy to see, but all differential cross section contributions are symmetric under $t \mapsto t_\mathrm{max} - t$, as this corresponds to an exchange from t- to u-channel.

In this simple model, for any m_N the light mass state contribution (green dash-dotted) is larger than that of the heavy mass state (orange dashed).[3] This is because in this simple model the amplitudes of light and heavy neutrino are identical safe for an extra suppression of $t/(|t| + m_\mathrm{N}^2)$ for the latter. The blue solid line shows the full differential cross section in the approximation of Eq. (2.7). As can be seen, the combined differential cross section follows the light neutrino divergence towards small values of t (u). Toward the centre of the t-range, the cancellation between the two contributions is the strongest, as here $t \simeq u$, so that simultaneously both the t and u channel propagator denominators are dominated by t or u respectively. From a phenomenological point of view it is interesting to note that unlike the more evenly distributed differential cross section of the single heavy mass state, the combined differential cross section in this model shows a clear tendency toward back-to-back scattering. On this note it should be mentioned that for $m_\mathrm{N}^2 < \frac{1}{4}(1+\sqrt{5})m_W^2$ the gradient of the HNL contribution itself flips sign and we get a convex shaped differential cross section approaching that of the light neutrino for decreasing m_N (see for example Figs. E.3b and E.3c).

With increasing m_N, the heavy state contribution is suppressed by m_N^2 in the LNV current denominator (see Fig. E.3d). This means that the differential cross section of the isolated heavy mass state vanishes and the combined differential cross section converges toward that of the isolated light mass state. With decreasing m_N the HNL propagator becomes divergent in the limit of $(-t)_\mathrm{min}$ (u_min), cancelling that of the light neutrino, so that the divergence in the combined cross section becomes less prominent.

Cross Section

Integrating the differential cross section with respect to t we find the total cross section. This is shown as a function of the HNL mass m_N at a center of mass energy

[3] Strictly speaking this is only true for $m_\nu < m_\mathrm{N}$, but in this limit the seesaw expansion is already invalid.

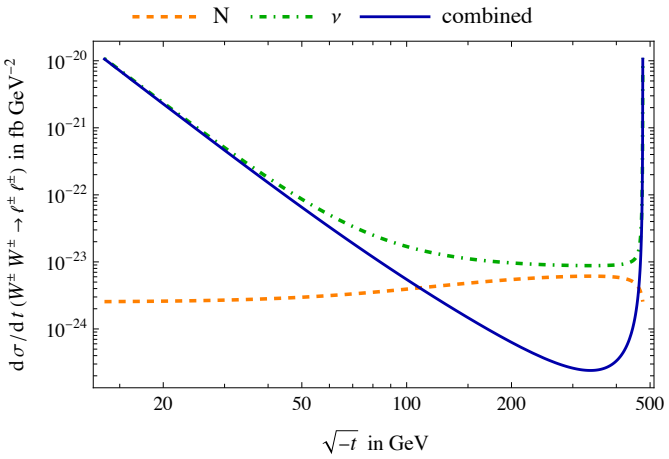

Figure 2.2: Differential cross section of $W^\pm W^\pm \to \ell^\pm \ell^\pm$ scattering in the case of a single HNL as a function the Mandelstam variable $\sqrt{-t}$ at a centre of mass energy of $\sqrt{M^2_{\mathrm{WW}}} = 490\,\mathrm{GeV}$ and for HNL mass $m_{\mathrm{N}} = 100\,\mathrm{GeV}$. The mixing angle here is a function of the HNL mass as well, such that $|V^2_{\ell\mathrm{N}} m_{\mathrm{N}}| = 1\,\mathrm{eV} \gtrsim m_{\nu_e}$. The orange dashed (green dash-dotted) line represents the differential cross section if only the heavy (light) mass states contributed to the process. The blue solid line shows the full differential cross section in the approximation of Eq. (2.7).

$\sqrt{M^2_{WW}} = 490\,\mathrm{GeV}$. The mixing angle $V_{\ell\mathrm{N}}$ in this plot is a function of m_{N} to keep the generated light mass state (shown in dash-dotted green) constant.

We see that the cross section of the isolated heavy mass state (shown in dashed orange) for $m_{\mathrm{N}} \sim$ few GeV is indistinguishable from that of the light mass state on the scales of the plot. As can also be seen in Fig. E.3, the differential cross section only starts to differ from that of the light mass state, when m_{N} becomes comparable to $\sqrt{(-t)_{\mathrm{min}}} \simeq 13\,\mathrm{GeV}$ at $M_{\mathrm{WW}} = 490\,\mathrm{GeV}$. For $\sqrt{(-t)_{\mathrm{min}}} < m_{\mathrm{N}} < \sqrt{\frac{1}{2} M^2_{\mathrm{WW}}}$ we see that the cross section of the isolated heavy mass state drops as m_{N}^{-2}. This is because for increasingly large parts of the phase space the LNV current denominator is dominated by m^2_{N}, so that the cross section scales to leading order as $|V_{\ell\mathrm{N}}|^4 m^0_{\mathrm{N}}$. Under the condition of Eq. (2.2) this yields a dependence of m_{N}^{-2} as observed. For $M^2_{\mathrm{WW}} \ll m^2_{\mathrm{N}}$ the LNV current denominator is dominated by m^2_{N} for the entirety of the available phase space. Following a similar reasoning as above, we observe a dependence of the isolated heavy state cross section as m_{N}^{-6}.

The full cross section (shown in blue) is described by the destructive interference between heavy and light mass state. Thus, we see a nearly mirrored dependence on the HNL mass m_{N} when compared to the isolated heavy mass state, where the cross

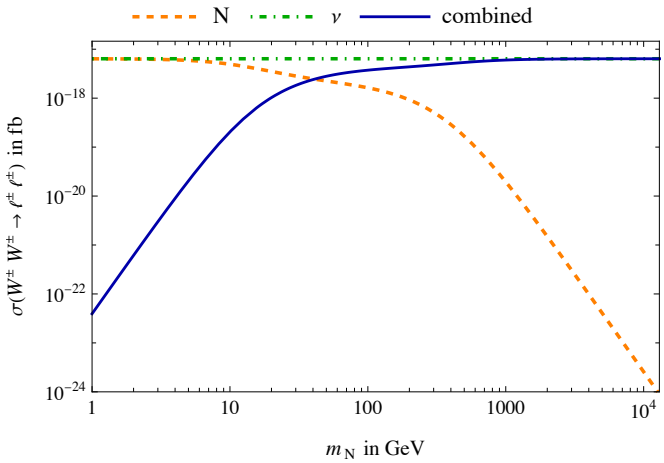

Figure 2.3: Cross section of $W^\pm W^\pm \to \ell^\pm \ell^\pm$ scattering in the case of a single HNL as a function of the HNL mass at a centre of mass energy of 490 GeV. The mixing angle here is a function of the HNL mass as well, such that $|V_{\ell N}^2 m_N| = 1\,\text{eV} \gtrsim m_{\nu_e}$. The orange dashed (green dash-dotted) line represents the cross section if only the heavy (light) mass states contributed to the process. The blue solid line shows the full cross section in the approximation of Eq. (2.7).

section vanishes for $m_N \to 0$ and asymptotically approaches the numerical value of the isolated light state for $M_{WW} \ll m_N^2$.

We note that $m_\nu = 1\,\text{eV}$ is only an upper bound, while realistic mixing angles could be as low as the seesaw line (see Section 1.2.1). As the scale of the observables shown is determined by m_ν, they could be even smaller than shown here.

2.2 Quasi-Dirac-Like Heavy Neutral Lepton Pair

In a model with at least two HNLs it is possible to arrange the mixing angles in such a way that the individual contributions to the light neutrino masses cancel

$$0 \stackrel{!}{=} m_{\ell\ell'} = \sum_{I=1}^{\mathcal{N}} V_{\ell I} V_{\ell' I} m_{NI}. \tag{2.10}$$

In the context of two HNLs this can be achieved under the prescription of Eq. (1.23) with a real $V_{\ell 1}$, without loss of generality.[4] If we require our two HNLs to fulfil Eq. (1.23), we can allow ourselves to be agnostic about the origin of light neutrino masses. If on top of that we require the light neutrinos to be Dirac particles, we can attribute the observation of Majorana effects solely to the HNLs.

In the following we will discuss, what effects the condition Eq. (1.23) has on $W^\pm W^\pm \to \ell^\pm \ell^\pm$ and LNV processes in general.

2.2.1 Amplitude Level

In the above described scenario, using the LNV current $J^{\alpha\beta}(p^2, m)$ as defined in Eq. (2.4), we can write the amplitude of $W^\pm W^\pm \to \ell^\pm \ell^\pm$ in the mass basis (see Fig. 2.1) as

$$\begin{aligned} i\mathcal{A} = &-\frac{i}{2} g^2 \varepsilon_{\mathrm{i1},\alpha} \varepsilon_{\mathrm{i2},\beta} \overline{u}_{\mathrm{f2}} \left(V_{\ell 1}^2 J^{\alpha\beta}(t, m_{\mathrm{N1}}) + V_{\ell 2}^2 J^{\alpha\beta}(t, m_{\mathrm{N2}}) \right) v_{\mathrm{f1}} \\ &+ (t \leftrightarrow u,\ \mathrm{f1} \leftrightarrow \mathrm{f2})\,. \end{aligned} \tag{2.11}$$

We notice that under Eq. (1.23)

$$V_{\ell 1}^2 J^{\alpha\beta}(t, m_{\mathrm{N1}}) + V_{\ell 2}^2 J^{\alpha\beta}(t, m_{\mathrm{N2}}) = V_{\ell 1}^2 J^{\alpha\beta}(t, m_{\mathrm{N1}}) \left(1 - \frac{t - m_{\mathrm{N1}}^2}{t - r_{\mathrm{N}}^2 m_{\mathrm{N1}}^2} \right), \tag{2.12}$$

where $r_{\mathrm{N}} = \frac{m_{\mathrm{N2}}}{m_{\mathrm{N1}}}$ is the mass ratio. From now on we will drop the index on N_I, where N is implicitly the lighter mass state N_1 unless stated explicitly.
As mentioned in Section 1.2.2, in case of $r_{\mathrm{N}} \simeq 1$ the two Majorana HNLs combine to form a quasi Dirac pair. We see that in the exact limit, the LNV current and thus all off-shell LNV processes, vanish.

In case of large r_{N} so that $|t|_{\max} \ll r_{\mathrm{N}}^2 m_{\mathrm{N1}}^2$, the second term is suppressed as r_{N}^{-2} and we reach a decoupling limit.[5] In this limit the amplitude reduces to that of a single HNL while the light neutrino masses, and thus their contribution to LNV effects, remain exactly cancelled. This converging behaviour can be seen in the (differential)

[4] In the most general case the only requirement is that the complex phases between $V_{\ell 1}$ and $V_{\ell 2}$ be orthogonal. But since in this study any complex phases would cancel out in the final observables, we can choose the most simple case of "+" and a real $V_{\ell 1}$ without loss of generality. Generally, such phases could also be absorbed in the definition of fields in Eq. (1.14).

[5] This corresponds to $M_{\mathrm{ww}}^2 \ll m_{\mathrm{N2}}^2$, so that we can treat the second HNL by means of effective field theory. As explained in II.E of Kersten-Smirnov's symmetry discussions [50], this results in significant running of light neutrino masses.

cross section in (Fig. 2.4) Fig. 2.5 of the $W^\pm W^\pm \to \ell^\pm \ell^\pm$ process. However, it is important to note that $r_\mathrm{N} \to \infty$ is not a physical limit. Not only do concerns like the running of light neutrino masses play a role here, but under Eq. (1.23) the heavier HNL will breach a perturbativity limit in the Yukawa couplings (see Section 1.2.1), thus breaking the assumption of weak Yukawa coupling in the deduction of the theory.

2.2.2 Observables

Differential Cross Section

In the limit of $M_\mathrm{ww}^2 \ll m_\mathrm{N}^2$, the t (u) dependence of the amplitude will always be overshadowed by the HNL masses. This results in differential cross sections which are essentially constant with respect to t. For larger mass ratios r_N the cancellation between the two HNL contributions becomes less significant. Hence, the numerical value of the differential cross section goes from 0 in the fully degenerate case to that of a single HNL with growing r_N. This behaviour is shown in Figs. E.4c and E.4d.

More interesting effects can be observed, when both $m_\mathrm{N1}^2, m_\mathrm{N2}^2 \lesssim M_\mathrm{ww}^2$. We will investigate only a region around small values of $|t|$. The rest of the curve follows mainly from mirror symmetry and absence of divergences. In order to investigate this region we will parametrise $-t$ around its minimal value as

$$t = \lambda(-t)_\mathrm{min} = -\lambda \varrho_{W/\mathrm{N}} m_\mathrm{N}^2, \tag{2.13}$$

with $1 \leq \lambda \sim$ few as a dimensionless parameter, and $\varrho_{W/\mathrm{N}} = \frac{m_W^4}{m_\mathrm{N}^2 M_\mathrm{ww}^2} \ll 1$ as a small parameter.[6] The differential cross section can be expanded as

$$\frac{\mathrm{d}\sigma}{\mathrm{d}t} = \frac{|V_{\ell\mathrm{N}}|^4 G_F^2}{9\pi} \frac{(r_\mathrm{N}^2 - 1)^2 \varrho_{W/\mathrm{N}}}{r_\mathrm{N}^4} + \mathcal{O}\left(\varrho_{W/\mathrm{N}}^2\right). \tag{2.14}$$

Close to the Dirac-limit $r_\mathrm{N} \to 1$, the differential cross section vanishes as $\mathrm{d}\sigma/\mathrm{d}t \propto (r_\mathrm{N} - 1)^2$. Further, we notice that all λ dependence is at least suppressed as $\varrho_{W/\mathrm{N}}^2$, resulting in slowly varying functions. Taking the gradient with respect to λ we find this suppression more explicitly as

$$\frac{\partial}{\partial\lambda}\frac{\mathrm{d}\sigma}{\mathrm{d}t} = \frac{|V_{\ell\mathrm{N}}|^4 G_F^2}{9\pi m_W^2} \frac{(r_\mathrm{N}^2 - 1)^2}{r_\mathrm{N}^4} \left(m_\mathrm{N}^2 - 2m_W^2\left(1 + r_\mathrm{N}^{-2}\right)\right) \varrho_{W/\mathrm{N}}^2 + \mathcal{O}\left(\varrho_{W/\mathrm{N}}^3\right). \tag{2.15}$$

[6] Formally, this could be extended to $1 \leq \lambda \leq \frac{M_{WW}^4}{m_W^4}$, but we will limit the discussion here to the extreme point of $\lambda \to 1$.

As expected from the amplitude discussion above, the t-dependence is strongly suppressed for large m_{N}. However, from this explicit form we can see that the m_{N} suppression already takes place for $m_W^2 \ll m_{\mathrm{N}}^2$ rather than only from $M_{\mathrm{WW}}^2 \ll m_{\mathrm{N}}^2$. We also find that the gradient flips sign at

$$r_{\mathrm{N,crit.}} = \frac{\sqrt{2} m_W}{\sqrt{m_{\mathrm{N}}^2 - 2m_W^2}}. \tag{2.16}$$

This can be observed in Fig. 2.4, which shows the differential cross section of the $W^{\pm}W^{\pm} \to \ell^{\pm}\ell^{\pm}$ process as a function of the Mandelstam variable $\sqrt{-t}$ for the lighter HNL mass $m_{\mathrm{N}} = 150\,\mathrm{GeV}$ (Fig. 2.4a), and $m_{\mathrm{N}} = 1500\,\mathrm{GeV}$ (Fig. 2.4b) for different mass ratios r_{N}.
For $m_{\mathrm{N}} = 150\,\mathrm{GeV}$ we find at leading order $r_{\mathrm{N,crit.}} = 1.16$, which agrees with the numerical values shown in the plot, where the extremal gradient flips sign between $r_{\mathrm{N}} = 1.1$ and $r_{\mathrm{N}} = 2$. However, the plot importantly also shows that higher order corrections flip the gradient for larger values of λ, resulting in a non-trivial angular distribution.
For $m_{\mathrm{N}} = 1500\,\mathrm{GeV}$ there is no solution $r_{\mathrm{N,crit.}} > 1$, so that the cross section is concave for all r_{N}. We furthermore note that any angular dependence is strongly suppressed, just as Eq. (2.14) suggests.

For small m_{N} ($\sim 13\,\mathrm{GeV}$ for $M_{\mathrm{WW}} = 490\,\mathrm{GeV}$) the above expansion breaks down. Expanding instead in $\varrho_{W/\mathrm{N}}^{-1}$ we find

$$\frac{\mathrm{d}\sigma}{\mathrm{d}t} = \frac{|V_{\ell\mathrm{N}}|^4 G_F^2}{9\pi} \frac{(r_{\mathrm{N}}^2 - 1)^2 m_{\mathrm{N}}^{12} \left(m_{\mathrm{N}}^2 \left(r_{\mathrm{N}}^2 + 1\right) - 2m_W^2\right)^2 \varrho_{W/\mathrm{N}}^{-3}}{\lambda^4 m_W^{16}} + \mathcal{O}\left(\varrho_{W/\mathrm{N}}^{-4}\right), \tag{2.17}$$

with a gradient of

$$\frac{\mathrm{d}\sigma}{\mathrm{d}t} = -\frac{4|V_{\ell\mathrm{N}}|^4 G_F^2}{9\pi} \frac{(r_{\mathrm{N}}^2 - 1)^2 m_{\mathrm{N}}^{12} \left(m_{\mathrm{N}}^2 \left(r_{\mathrm{N}}^2 + 1\right) - 2m_W^2\right)^2 \varrho_{W/\mathrm{N}}^{-3}}{\lambda^5 m_W^{16}} + \mathcal{O}\left(\varrho_{W/\mathrm{N}}^{-4}\right). \tag{2.18}$$

Importantly, in this expansion, there is no possible sign flip of the gradient, so that the curves for all r_{N} follow the λ^{-4} shape. An example for this can be seen for $m_{\mathrm{N}} = 10\,\mathrm{GeV}$ in Fig. E.4a.

Cross Section

Figure 2.5 shows the total cross section of $W^{\pm}W^{\pm} \to \ell^{\pm}\ell^{\pm}$ as a function of m_{N1} for different mass ratios r_{N} at a center of mass energy $\sqrt{M_{\mathrm{WW}}^2} = 490\,\mathrm{GeV}$. We see

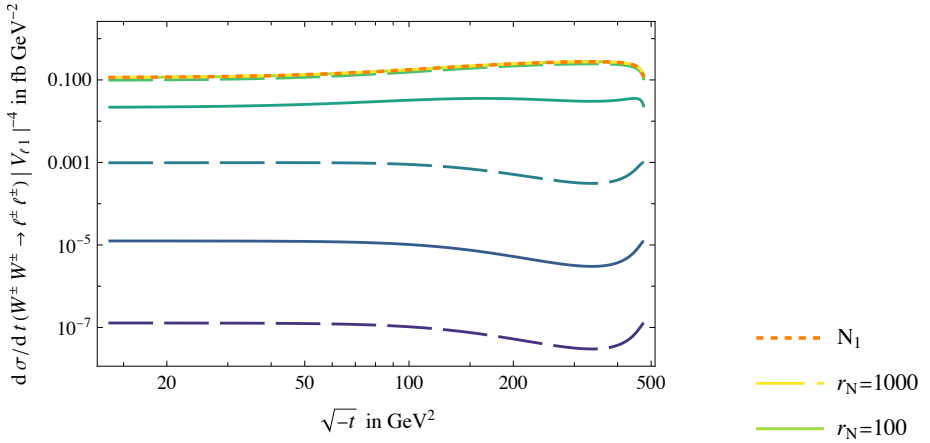

(a) $m_{N1} = 150\,\mathrm{GeV}$

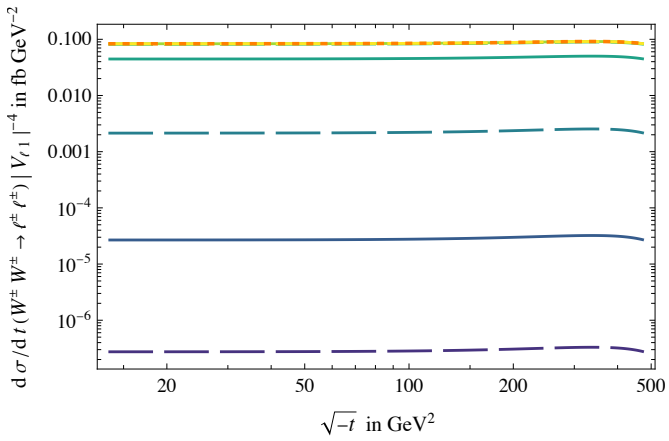

(b) $m_{N1} = 1500\,\mathrm{GeV}$

Figure 2.4: Total differential cross section of $W^\pm W^\pm \to \ell^\pm \ell^\pm$ for a QDL HNL pair with a mass ratio $r_N = \frac{m_{N2}}{m_{N1}}$. The mixing angle of the first HNL $V_{\ell 1}$ factors out of the observable, while $V_{\ell 2}$ is adjusted to account for the exact cancellation. The lighter of the two HNL masses $m_{N1} = 150\,\mathrm{GeV}$ (a), and $m_{N1} = 1500\,\mathrm{GeV}$ (b). The centre of mass energy is 490 GeV.

that the $(r_N - 1)^2$ dependence of the differential cross section directly translates to the total cross section, in that for $r_N \simeq 1$, the numerical value increases by about two orders of magnitude for every order of magnitude we move away from 1. All of the curves tend toward 0 for $m_N \to 0$ in accordance with the indistinguishability-theorem. As expected from the amplitude level, and as can be seen from Eq. (2.14), for $M_{WW}^2 \ll m_N^2$ the cross section vanishes as m_N^{-2}. With growing r_N, the maximum of the curve shifts from around $m_N = \sqrt{M_{WW}^2}$ toward $\sqrt{\frac{1}{2}M_{WW}^2}$. In the limit of $r_N \to \infty$,

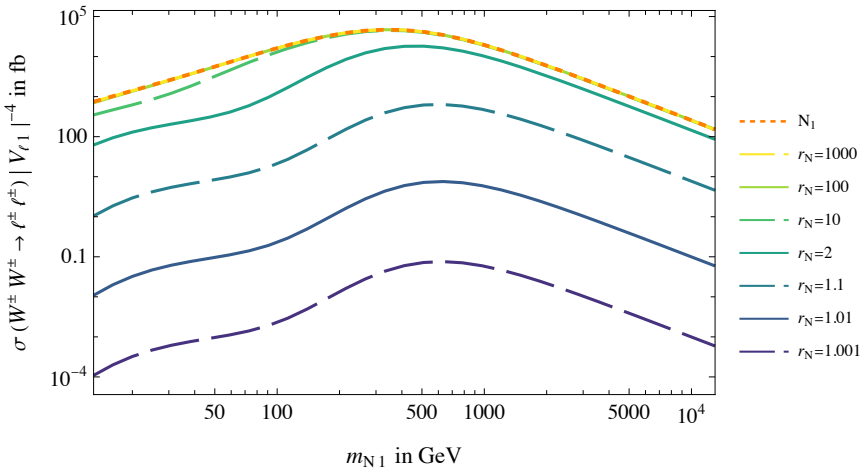

Figure 2.5: Total cross section of $W^\pm W^\pm \to \ell^\pm \ell^\pm$ scattering for a QDL HNL pair with a mass ratio $r_\mathrm{N} = \frac{m_{\mathrm{N}2}}{m_{\mathrm{N}1}}$. The mixing angle of the first HNL $V_{\ell 1}$ factors out of the observable, while $V_{\ell 2}$ is adjusted to account for the exact cancellation. The centre of mass energy is 490 GeV.

we find the completely decoupled case of a single HNL (shown in dashed orange), where already for $r_\mathrm{N} = 100$ the two curves become indistinguishable at the scales shown.

2.3 Full Four Majorana State Model

A very convenient formulation to ensure that mixing angles V generate light neutrino mass states compatible with neutrino oscillation data for any choice of m_N is the Casas-Ibarra parametrisation [123, 124]

$$V^{\mathrm{CI}} = iU\mathrm{diag}(m_{\nu 1}, m_{\nu 2}, m_{\nu 3})^{1/2}\Omega\mathrm{diag}(m_{\mathrm{N}1}, ..., m_{\mathrm{N}\mathcal{N}})^{-1/2}. \tag{2.19}$$

Here Ω is an orthogonal $3 \times \mathcal{N}$ matrix holding all degrees of freedom of the model that are not fixed by the PMNS matrix U, the heavy mass states $m_{\nu i}$, and the light mass states $m_{\nu i}$. To account for neutrino oscillations with two HNLs, we require the lightest neutrino mass state to be massless. The most general explicit form of Ω in case of normal hierarchy (NH) or inverted hierarchy (IH) is given by

$$\Omega = \begin{pmatrix} 0 & 0 \\ \cos\omega & \sin\omega \\ -\xi\sin\omega & \xi\cos\omega \end{pmatrix} \text{(NH)}, \quad \begin{pmatrix} \cos\omega & \sin\omega \\ -\xi\sin\omega & \xi\cos\omega \\ 0 & 0 \end{pmatrix} \text{(IH)}, \tag{2.20}$$

with $\xi = \pm 1$, and $\omega \in \mathbb{C}$. The parity ξ can be chosen by simultaneous redefinition of the fields and ω so that we will choose $\xi = +1$ without loss of generality. Given that recent data indicates a preference for normal ordering (νFIT at 2.7σ [125], see [126] for discussion), in the following we present the case of normal hierarchy.

In the case of two HNLs and NH, we can write the two mixing angles of this parametrisation explicitly as

$$\begin{aligned} V_{\ell 1}^{\mathrm{CI}} &= i\frac{U_{\ell 2}\sqrt{m_{\nu 2}}\cos\omega - U_{\ell 3}\sqrt{m_{\nu 3}}\sin\omega}{\sqrt{m_{\mathrm{N1}}}} \\ V_{\ell 2}^{\mathrm{CI}} &= i\frac{U_{\ell 2}\sqrt{m_{\nu 2}}\sin\omega + U_{\ell 3}\sqrt{m_{\nu 3}}\cos\omega}{\sqrt{m_{\mathrm{N2}}}}. \end{aligned} \tag{2.21}$$

For a small discussion of what changes when considering the inverted hierarchy case see Appendix B.

2.3.1 Amplitude Level

In this scenario, the amplitude of the $W^{\pm}W^{\pm} \to \ell^{\pm}\ell^{\pm}$ t-channel will be proportional to

$$i\mathcal{A}_t \propto \sum_I V_{\ell I}^2 J^{\alpha\beta}\left(t, m_{\mathrm{N}I}\right) + \sum_i U_{\ell i}^2 J^{\alpha\beta}\left(t, m_{\nu i}\right), \tag{2.22}$$

where $V_{\ell I}$ are the mixing angles, $U_{\ell i}$ is the PMNS matrix, and $J^{\alpha\beta}$ the LNV current (see Eq. (2.4)). Using the Casas-Ibarra parametrisation we get

$$\begin{aligned} i\mathcal{A}_t \propto & \frac{\left(U_{\ell 2}\sqrt{m_{\nu 2}}\cos\omega - U_{\ell 3}\sqrt{m_{\nu 3}}\sin\omega\right)^2}{m_{\mathrm{N1}}} J^{\alpha\beta}\left(t, m_{\mathrm{N1}}\right) \\ & + \frac{\left(U_{\ell 2}\sqrt{m_{\nu 2}}\sin\omega + U_{\ell 3}\sqrt{m_{\nu 3}}\cos\omega\right)^2}{m_{\mathrm{N2}}} J^{\alpha\beta}\left(t, m_{\mathrm{N2}}\right) \\ & - U_{\ell 2}^2 J^{\alpha\beta}\left(t, m_{\nu 2}\right) - U_{\ell 2}^2 J^{\alpha\beta}\left(t, m_{\nu 3}\right). \end{aligned} \tag{2.23}$$

In the limit of $m_{\nu i}^2 \ll |t|_{\min}$ and after some tedious algebra, we again find an expression like we get from the first flavour basis expansion (see Fig. E.2)

$$\begin{aligned} i\mathcal{A}_t \propto & \frac{m_{\mathrm{N1}}^2}{t}\frac{\left(U_{\ell 2}\sqrt{m_{\nu 2}}\cos\omega - U_{\ell 3}\sqrt{m_{\nu 3}}\sin\omega\right)^2}{m_{\mathrm{N1}}} J^{\alpha\beta}\left(t, m_{\mathrm{N1}}\right) \\ & + \frac{m_{\mathrm{N2}}^2}{t}\frac{\left(U_{\ell 2}\sqrt{m_{\nu 2}}\sin\omega + U_{\ell 3}\sqrt{m_{\nu 3}}\cos\omega\right)^2}{m_{\mathrm{N2}}} J^{\alpha\beta}\left(t, m_{\mathrm{N2}}\right). \end{aligned} \tag{2.24}$$

As we operate in the normal hierarchy and set the smallest neutrino mass to 0, we have $m_{\nu 1} = 8.6\,\text{meV}$ and $m_{\nu 1} = 50\,\text{meV}$ [125], so that the expansion condition is even better met than in the case discussed in Eq. (2.7).

Reintroducing the mass ratio r_N and dropping indices on $m_{\text{N}I}$ with $m_\text{N} = m_{\text{N}1}$, this reads

$$\begin{aligned} i\mathcal{A}_t \propto \frac{m_\text{N}}{t} \Bigg(& \left(U_{\ell 2}\sqrt{m_{\nu 2}}\cos\omega - U_{\ell 3}\sqrt{m_{\nu 3}}\sin\omega\right)^2 \\ & + \left(U_{\ell 2}\sqrt{m_{\nu 2}}\sin\omega + U_{\ell 3}\sqrt{m_{\nu 3}}\cos\omega\right)^2 \frac{t - m_\text{N}^2}{r_\text{N}^{-2}t - m_\text{N}^2} \Bigg) J^{\alpha\beta}\left(t, m_\text{N}\right). \end{aligned} \tag{2.25}$$

In the degeneracy limit of $r_\text{N} \to 1$ this becomes

$$\begin{aligned} i\mathcal{A}_t \propto \frac{m_\text{N}}{t} \Bigg(& m_{\nu 2}U_{\ell 2}^2 + m_{\nu 3}U_{\ell 3}^2 \\ & + \frac{2(r_\text{N} - 1)t\left(\sqrt{m_{\nu 2}}U_{\ell 2}\sin\omega + \sqrt{m_{\nu 3}}U_{\ell 3}\cos\omega\right)^2}{t - m_\text{N}^2} \\ & + \mathcal{O}\left((r_\text{N} - 1)^2\right) \Bigg) J^{\alpha\beta}\left(t, m_\text{N}\right), \end{aligned} \tag{2.26}$$

so that any possible enhancement of the amplitude is suppressed as $\mathcal{O}(r_\text{N} - 1)$. However, we note that unlike in the quasi-Dirac limit (see 2.2.1), in the degeneracy limit of the Casas-Ibarra parametrisation we do not obtain a necessarily vanishing amplitude. Rather, it reduces to the case of a single HNL (see Eq. (2.6)) with a mixing angle of

$$\left(V_{\ell\text{N}}^{\text{CI},r_\text{N}\to 1}\right)^2 = \frac{m_{\nu 2}U_{\ell 2}^2 + m_{\nu 3}U_{\ell 3}^2}{m_\text{N}}, \tag{2.27}$$

at the seesaw line, similar to the condition used in our single HNL analysis in Section 2.1.

In the strongly hierarchical limit of $r_\text{N} \to \infty$ this becomes

$$\begin{aligned} i\mathcal{A}_t \propto \frac{m_\text{N}}{t} \Bigg(& \left(U_{\ell 2}\sqrt{m_{\nu 2}}\cos\omega - U_{\ell 3}\sqrt{m_{\nu 3}}\sin\omega\right)^2 \\ & - \left(U_{\ell 2}\sqrt{m_{\nu 2}}\sin\omega + U_{\ell 3}\sqrt{m_{\nu 3}}\cos\omega\right)^2 \frac{t - m_\text{N}^2}{m_\text{N}^2} \\ & + \mathcal{O}\left(r_\text{N}^{-2}\right) \Bigg) J^{\alpha\beta}\left(t, m_\text{N}\right). \end{aligned} \tag{2.28}$$

This corresponds to the case of a single, potentially enhanced HNL and the two light mass states, the contribution of which can also be enhanced. We note that for $M_{\mathrm{WW}}^2 \ll m_{\mathrm{N}}^2$ this becomes

$$i\mathcal{A}_t \propto \frac{m_{\mathrm{N}}}{t}\left(m_{\nu 2}U_{\ell 2}^2 + m_{\nu 3}U_{\ell 3}^2\right) J^{\alpha\beta}(t, m_{\mathrm{N}}^2) + \mathcal{O}\left(r_{\mathrm{N}}^{-2}, \frac{M_{\mathrm{WW}}^2}{m_{\mathrm{N}}^2}\right), \tag{2.29}$$

where all possible enhancement $\mathrm{Im}\,\omega$ is suppressed as well.

2.3.2 Observables

Using νFIT data [127, 125] for the numerical values of the PMNS matrix U, as well as the light neutrino mass splitting, we can now numerically evaluate the physical observables. The exact numerical values used will again be those $W^+W^+ \to e^+e^+$, while we stress that the numerical values for other leptons ℓ will yield the same results up to ratios of their PMNS entries $(U_{\ell i}/U_{ei})^4$.

Differential Cross Section

In the same parametrisation of t as used above (Eq. (2.13)), we again expand the differential cross section in $\varrho_{W/\mathrm{N}} = \frac{m_W^4}{m_{\mathrm{N}}^2 M_{\mathrm{WW}}^2}$. In order to shorten the notation, we define $m_\nu = U_{\ell 2}^2 m_{\nu 2} + U_{\ell 3}^2 m_{\nu 3}$ and $\Delta m_\nu = U_{\ell 2}^2 m_{\nu 2} - U_{\ell 3}^2 m_{\nu 3}$. Assuming a purely imaginary ω this yields[7]

$$\begin{aligned}\frac{\mathrm{d}\sigma}{\mathrm{d}t} =& \frac{G_F^2}{9\pi}\frac{m_\nu^2}{\varrho_{W/\mathrm{N}}\lambda^2 m_{\mathrm{N}}^2} \\ &+ \frac{G_F^2\left(m_\nu^2\left((\lambda+3)\,r_{\mathrm{N}}^2 m_{\mathrm{N}}^2 - \lambda\left(r_{\mathrm{N}}^2+1\right)m_W^2\right)\right)}{9\pi\lambda^2 r_{\mathrm{N}}^2 m_{\mathrm{N}}^2 m_W^2} \\ &- \frac{G_F^2\left(r_{\mathrm{N}}^2-1\right)\Delta m_\nu m_\nu \cosh(2\,\mathrm{Im}\,\omega)}{9\pi\lambda r_{\mathrm{N}}^2 m_{\mathrm{N}}^2} + \mathcal{O}\left(\varrho_{W/\mathrm{N}}\right).\end{aligned} \tag{2.30}$$

We note that the dependence at $\lambda \to 1$ is quadratic in t^{-1} at leading order. Meanwhile, for large values of $\mathrm{Im}\,\omega$ last term in Eq. (2.30) becomes dominant, yielding a constant t dependence. The effect of this is more evident when taking the gradient

[7] As explained above, $\mathrm{Im}\,\omega$ controls the scale of the mixing angle, so that effects caused by $\mathrm{Re}(\omega)$ become secondary for large $\mathrm{Im}\,\omega$.

with respect to λ at the lower extremal value of $|t|$, which yields

$$\begin{aligned}\frac{\partial}{\partial\lambda}\frac{\mathrm{d}\sigma}{\mathrm{d}t} =& -\frac{2G_F^2 m_\nu^2}{9\pi\lambda^3\varrho_{W/\mathrm{N}}m_\mathrm{N}^2}\\ &-\frac{G_F^2 m_\nu^2\left((\lambda+6)r_\mathrm{N}^2 m_\mathrm{N}^2-\lambda\left(r_\mathrm{N}^2+1\right)m_W^2\right)}{9\pi\lambda^3 r_\mathrm{N}^2 m_\mathrm{N}^2 m_W^2}\\ &+\frac{G_F^2\left(\left(r_\mathrm{N}^2-1\right)\cosh(2\,\mathrm{Im}\,\omega)\Delta m_\nu m_\nu\right)}{9\pi\lambda^2 r_\mathrm{N}^2 m_\mathrm{N}^2}+O\left(\varrho_{W/\mathrm{N}}\right).\end{aligned} \tag{2.31}$$

We, thus, expect the gradient to flip for a mass ratio of

$$\frac{r_\mathrm{N}^2}{r_\mathrm{N}^2-1}\simeq\cosh(\mathrm{Im}\,\omega)\lambda\varrho_{W/\mathrm{N}}\frac{\Delta m_\nu}{m_\nu}. \tag{2.32}$$

We note that this can only be fulfilled for $1<\cosh(\mathrm{Im}\,\omega)\lambda\varrho_{W/\mathrm{N}}\frac{\Delta m_\nu}{m_\nu}$, resulting in a minimal enhancement $\mathrm{Im}\,\omega$ required to observe this effect (see for example Fig. E.6).

In the limit of $\varrho_{W/N}^{-1}\ll 1$ this becomes instead

$$\begin{aligned}\frac{\mathrm{d}\sigma}{\mathrm{d}t}=\frac{m_\mathrm{N}^{10}G_F^2}{36\pi\lambda^4 m_W^{16}}\Bigg(&\left(r_\mathrm{N}^2-1\right)\cosh(2\,\mathrm{Im}\,\omega)\left(m_\mathrm{N}^2\left(r_\mathrm{N}^2+1\right)-2m_W^2\right)\Delta m_\nu\\ &-\left(m_\mathrm{N}^2\left(r_\mathrm{N}^4+1\right)-2\left(r_\mathrm{N}^2+1\right)m_W^2\right)m_\nu\Bigg)^2\varrho_{W/\mathrm{N}}^{-3}\\ &+\mathcal{O}\left(\varrho_{W/\mathrm{N}}\right)^{-4},\end{aligned} \tag{2.33}$$

which is manifestly convex for any $\mathrm{Im}\,\omega$ or r_N. An example of this can be seen in Fig. E.5a, where also the N_1-contribution is convex as explained above.

Figure 2.6a shows the differential cross section of $W^\pm W^\pm\to\ell^\pm\ell^\pm$ in the Casas-Ibarra parametrisation of the Mixing angles as a function of the Mandelstam variable t for different mass ratios r_N at $\omega=0$, $m_{\mathrm{N}1}=150\,\mathrm{GeV}$ and $\sqrt{M_{WW}^2}=490\,\mathrm{GeV}$. As expected from the discussion above, for all mass ratios r_N (shown in dark purple to yellow) the differential cross section is divergent towards the extremal values of t. Furthermore, in the absence of any enhancement $\mathrm{Im}\,\omega$ the process is dominated by the contribution of the light neutrino mass states (dash-dotted in dark green). The share of $U_{\ell\nu_i}\sqrt{m_{\nu i}}$ are assigned to the N_I depend on the choice of $\mathrm{Re}(\omega)$ (see Eq. (2.19)). Thus, the two graphs for N_1 and N_2 (dashed orange and dashed red respectively) should be understood as extremal values of a band in which to expect the individual contribution of the lighter of the two heavy mass states.

Figure 2.6b also shows the differential cross section of $W^\pm W^\pm\to\ell^\pm\ell^\pm$ in the Casas-Ibarra parametrisation, but with a mixing enhancement of $\omega=5i$. We see

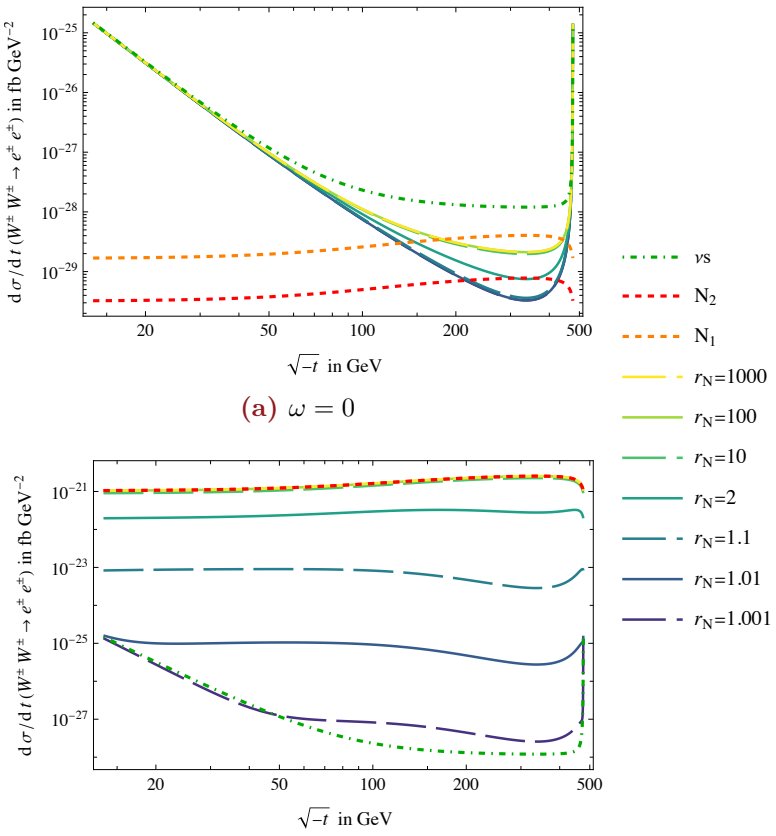

(a) $\omega = 0$

(b) $\omega = 5i$

Figure 2.6: Total differential cross section of $W^\pm W^\pm \to \ell^\pm \ell^\pm$ scattering using the Casas-Ibarra parametrisation of the HNL mixing angles with $\omega = 0$ (a) and $\omega = 5i$ (b). Here $r_N = \frac{m_{N2}}{m_{N1}}$ is the mass ratio. The lighter of the two HNL masses $m_{N1} = 150\,\mathrm{GeV}$ and the centre of mass energy is 490 GeV.

that for almost degenerate HNLs the differential cross section is convex, while for more hierarchical HNLs (from $r_N \simeq 2$) the curve approaches that of the single HNL case. The differences between N_1 and N_2 due to the choice of $\mathrm{Re}(\omega)$ are vanishingly small on the scales shown here.

For even stronger enhancement, the effects due to light neutrinos become negligible and the curves become qualitatively similar to those of the qDL case (c.f. Section 2.2 and Fig. 2.4a).

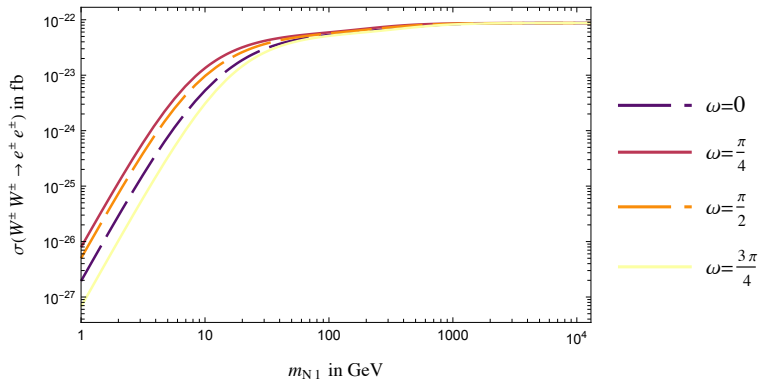

(a) Real Casas-Ibarra parameters

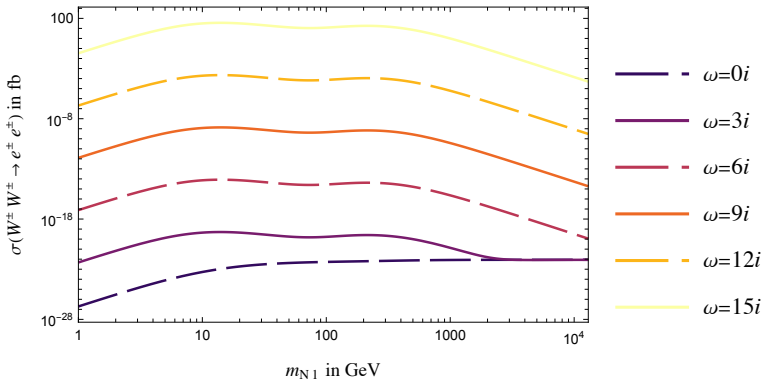

(b) Imaginary Casas-Ibarra parameters

Figure 2.7: Total cross section of $W^\pm W^\pm \to \ell^\pm \ell^\pm$ scattering using the Casas-Ibarra parametrisation of the HNL mixing angles for different real (a) and imaginary (b) Casas-Iabarra parameters. The mass ratio $r_N = \frac{m_{N2}}{m_{N1}} = 2$ and the centre of mass energy is 490 GeV.

Cross Section

Figure 2.7a shows the total cross section of $W^\pm W^\pm \to \ell^\pm \ell^\pm$ using the Casas-Ibarra parametrisation (Eq. (2.19)) for a mass ratio of $r_N = 2$, varying the Casas-Ibarra parameter ω for a range of real values. For all values of ω, we observe a convergence with the numerical value determined by the light mass states for large masses ($m_N > 1000 \simeq 2M_{WW}$). Furthermore, we note a cancellation between light and heavy mass states for small m_N similar to the case of a single HNL (see Fig. 2.3). The splitting for smaller values of m_N is due to the way ω distributes the $U_{\ell\nu}\sqrt{m_\nu}$ in the mixing of non-degenerate ($r_N = 2$) HNLs, giving smaller or larger weight to the heavier — and therefore more suppressed — N_2. However, for $m_N \to m_\nu$ the cross section vanishes

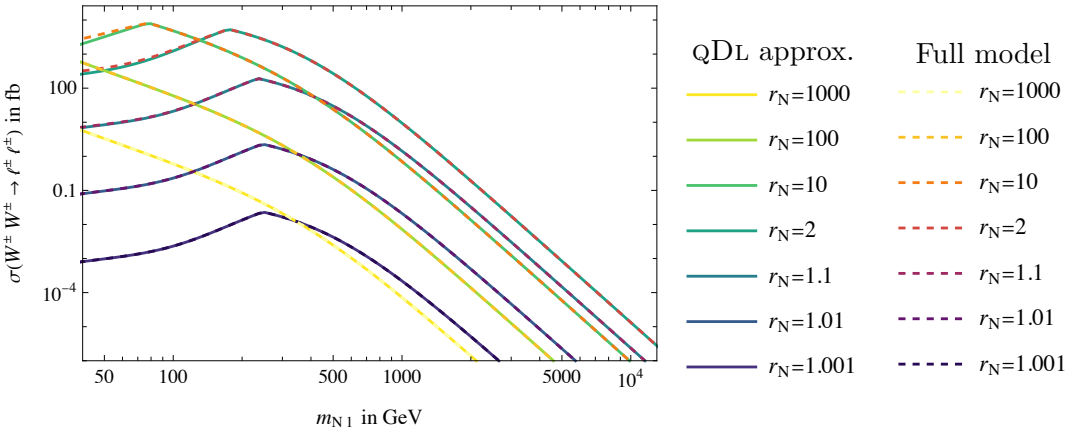

Figure 2.8: Comparison of $W^\pm W^\pm \to \ell^\pm \ell^\pm$ cross sections between QDL and fully realistic two HNL neutrino sector model. The data is shown at a maximally admissible mixing angle $V_{\ell 1}$ according to Section 1.2.1.

for all values of ω. The portrayed dependence on $\mathrm{Re}(\omega)$ is π-periodic, as can also be seen from Eq. (2.19).

By contrast, Fig. 2.7b shows the total cross section of $W^\pm W^\pm \to \ell^\pm \ell^\pm$ for a range of purely imaginary ωs permitted by the limit of $|V_{\ell N}| < 1$. Again all curves will eventually meet the numerical value determined by the light mass states for large values of m_{N1}. However, the range at which the heavy mass states dominate is greatly extended depending on the enhancement factor $\mathrm{Im}\,\omega$. This behaviour is due to the constant enhancement by $\mathrm{Im}\,\omega$ becoming suppressed by very large m_N as prescribed by the Casas-Ibarra parametrisation (see Eq. (2.19)). We can also observe some non-trivial interference between the enhanced HNL contributions for $m_{N1} \simeq m_W = 80\,\mathrm{GeV}$. The interference is especially non trivial, as m_{N2} is right at the minimum centre of mass energy $2m_W$ due to the chosen mass ratio r_N, potentially making terms significant that can otherwise be neglected.

In the limit of large $V_{\ell 1}$, the cross sections of the QDL model and in Casas-Ibarra parametrisation become indistinguishable (see Fig. 2.8) to the precision of this analysis. This means that for large mixing angles, $m_{N1} m_\nu^{-1} \ll \cosh(2\,\mathrm{Im}\,\omega)$, the QDL model is a good approximation of a more realistic neutrino sector model.

Extension to Same Sign Di-Lepton Signal at Colliders

3

In this chapter we will translate our findings from Chapter 2 to the specific case of W boson fusion in $pp \to \ell^\pm\ell^\pm jj$ scattering (see Fig. 1.4a). To mark the pp level cross sections we will mark them with $pp \to \ell^\pm\ell^\pm jj$. However, this does not include contributions coming from the Drell-Yan process, which shares the same signature (see Fig. 1.4b). Unlike in Chapter 2, where the $\pm$ in $W^\pm W^\pm \to \ell^\pm\ell^\pm$ signified that both possibilities lead to equally sized cross sections, $pp \to \ell^\pm\ell^\pm jj$ will denote that we add both contributions to a combined cross section. This does not correspond to a simple factor of 2, as the parton structure of the proton favours the "++" over the "−−" process.

After explaining the methodology of obtaining our proton-proton level cross sections (Section 3.1), we will analyse the detection prospects at current (Large Hadron Collider, LHC, Section 3.2) and future (Future Circular Collider in the hadron-hadron stage, FCC-hh, Section 3.3) colliders. Both of these colliders are/will be circular synchrotron accelerators capable of high energy pp collisions. The experimental parameters of these machines constitute the best chance for the potential observation of $pp \to \ell^\pm\ell^\pm jj$ for the foreseeable future.[1]

[1]The current timeline predicts that after the high luminosity upgrade to the LHC, it will reach its target integrated luminosity some time around 2040 [128]. Meanwhile the FCC-hh is scheduled to become operational in 2062, reaching its predicted integrated luminosity after 25 years [129].

3.1 Methodology

As already mentioned in Section 1.3.2, the W *boson fusion* (Fig. 1.4a) process is distinct from the *Drell-Yan* process (Fig. 1.4b), due to the antiquarks in initial and final state of DY. We can thus safely ignore DY in our calculations, even though they share the same collider signature $pp \to \ell^\pm\ell^\pm jj$.

As we saw in Section 2.3, a qDL model becomes a good approximation of a neutrino sector model involving light neutrino masses compatible with oscillation and cosmological data for large mixing angles ($m_{\mathrm{N}1} m_\nu^{-1} \ll \cosh(2\,\mathrm{Im}\,\omega)$). As we will see, at currently proposed hadron colliders only those mixing angles are within reach. Therefore, we will limit ourselves to the qDL model for the following estimates, as it is inherently numerically simpler. For pp level cross sections in the case of one HNL and two HNLs in the Casas-Ibarra parametrisation find Appendices A and B.

An accurate description of QCD effects involved in the WBF process is beyond the scope of this thesis. Instead we will use the effective W approximation (see Section 1.4).

In order to use this approximation, the cross section has to be decomposed into longitudinal and transversal components. This is implemented at amplitude level using the corresponding sum relations on the polarisation vectors. Subsequently, the polarised cross sections are folded with effective PDFs $f^\lambda_{W/p}$ as described in Section 1.4. These relate a W's energy to that of its respective mother-proton in the pp collision through the momentum fraction $x_{(i)}$.

In the case of WBF we have (in the notation of Section 1.4.2)

$$m_a = m_b = m_W, \quad \text{and} \quad m_X^2 + m_Y^2 + m_Z^2 = 4m_\ell^2 + \sum_i {m_{ji}^2}^{\min}, \tag{3.1}$$

with ${m_{ji}^2}^{\min}$ being the minimal invariant mass of of the ith jet. If we do not apply any cuts on the jets minimal invariant mass, we have $4m_W^2 > 4m_\ell^2 + {m_{j1}^2}^{\min} + {m_{j2}^2}^{\min}$ for all lepton generations ℓ.[2] Under a change of variables ($x_1x_2 \to \tau, x_1 \to \xi$) and summing over the polarisation states described in Section 1.4.1, we write Eq. (1.42) for WBF in the simple form

$$\sigma_{pp\to\ell^\pm\ell^\pm jj}(s) = 2 \sum_{\substack{\lambda,\lambda'=\{\mathrm{T},\mathrm{L}\}\\ \kappa=\pm}} \int_{\tau_{\min}}^1 \mathrm{d}\tau \int_\tau^1 \frac{\mathrm{d}\xi}{\xi} f^{\lambda 1}_{W^\kappa/p}\left(\frac{\tau}{\xi}\right) f^{\lambda 2}_{W^\kappa/p}(\xi)\sigma_{W^\kappa W^\kappa\to\ell^\kappa\ell^\kappa}(\tau s), \tag{3.2}$$

[2] Indeed the cuts Eq. (3.5) imposed on in the detector simulation demand that the transverse momentum $p_T^j > 20\,\mathrm{GeV}$, so that this relation still holds.

where the sum over polarisations λ includes longitudinal (L) and transversal (T) polarisations, the sum over W electric charges κ includes $+$ and $-$, and $\tau_{\text{min}} = 4m_W^2 s_{pp}^{-1}$.

In Section 3.1.1 we show a decomposition by polarisation as mentioned in the paragraphs above, along with a discussion of the EWA. We show that the EWA can only be safely applied for $m_{\text{N1}} \gtrsim$ several 100 GeV.

We then compare the resulting pp level cross sections for the case of a single HNL in the phenomenological type-I seesaw model to those derived in MadGraph5_aMC at NLO (MG5aMC) analogously to the NLO study of WBF in this framework by Fuks et al. [101]. We find good agreement for HNL masses $m_{\text{N}} \gtrsim$ few TeV, but larger discrepancies for smaller masses in the 100 GeV range. To extend the meaningful range of our results, we will use this comparison to rescale the EWA results. This has the added benefit of applying detector motivated cuts on the jets of the signal, excluding too large pseudorapidities.

Using the thus derived pp level cross sections, we will give an estimate for maximal collider event rates and parameter reach in the qDL framework.

This workflow employed in calculating pp level quantities can be summarised in the following way:

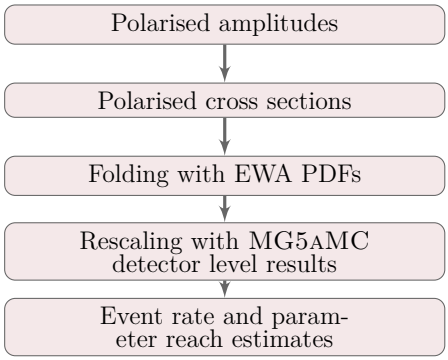

3.1.1 Effective W Approximation

Polarisation Decomposition of a quasi-Dirac-like HNL pair

In this section, we present the polarised cross sections of $W^\pm W^\pm \to \ell^\pm \ell^\pm$ that go into the effective W approximation. The decompositions were performed using the

polarisation sum relations (in unitary gauge)

$$\sum_{\lambda} \varepsilon_k^{\alpha} \varepsilon^{*\beta}_k = -\eta^{\alpha\beta} \qquad \text{(transversal)} \tag{3.3a}$$

$$\sum_{\lambda} \varepsilon_k^{\alpha} \varepsilon^{*\beta}_k = \frac{k^{\alpha} k^{\beta}}{m_W^2} \qquad \text{(longitudinal)} \tag{3.3b}$$

for the W polarisation vectors ε_k with momentum k to obtain polarised squared amplitudes.

Using this decomposition, we can identify the interaction of the two HNLs in a qDl pair at polarised WW cross section level. This is shown in Fig. 3.1 for a mass ratio $r_{\mathrm{N}} = 2$ with the lighter HNL N_1 having a mass $m_{\mathrm{N1}} = 150\,\mathrm{GeV}$ (Figs. 3.1a and 3.1b) and $m_{\mathrm{N1}} = 1500\,\mathrm{GeV}$ (Figs. 3.1c and 3.1d) as a function of WW centre of mass energy $\sqrt{M^2_{\mathrm{ww}}}$. The individual cases N_I are polarised single HNL cross sections with parameters corresponding to their values in the qDl pair. The combined case is the polarised cross section of this same qDl pair.

We see that in the transversally polarised case (Figs. 3.1a and 3.1c), the individual HNL contributions drop with increasing $\sqrt{M^2_{\mathrm{ww}}}$. Furthermore, the mass ratio causes a split between the cross sections for all centre of mass energies. This split is more significant when the HNL masses are comparable to $\sqrt{M^2_{\mathrm{ww}}}$ and approaches a constant factor (~ 1 order of magnitude difference for $r_{\mathrm{N}} = 2$) between the individual contributions, as $\sqrt{M^2_{\mathrm{ww}}}$ becomes large compared to the HNL masses. As the combined qDl cross section is generated by negative interference between the two mass states — and the N_2 contribution is suppressed by the mixing angle as prescribed by Eq. (1.23) — the N_1 curve always lies above the combined case. For hierarchical HNLs, this suppression is strong enough for the combined cross section to be larger than the N_2 contribution (see also Figs. E.7e and E.7g for $r_{\mathrm{N}} = 10$, where the combined cross sections is in good approximation equal to that of the lighter single HNL). This is not the case for degenerate HNLs (see Figs. E.7a and E.7c for $r_{\mathrm{N}} = 1.1$), where the negative interference is much stronger due to comparable individual contributions.

In the longitudinal case (Figs. 3.1b and 3.1d), the individual HNL contributions grow with increasing $\sqrt{M^2_{\mathrm{ww}}}$. Contrary to the transversal case, there is a constant factor between individual contributions when the centre of mass energy is small or of comparable size to the HNL masses. This split vanishes when $\sqrt{M^2_{\mathrm{ww}}}$ becomes large compared to $m_{\mathrm{N}I}$. As the N_2 contribution approaches that of N_1, the negative interference between the two causes the combined cross section to drop. This behaviour is reproduced both in the more degenerate ($r_{\mathrm{N}} = 1.1$, Figs. E.7b and E.7d) and more

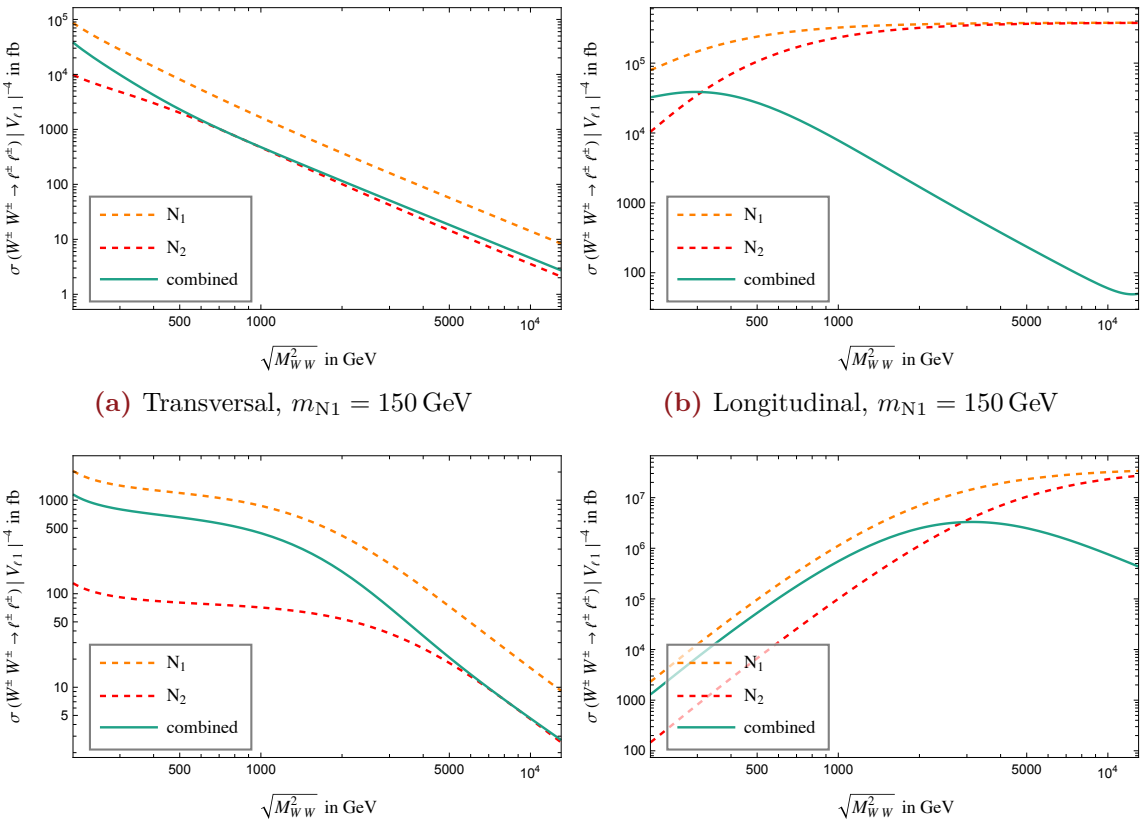

(a) Transversal, $m_{\mathrm{N1}} = 150\,\mathrm{GeV}$ **(b)** Longitudinal, $m_{\mathrm{N1}} = 150\,\mathrm{GeV}$

(c) Transversal, $m_{\mathrm{N1}} = 1500\,\mathrm{GeV}$ **(d)** Longitudinal, $m_{\mathrm{N1}} = 1500\,\mathrm{GeV}$

Figure 3.1: Polarised cross sections of $W^\pm W^\pm \to \ell^\pm \ell^\pm$ scattering as decompositions in the WW polarisations as Transversal $\leftrightarrow \sigma^{\mathrm{TT}}$ and Longitudinal $\leftrightarrow \sigma^{\mathrm{LL}}$. The cross sections are given as a function of the centre of mass energy $\sqrt{M^2_{\mathrm{WW}}}$. The data is given for the lighter HNL mass $m_{\mathrm{N1}} = 150\,\mathrm{GeV}$ (upper) and $m_{\mathrm{N1}} = 1500\,\mathrm{GeV}$ (lower) with the second HNL having a mass according to the mass ratio $r_{\mathrm{N}} = 2$. For different values of r_{N} see Fig. E.7.

hierarchical case ($r_{\mathrm{N}} = 10$, Figs. E.7f and E.7h). Here, the splitting is also smaller in the degenerate and larger in the hierarchical case, due to the same reasoning as in the transversal case.

We note that at small WW centre of mass energies, the transversal and longitudinal contributions are comparable, while at large $\sqrt{M^2_{\mathrm{WW}}}$ the longitudinal contributions dominate.

Validity of the Effective W Approximation

In the deduction of the effective W approximation's PDFs, one formally assumes decoherence between the polarisation states of individual W "partons" (see Section 1.4.1). This means that if contributions due to different polarisation states are on a similar scale — and thus the decoherence assumption is no longer valid — the results at pp level potentially underestimate by a factor of few[2].[3]

To investigate the validity of the approximation we will thus compare the doubly longitudinally polarised (LL) WW cross section to the doubly transversally polarised (TT) case. As the folding with PDFs involves an integration over different energy regimes, this is important at all relevant centre of mass energies determined by the PDFs in Fig. 1.5. Figure 3.2 shows this for a centre of mass energy on the lower end of the PDF spectrum ($M^2_{\mathrm{WW}} = 16m^2_W$, Figs. 3.2a and 3.2b), on the upper end of LHC energies ($M^2_{\mathrm{WW}} = s_{\mathrm{LHC}}/100$, Figs. 3.2c and 3.2d), and upper end of FCC energies ($M^2_{\mathrm{WW}} = s_{\mathrm{FCC}}/100$, Figs. 3.2e and 3.2f). We note that for low end energies, the LL cross section becomes comparable with the TT cross section for $m_{\mathrm{N1}} \gtrsim 100$–$200\,\mathrm{GeV}$, while at larger energies this is the case for $m_{\mathrm{N1}} \gtrsim 10$–$100\,\mathrm{GeV}$. As pp level validity is determined by validity at all relevant sub energies, only a region of general LL dominance fully meets the assumptions of the effective W approximation. Hence, we expect the results to become more accurate for larger HNL masses, while we expect to underestimate the pp level cross section for smaller m_{N1}. Validity due to this restriction is expected to be reached for $m_{\mathrm{N1}} \gtrsim$ several $100\,\mathrm{GeV}$.

It has been, furthermore, pointed out in past literature that in order to achieve numerical stability, the lower limit of the integration has to be set above a certain threshold, rather than to account for minimal production energy [130]. We investigate this by varying the lower limit on τ_{min} (see Eq. (3.2)). This is shown in Fig. 3.3, where we have plotted the cross section of a single isolated HNL for different values of $M^{\mathrm{min}}_{WW} = \sqrt{M^{\mathrm{min}\,2}_{WW}}$ at $\sqrt{s_{\mathrm{LHC}}} = 13\,\mathrm{TeV}$. For small HNL masses $m_{\mathrm{N}} \lesssim 100\,\mathrm{GeV}$, there is a noticeable dependence on the lower cut-off. We note that the cross section for $M^{\mathrm{min}}_{WW} = 320$–$500\,\mathrm{GeV}$ is largest in this regime, even though we removed part of the integration interval for positive definite functions with respect to e.g. $M^{\mathrm{min}}_{WW} = 200\,\mathrm{GeV}$. The lines of $M^{\mathrm{min}}_{WW} = 320\,\mathrm{GeV}$ and $M^{\mathrm{min}}_{WW} = 500\,\mathrm{GeV}$ coincide for all mass values m_{N_1}. For $m_{\mathrm{N}} \gtrsim$ several $100\,\mathrm{GeV}$, the numerical values are identical for all $M^{\mathrm{min}}_{WW} < 750\,\mathrm{GeV}$, while the curve of $M^{\mathrm{min}}_{WW} = 750\,\mathrm{GeV}$ lies slightly below the others. The curve representing $M^{\mathrm{min}}_{WW} = 1\,\mathrm{TeV}$ lies below the others by a factor of $\mathcal{O}(10\,\%)$ for lower m_{N} converging with the rest at $m_{\mathrm{N}} \simeq$ few TeV.

[3] This is due to the error occurring in both p involved in the $pp \to \ell^\pm\ell^\pm jj$ process.

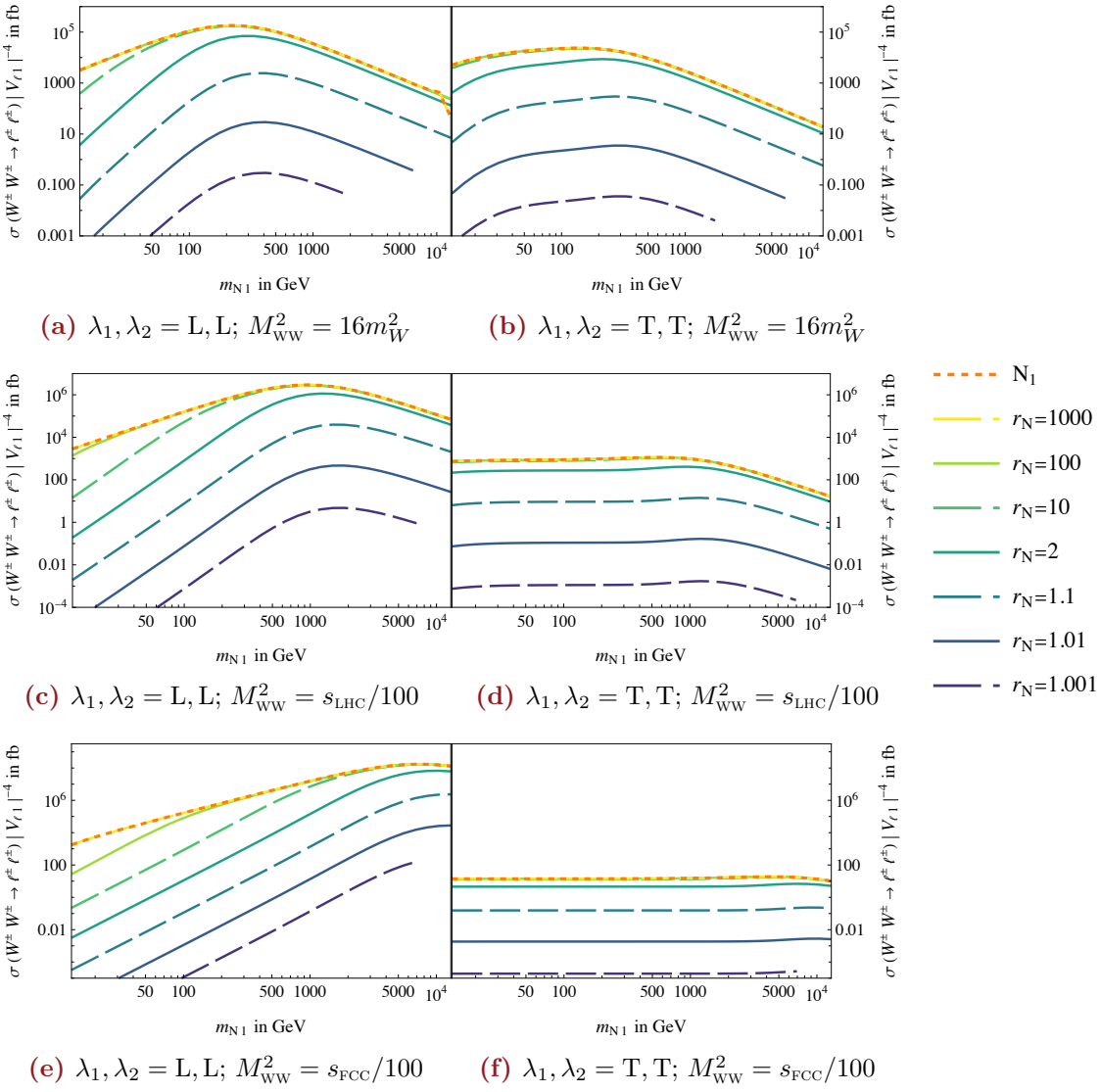

(a) $\lambda_1, \lambda_2 = \mathrm{L}, \mathrm{L}$; $M^2_{\mathrm{WW}} = 16 m_W^2$ **(b)** $\lambda_1, \lambda_2 = \mathrm{T}, \mathrm{T}$; $M^2_{\mathrm{WW}} = 16 m_W^2$

(c) $\lambda_1, \lambda_2 = \mathrm{L}, \mathrm{L}$; $M^2_{\mathrm{WW}} = s_{\mathrm{LHC}}/100$ **(d)** $\lambda_1, \lambda_2 = \mathrm{T}, \mathrm{T}$; $M^2_{\mathrm{WW}} = s_{\mathrm{LHC}}/100$

(e) $\lambda_1, \lambda_2 = \mathrm{L}, \mathrm{L}$; $M^2_{\mathrm{WW}} = s_{\mathrm{FCC}}/100$ **(f)** $\lambda_1, \lambda_2 = \mathrm{T}, \mathrm{T}$; $M^2_{\mathrm{WW}} = s_{\mathrm{FCC}}/100$

Figure 3.2: Polarised cross sections of $W^\pm W^\pm \to \ell^\pm \ell^\pm$. The polarisation λ_1, λ_2 are both longitudinal (L, L, left panels) or transversal (T, T, right panels), while the centre of mass energy is $4m_W = 225\,\mathrm{GeV}$ (top panels), $\sqrt{s_{\mathrm{FCC}}}/10 = 1.3\,\mathrm{TeV}$ (middle panels) and $\sqrt{s_{\mathrm{FCC}}}/10 = 10\,\mathrm{TeV}$ (bottom panels). We assume a QDL model with mass ratio r_N.

Overall the effect of the cut-off is only significant in the regime of $m_N \lesssim 100\,\mathrm{GeV}$. As the focus of this work lies on the regime of $m_N \simeq$ several 100–few 1000 GeV, the influence is marginal. Nevertheless, we set the lower limit $M^{\mathrm{min}}_{WW} = 4m_W \simeq 320\,\mathrm{GeV}$ as a benchmark for this work, which corresponds to twice the minimal production energy and is already in a numerically stable regime according to Fig. 3.3.

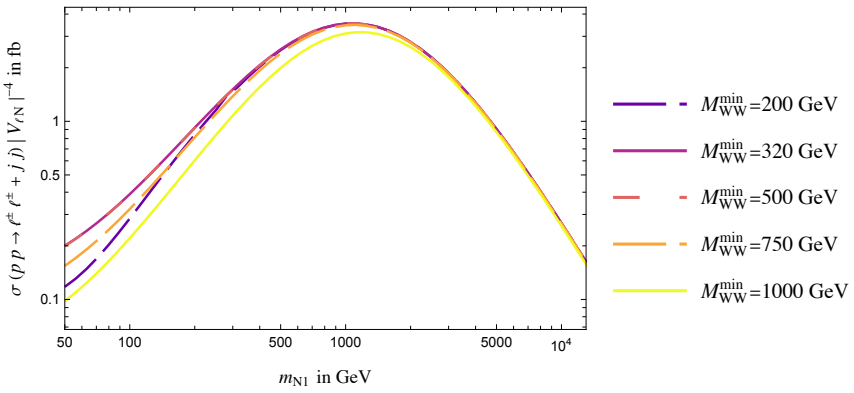

Figure 3.3: Single isolated HNL pp level WBF cross section at $\sqrt{s_{\text{LHC}}} = 13\,\text{TeV}$ as a function of HNL mass m_{N}. This is shown for different lower bounds on the integration parameters of the effective W approximation determined by M_{WW} (according to $\tau^{\text{min}} = M_{\text{WW}}^{\text{min}\,2} s_{pp}^{-1}$).

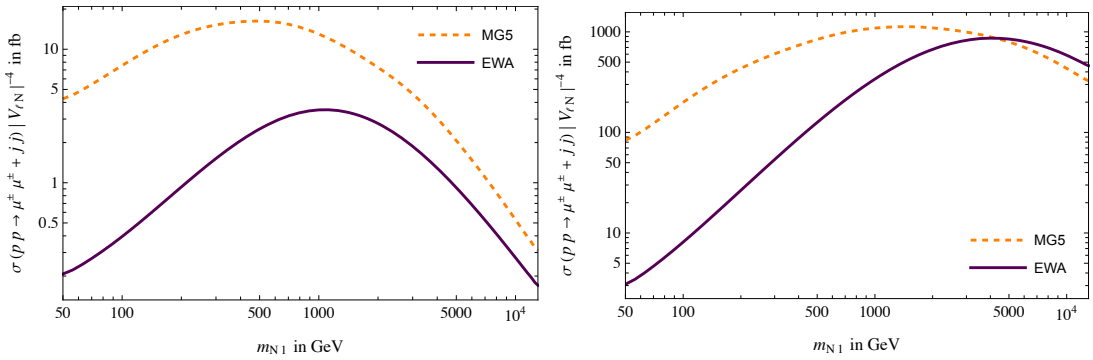

(a) $\sqrt{s_{\text{LHC}}} = 13\,\text{TeV}$ **(b)** $\sqrt{s_{\text{FCC}}} = 100\,\text{TeV}$

Figure 3.4: WBF at pp level cross section for a single isolated HNL ($W^\pm W^\pm$ combined). Comparison of MG5aMC detector simulation prescribed by Fuks et al. [101] (dashed orange) and effective W approximation (purple), shown at LHC (a) and FCC (b) centre of mass energy.

3.1.2 Rescaling for Small Heavy Neutral Lepton Masses

For the case of a single HNL in a phenomenological type-I seesaw, Fig. 3.4 compares the WBF cross section deduced using the EWA without any detector motivated cuts with that including such cuts on the jets using the Montecarlo event generator MG5aMC.

As prescribed by Fuks et al., we employ generator level cuts for the LHC on the jets' transverse momentum p_T^j and pseudorapidities η^j

$$p_T^j > 20\,\text{GeV} \quad \text{and} \quad |\eta^j| < 5.5. \tag{3.4}$$

As the FCC is expected to have a larger pseudorapidity acceptance [131], we adjust the cuts to

$$p_T^j > 20\,\text{GeV} \quad \text{and} \quad |\eta^j| < 6. \tag{3.5}$$

In both cases we impose the restriction on QCD partons to be sequentially clustered according to the anti-k_T algorithm [132] with $R = 0.4$, and the standard Delphes ATLAS parameter card [133] for all other values. The MG5aMC simulations were performed only at LO in QCD, due to unknown errors occurring in the NLO simulation and time restriction on this thesis.

For LHC centre of mass energy (see Fig. 3.4a), we see that in the EWA applicability regime according to Section 3.1.1, the two curves differ by a factor of ~ 1.8, while the difference is significant at smaller m_N (~ 20). This discrepancy could be due to neglecting terms scaling as $\mathcal{O}\left(p_T^2 M_{WW}^{-2}\right), \mathcal{O}\left(m_W^2 M_{WW}^{-2}\right)$, as the EWA is formulated as a small angle approximation (see Section 1.4). These are known shortcomings of the EWA [130] usually resulting in errors up to order 1.

For FCC centre of mass energy (see Fig. 3.4b), we see a similar behaviour to the LHC case. In the low mass regime of $m_{\text{N}1} < 1\,\text{TeV}$ we find a large discrepancy ~ 20, which vanishes in the large mass regime. Here, we find that the EWA slightly overestimates the detector cross section. This is because — as larger centre of mass energy leads to larger pseudorapidities — even the FCC adjusted cuts likely decrease the overall cross section more significantly than in the LHC case. Meanwhile in the EWA, we do not consider any cuts on the signal, leading to a slight overestimation. As the terms mentioned in the paragraph above scale with M_{WW}^{-2}, we expect the EWA to be more accurate in this regard for the FCC case.

By comparing the two curves, we can generate a rescaling function for our pp level cross sections derived in the EWA for a given centre of mass energy. This approach allows us to investigate the effect of complex mixing angles — as demanded by Eq. (1.23), and which is not yet possible in MG5aMC — for an extended range of HNL masses $m_{\text{N}1}$, while respecting detector geometries as given by Eqs. (3.4) and (3.5). We expect this scaling to be directly translatable to all r_N showing the same WW level differential cross section. According to Eq. (2.16) this is the case for all r_N if $m_{\text{N}1} > 2m_W = 160\,\text{GeV}$.

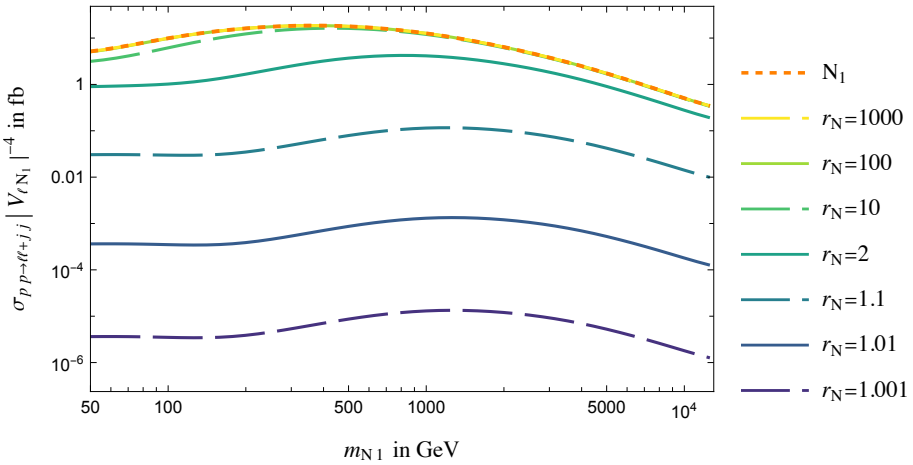

Figure 3.5: Cross section of $pp \to \ell^\pm\ell^\pm jj$ as calculated in the effective W approximation in the model with two HNLs whose mass ratio is equal to r_N. The mass of the lighter HNL is shown as the x-axis, while another one is r_N times heavier. Notations are the same as in Fig. 2.5. The dependence on the mixing angle $|V_{\ell 1}|^4$ is factored out. Contribution of the light neutrinos is neglected (see Section 2.3 for details). The centre of mass energy is assumed to be $\sqrt{s_{\text{LHC}}} = 13\,\text{TeV}$.

3.2 Large Hadron Collider

3.2.1 *pp* Level Cross Section

Figure 3.5 shows the expected total cross section of $pp \to \ell^+\ell^+ + jj$ for a centre of mass energy $\sqrt{s_{\text{LHC}}} = 13\,\text{TeV}$. We see that the polarisation decomposition, folding with PDFs, and subsequent rescaling increases the difference in relative maximum with respect to the mass ratio r_N. The highly hierarchical case approaches that of the independent single HNL at $m_{N1} \sim 450\,\text{GeV}$, while for the degenerate case the maximum shifts from around $m_{N1} \sim 600\,\text{TeV}$ at WW level to $m_{N1} \sim 1\,\text{TeV}$. Importantly, the pp cross section is about four orders of magnitude smaller than the WW cross section at $M_{WW} = 490\,\text{GeV}$. Beyond this, the general characteristics of the WW-scattering case directly translate into the pp case.

3.2.2 Theoretically Accessible Mass Ranges

Using the pp cross sections in Fig. 3.5, we can estimate how many events could be expected at the LHC. To this end, we multiply the cross section by the maximal

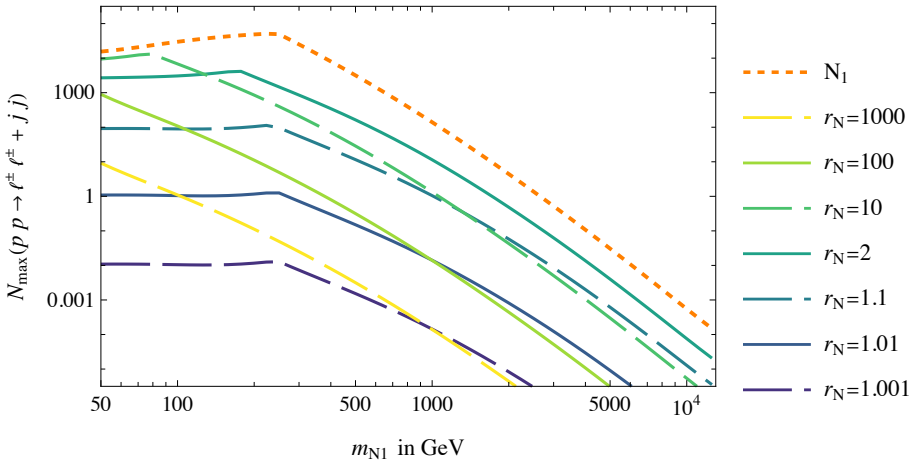

Figure 3.6: The maximal number of WBF events as calculated in the effective W approximation in the model with two HNLs with mass ratio $r_{\rm N}$. The mixing angle $|V_{\ell I}|^4$ is maximised, according to Eq. (3.6). Notice that for $m_{\rm N2} = r_{\rm N} m_{\rm N1} > v$, it is the condition on the mixing angle $|V_{\ell 2}|$ that dominates. Efficiency of the detector is assumed 100%. The centre of mass energy is $\sqrt{s_{\rm LHC}} = 13\,\text{TeV}$ and the luminosity $3\,\text{ab}^{-1}$.

theoretically admissible values of the mixing angles $|V_{\ell I}|$ (see Eq. (3.6) for details). This means that both $V_{\ell 1}$ and $V_{\ell 2}$ should obey the condition

$$\left|V_{\ell I}\right| \leq \begin{cases} 1, & m_{{\rm N}I} < v \\ \dfrac{v}{m_{{\rm N}I}}, & m_{{\rm N}I} > v \end{cases} \tag{3.6}$$

for their respective masses.[4] Here, v is the Higgs' vacuum expectation value. Notice that for $m_{\rm N2} > v$ and $r_{\rm N} > 1$, the perturbativity condition of the HNL $\rm N_2$ provides the most stringent theoretical upper bound on $|V_{\ell 1}|$ (under the assumption of Eq. (1.23)).[5]

Figure 3.6 shows the expected maximal amount of events $N_{\max}$ at the HL-LHC with an integrated luminosity of $3000\,\text{fb}^{-1} \equiv 3\,\text{ab}^{-1}$ [134] as a function of the lighter of two HNL masses $m_{\rm N1}$ for different mass ratios $r_{\rm N}$, as well as for a single HNL case (dashed orange). The number of events reaches its maximum at $m_{\rm N1} \sim r_{\rm N}^{-1/2}\text{VEV}$. For models with $m_{\rm N1} < 100\,\text{GeV}$, $N_{\max}$ is the largest for $r_{\rm N} \gtrsim \mathcal{O}(10)$, while for $m_{\rm N1} > 100\,\text{GeV}$, $N_{\max}$ is largest for $r_{\rm N} \sim$ few. Notice that for $r_N \geq 2$ — and for

[4] Strictly speaking, the actual perturbativity limit is of course $\ll 1$. However, setting a limit of exactly 1 arguably removes a degree of arbitrariness.

[5] This, in particular, demonstrates that decoupling of one of the HNLs, while keeping neutrino masses small, is not possible. The condition for the theory to remain perturbative imposes constraints on the mixings of non-decoupled lighter HNLs.

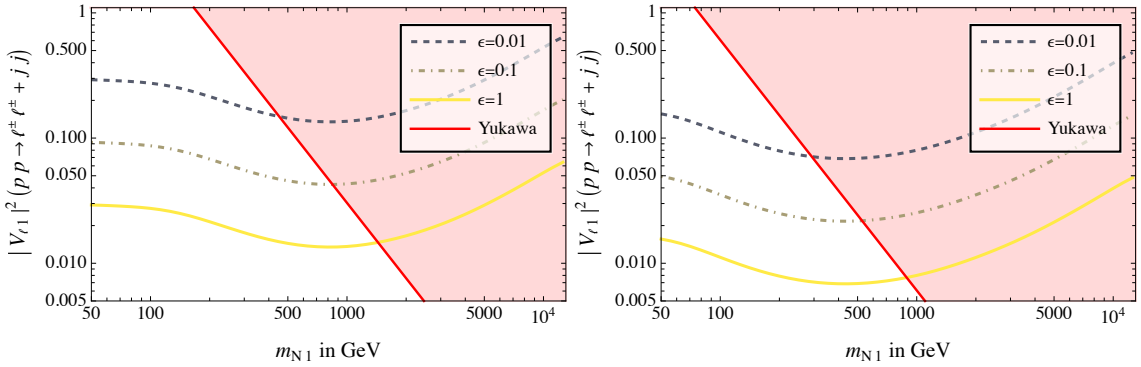

(a) $r_{\mathrm{N}} = 2$ **(b)** $r_{\mathrm{N}} = 10$

Figure 3.7: *Optimistic* exclusion limits on the N_1 parameters via WBF-mediated $pp \to \ell^\pm\ell^\pm jj$ events in the model with two HNLs with mass ratio r_{N}. The exclusions limits are 95 % CL assuming zero background. The centre of mass energy is $\sqrt{s_{\mathrm{LHC}}} = 13\,\mathrm{TeV}$ and the luminosity $3\,\mathrm{ab}^{-1}$.

masses $m_{\mathrm{N}1} \gtrsim$ few 100 GeV in general — the differential cross section predicted for a QDL HNL pair looks similar to that of the free parameter single HNL. Therefore, efficiencies of cuts will be similar to those estimated in [101]. We stress that, for all mass ratios $m_{\mathrm{N}1} \geq 2\,\mathrm{TeV}$, $N_{\mathrm{max}} < 1$. As the actual perturbativity limit would be smaller than $F = 1$, this means that the process $pp \to \ell^\pm\ell^\pm jj$ is not suitable for probing HNLs in the TeV mass range at the LHC.

3.2.3 Mixing-Mass Exclusion Regions

Nevertheless, using the cross sections shown in Fig. 3.5, we can give an estimate 95 % CL exclusion in the $(V_{\ell\mathrm{N}}, r_{\mathrm{N}}, m_{\mathrm{N}})$ parameter space. We present our results for $r_{\mathrm{N}} = 2$ and $r_{\mathrm{N}} = 10$, as they represent the most promising mass ratio regime of $\mathcal{O}$ (few–several) according to Fig. 3.6. Bounds for $r_{\mathrm{N}} < 2$ become an order of magnitude weaker for every order of magnitude in $|r_{\mathrm{N}} - 1| \to 0$. For $r_{\mathrm{N}} > 10$ the bounds remain the same, while the Yukawa excluded region grows. This can be observed in Fig. E.8 where we compare exclusion regions for $r_{\mathrm{N}} \in \{1.1, 2, 10, 100\}$. The mass ratios $r_{\mathrm{N}} = 2$ and $r_{\mathrm{N}} = 10$ are chosen, as only in this r_{N} range any signal could be expected in the $m_{\mathrm{N}1} \sim$ TeV range interesting for indirect searches.

In a model with $r_{\mathrm{N}} \sim$ few (Fig. 3.7a), for a near perfect detector and negligible background ($\epsilon \sim 1$, yellow), we find that a WBF search at the HL-LHC can probe HNL masses $m_{\mathrm{N}1}$ up to 1.5 TeV. This mass range is limited to $m_{\mathrm{N}1} \lesssim 850\,\mathrm{GeV}$ for

a lower detector efficiency ($\epsilon \sim 0.1$, dashed-dotted grey), and $m_{\mathrm{N1}} \lesssim 450\,\mathrm{GeV}$ for a low efficiency ($\epsilon \sim 0.01$, dashed blue).

In a model with $r_{\mathrm{N}} \sim \mathcal{O}(10)$ (Fig. 3.7b) the cross section per $|V_{\ell 1}|^4$ is higher, but the range of accessible masses is smaller due to the perturbativity condition of Eq. (3.6). As a result the maximally probed HNL mass is $m_{\mathrm{N1}} \lesssim 850\,\mathrm{GeV}$. This limit drops to $m_{\mathrm{N1}} \lesssim$ several $100\,\mathrm{GeV}$ for more realistic efficiencies.[6]

3.3 Future Circular Collider

Sensitivity of the WBF process is maximal for $\sqrt{M^2_{\mathrm{WW}}} \sim m_{\mathrm{N1}}$. With larger centre of mass energy of pp collisions, this factor increases accordingly. Therefore, the process under consideration can be expected to be more efficient at Future Circular Collider (FCC-hh), where the anticipated collision centre of mass energy $\sqrt{s_{\mathrm{FCC}}} = 100\,\mathrm{TeV}$ [135]. To the authors best knowledge, a WBF investigation with FCC-hh parameters has not yet been performed in past literature.

3.3.1 *pp* Level Cross Section

Using the projected centre of mass energy and machinery developed in this work, we can estimate the WBF cross section of the $pp \to \ell^\pm \ell^\pm jj$ process, shown in Fig. 3.8. We find that the cross section reaches its maximum at $m_{\mathrm{N1}} \simeq 1.5\,\mathrm{TeV}$ for a highly hierarchical qDl pair and at up to $m_{\mathrm{N1}} \simeq 5\,\mathrm{TeV}$ in the highly degenerate case. It is, furthermore, about two orders of magnitude larger at FCC compared to LHC energies and reaches $\sim 1\,\mathrm{pb}$ for a hierarchical HNL pair.

3.3.2 Theoretically Accessible Mass Ranges

With a target integrated luminosity $30\,\mathrm{ab}^{-1}$[131], this corresponds to a maximal theoretically admissible event number N_{max} as shown in Fig. 3.9. Again, we see that for $m_{\mathrm{N1}} > r_{\mathrm{N}}^{-1/2}$vev Yukawa perturbativity becomes the main theoretical constraint on the mixing angle $V_{\ell 1}$, resulting in $r_{\mathrm{N}} \sim$ few to yield the largest N_{max}. Nevertheless, at FCC parameters, the mass range for m_{N1} in a qDl pair with $1.01 < r_{\mathrm{N}} < 100$ extends into the TeV range.

[6] Fuks et al. report a maximal efficiency of around 40 % for $m_{\mathrm{N}} \sim \mathcal{O}\,(\mathrm{TeV})$ for the free parameter single HNL case, which drops for smaller masses.

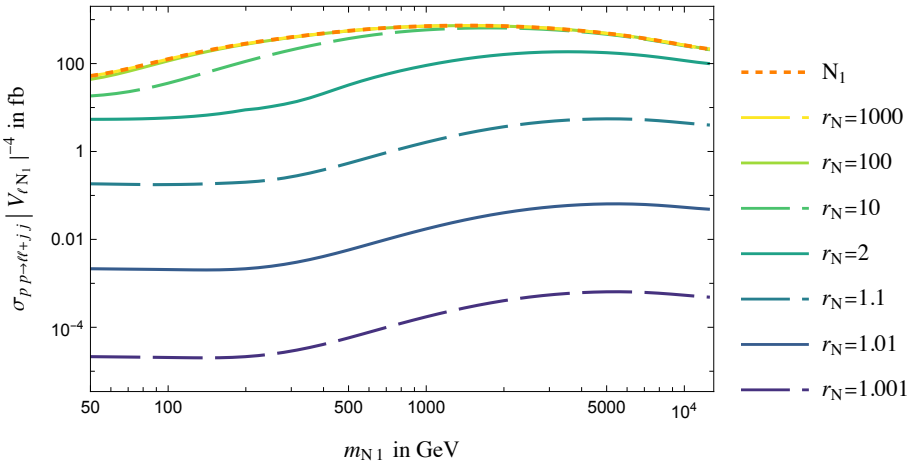

Figure 3.8: Cross section of $pp \to \ell^\pm\ell^\pm jj$ as calculated in the effective W approximation in the model with two HNLs whose mass ratio is equal to r_N. The mass of the lighter HNL is shown as the x-axis, while another one is r_N times heavier. Notations are the same as in Fig. 2.5. The dependence on the mixing angle $|V_{\ell 1}|^4$ is factored out. Contribution of the light neutrinos is neglected (see Section 2.3 for details). The centre of mass energy is assumed to be $\sqrt{s_{\text{FCC}}} = 100\,\text{TeV}$.

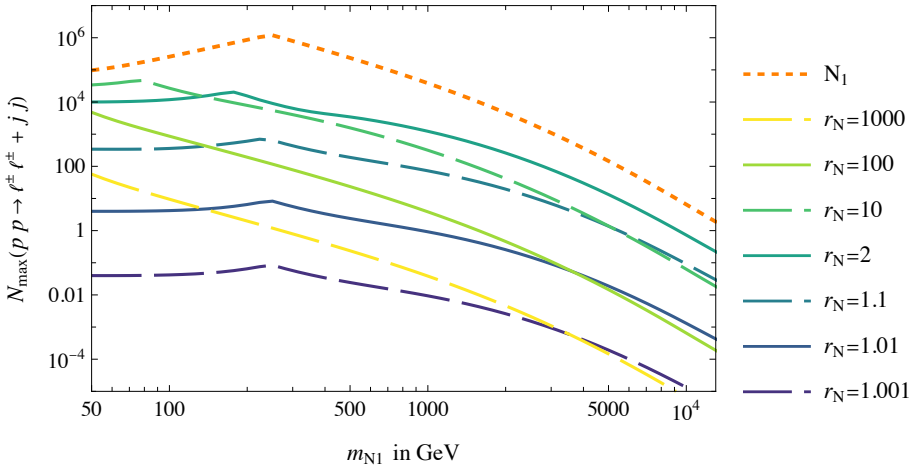

Figure 3.9: The maximal number of WBF events as calculated in the effective W approximation in the model with two HNLs with mass ratio r_N. The mixing angle $|V_{\ell 1}|^4$ is maximised, according to Eq. (3.6). Efficiency of the detector is assumed 100 %. The centre of mass energy is $\sqrt{s_{\text{FCC}}} = 100\,\text{TeV}$ and the luminosity $30\,\text{ab}^{-1}$.

3.3.3 Mixing-Mass Exclusion Regions

Due to the significantly larger cross section and higher integrated luminosity, the relevant $(V_{\ell N}, r_N, m_N)$ parameter space covered by $pp \to \ell^\pm\ell^\pm jj$ at the FCC-hh opens

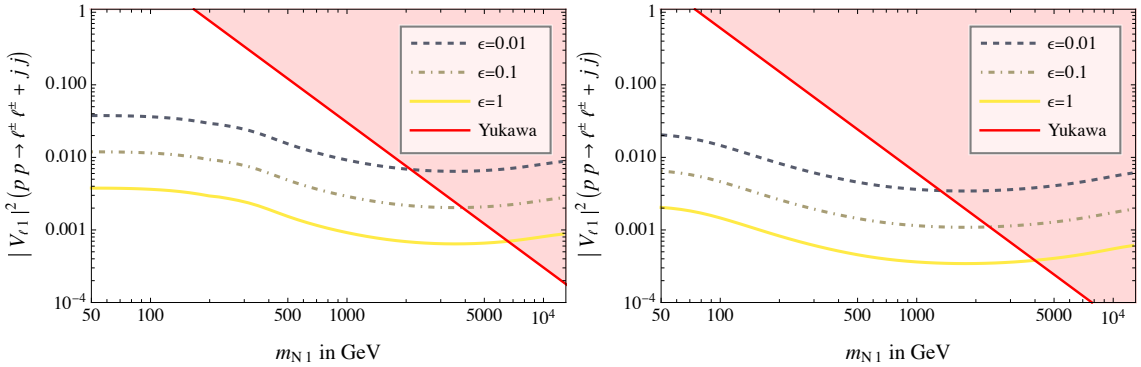

(a) $r_{\mathrm{N}} = 2$ **(b)** $r_{\mathrm{N}} = 10$

Figure 3.10: The exclusion limits on the N_1 parameters by WBF events as calculated in the effective W approximation in the model with two HNLs with mass ratio r_{N}. The limits are obtained for 95 % CL exclusions assuming zero background. The assumed detector efficiency is ϵ, the centre of mass energy $\sqrt{s_{\mathrm{FCC}}} = 100\,\mathrm{TeV}$ and the luminosity $30\,\mathrm{ab}^{-1}$.

up as seen in the previous section. For both $r_{\mathrm{N}} = 2$ and $r_{\mathrm{N}} = 10$ (see Figs. 3.10a and 3.10b respectively), physically relevant mixing angles $V_{\ell\mathrm{N}}$ are within reach for a QDL HNL pair with $m_{\mathrm{N1}} \sim$ few TeV and $m_{\mathrm{N1}} \sim$ few TeV assuming a detection efficiency $\epsilon \geq 0.1$. See Fig. E.8 for exclusion plots for further values of r_{N}, where we find that for $r_{\mathrm{N}} = 1.1$ and $r_{\mathrm{N}} = 100$ the detection of a QDL pair with m_{N1} in the TeV range is only possible for a highly efficient detector. The relative difference between different values of r_{N} are as discussed in the LHC case in Section 3.2.

Discussion and Conclusion 4

4.1 Discussion

4.1.1 *WW* Level Results

The results derived at WW level are fully analytical. Therefore, the numerical values and expansions presented in Chapter 2 are effectual barring the following caveats.

As mentioned in Section 2.1, the chosen light neutrino mass scale in case of the single HNL model corresponds to an experimental upper bound. As the actual light neutrino mass scale can be anywhere between the $\sqrt{\Delta m^2_{\text{atm}}}$ and this upper bound (see Section 1.1.2), the numerical values presented for this model are *very* optimistic.

As mentioned in Section 2.3, the exact results in the Casas-Ibarra parametrisation Eq. (2.21) are strictly only valid for $W^\pm W^\pm \to e^\pm e^\pm$ scattering for a normal neutrino mass hierarchy, as they rely on direct input of the PMNS matrix entries and light neutrino masses. However, this matters only if the light mass states contribute significantly to the cross section. For mixing angles with significant $\operatorname{Im}\omega$ enhancement (where this is not the case), the same cross sections can be recovered in other scenarios by adjusting $\operatorname{Im}\omega$ to the corresponding $U^2_{\ell i} m_i$ ratios (c.f. Appendix B).

4.1.2 *pp* Level Results

In the deduction of pp level results we employed the effective W approximation (see Sections 1.4 and 3.1.1 for details). As we saw in Section 3.1.1, we expected the EWA results to be less reliable for $m_{\text{N1}} \lesssim$ few 100 GeV. This was confirmed by the direct comparison of EWA results with a full $2 \to 4$ simulation for a phenomenological type-I seesaw HNL in Fig. 3.4. The consequent rescaling remedies this mismatch for QDL pairs with large mass ratios r_{N}, as the WW level differential cross sections — and consequently the WW system behaviour in the $2 \to 4$ process — are very similar (see Fig. E.4). In the case of near degeneracy with masses $m_{\text{N1}} <$ few 100 GeV this is not the case. Here we expect that deviations in this regime should be expected when considering a full Montecarlo simulation. However, as this parameter combination will unlikely lead to WBF detector discovery even at FCC energies (see Fig. E.8e), giving only a rough estimate for that parameter space is justified.

The rescaling cross sections in this thesis were derived at LO in QCD due to unknown errors occurring in the NLO simulations and time restrictions. At the LHC the k factor $k = \sigma_{\mathrm{NLO}}\sigma_{\mathrm{LO}}^{-1}$ lies in the range 1–1.4. Due to higher energies at the FCC we expect the influence of NLO QCD to be even stronger. Therefore, our cross section and subsequent bounds on HNL parameters likely underestimate the actual detector signal strength.

On the other hand, all pp level results in this thesis were derived without considering background motivated detector cuts, so that no cuts were applied on the signal outside of the bounds on the jets. Fuks et al. report a relatively stable 40 % efficiency for a phenomenological type-I seesaw HNL with $m_{\mathrm{N1}} \sim$ few TeV. However, due to the higher centre of mass energy — and associated forward shift in signal — these efficiencies are not easily translated to the FCC. This leads to an overestimation of the signal strength.

At the LHC, these two effects nearly compensate one another in the mass range of interest ($m_{\mathrm{N1}} \simeq 1\,\mathrm{TeV}$), however without a full detector level study, it is not possible to predict how this translates to FCC energies. Therefore, we will limit ourselves to giving an estimate on the potential reach on the HNL parameters of the process for a given centre of mass energy, rather than actual exclusion limits by a potential detector experiment.

4.2 Conclusion

In this work we analysed the collider probe for Majorana particles with masses ranging from $\sim 50\,\mathrm{GeV}$ to $\sim 5\,\mathrm{TeV}$. The process that we considered is a direct analog of the $0\nu\beta\beta$ decay — $pp \to \ell^{\pm}\ell^{\pm}jj$ (Section 1.3.2). Compared to previous works on the subject (c.f. [97–101]) we concentrated on models where HNLs are solely responsible for generating neutrino masses. All Majorana particles — HNLs and active neutrinos — contribute to the process in question and we analysed their interference. We demonstrated that such an interference is necessarily *destructive* as a consequence of smallness of neutrino masses compared to other relevant energy scales. There are two regimes determined by whether HNLs' mixing angles $|V_{\ell\mathrm{N}}|$ are comparable or much larger than the naive "seesaw limit" $|V|^2_{\mathrm{seesaw}} = m_\nu m_{\mathrm{N}}^{-1}$ (see text around Eq. (1.21)).

1. For $|V_{\ell\mathrm{N}}| \sim |V|_{\mathrm{seesaw}}$ and HNL masses comparable to the sub process energy scale, cancellation between light states and heavy mass states occurs. For heavy HNL masses (above the sub process energy scale) the HNL contribution

can become suppressed with respect to that of the light neutrino states. In both cases the cross section is limited by its proportionality to $m_{\nu_i}^2$.

2. For $|V_{\ell\mathrm{N}}| \gg |V|_{\mathrm{seesaw}}$ (while still keeping neutrino masses small, as experimentally observed) the situation is quite different. The contribution of active neutrinos is negligible, but cancellation occurs between HNL states (similarly to the way it happens in the neutrino mass matrix). On one hand, the cross section is always smaller than that of an isolated single HNL with the same mixing. On the other hand, the cross section can become enhanced compared to the naive scaling of $\sigma \propto m_\nu^2$ which would be suggested by the Weinberg operator per se (c.f. [136]). This enhancement corresponds roughly to a factor of $|V_{\ell\mathrm{N}}|^4 |V|_{\mathrm{seesaw}}^{-4}$ and occurs only if HNLs are sufficiently far from the quasi-Dirac limit and was found to be most effective for $m_{\mathrm{N}_2} m_{\mathrm{N}_1}^{-1} = r_{\mathrm{N}} \gtrsim$ few.
3. Lastly, large mass splitting $r_{\mathrm{N}} \gg 1$ allows to recovering the limit of a single HNL (as considered, e.g. in [101]) only with considerable limitations. Naively, in this case the heavier HNL N_2 and its contribution to $pp \to \ell^\pm \ell^\pm jj$ disappears. This is not necessarily the case in our realistic (and UV-complete) model (type-I seesaw with 2 HNLs), as perturbativity demands that all Yukawa couplings are smaller than 1. For HNLs heavier than the Higgs' vacuum expectation value, this condition together with the requirement of the neutrino mass smallness caps not only the value of the mixing angle $|V_{\ell 2}|$ but by extension also $|V_{\ell 1}|$.

As a result, the largest sensitivity occurs in models with $r_{\mathrm{N}} \sim$ few at $m_{\mathrm{N}_1} \sim$ 0.5–1 TeV.[1] Even in this case, the cross section for the process $pp \to \ell^\pm \ell^\pm jj$ is about 1 order of magnitude smaller than that of a single HNL with the same mixing angle. Figure 4.1 compares the single event sensitivity for these parameters to other searches for the case of $V_{\mu 1}$ mixing. The solid thick lines correspond to a mass ratio $r_{\mathrm{N}} = 2$, and the dashed thick lines to $r_{\mathrm{N}} = 10$. We present this for $V_{\mu 1}$ mixing, as the $\mu^\pm \mu^\pm$ final state involves a smaller implicit background than $e^\pm e^\pm$ [101], and unlike $\tau^\pm \tau^\pm$ does not require decay reconstruction.

At the HL-LHC, the best exclusion limit obtainable for such mass ratios reaches $|V_{\ell 1}|^2 \sim 0.01$–0.03 (assuming a background-free search, 100 % detector efficiency and a luminosity of $3\,\mathrm{ab}^{-1}$). These limits are not competitive with those coming from the *electroweak precision tests* (EWPT) [137] or from non-observations of charged lepton *flavour violating* (cLFV) processes involving charged leptons [138] coming from non-observation of $\mu \to 3e$ decays or $\mu - e$ conversions under the assumption

[1] Contributions of hierarchical HNLs to the $0\nu\beta\beta$ process have been studied recently [83–85].

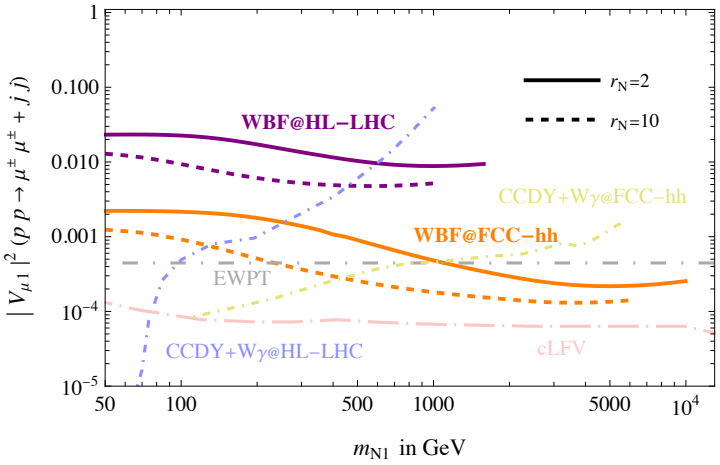

Figure 4.1: Single event sensitivity to the HNL mixing parameter $V_{\mu 1}$ from W boson fusion in $pp \to \ell^\pm \ell^\pm jj$ at future collider experiments for an HNL pair with selected mass ratios r_{N} for an assumed detector efficiency of 100 %. The $W\gamma$ + CCDY limits are an extrapolation of a previous CMS tri-lepton search [140] based on the findings of [141] (light blue) and a MG5aMC simulation at FCC energy [139] (yellow-grey). Indirect limits come from electroweak precision tests [137] (light grey), and non-observation of charged Lepton Flavour Violation [138] (light pink). The end points of these curves correspond to a Yukawa coupling reaching a non-perturbative limit, in the theory employed for deriving the V^2-bounds. For further information see Chapters 2 and 3.

of $|V_{e1}|^2 : |V_{\mu 1}|^2 : |V_{\tau 1}|^2 \equiv 0.06 : 0.46 : 0.48$.

At the FCC-hh (again assuming a background-free search and 100 % detector efficiency, but at a luminosity of $30\,\mathrm{ab}^{-1}$) the exclusion limit could be as low as $|V_{\ell 1}|^2 \sim (3\text{–}5) \times 10^{-4}$ for $r_{\mathrm{N}} \sim$ few in a mass range of $m_{\mathrm{N}_1} \sim$ few TeV. These bounds are competitive with EWPT exclusion. Further, in the TeV range, they are expected to improve on bounds by DY + $W\gamma$ [139]. The exclusion coming from cLFV is expected to be stronger for all masses m_{N1}. Nevertheless, exclusions derived from cLFV necessarily assume a hierarchy between an HNL's mixing angles to different leptons. Therefore, comparable mixing exclusions from searches like WBF are important as they serve as a more direct way of accessing this parameter space.

We note again that the Fuks et al. analysis [101] for a phenomenological type-I seesaw HNL showed large implicit backgrounds for $m_{\mathrm{N}} < 1\,\mathrm{TeV}$, while giving a signal efficiency of $\sim 40\,\%$ in the TeV range. This corresponds to a correction factor of $(0.4)^{-0.5} = 1.6$ to the effective reach concerning $|V_{\ell 1}|^2$.

4.2.1 Perspective of W Boson Fusion Detector Discovery

In this thesis, we explored the potential of the W Boson Fusion at high energy proton-proton colliders. We concluded that — for the planed HL-LHC parameters — it can only contribute meaningful mixing bounds in a quasi-Dirac-like HNL model with HNL mass $m_{\mathrm{N}_1} < 1\,\mathrm{TeV}$ and mass m_{N_2} corresponding to a mass ratio $r_{\mathrm{N}} \sim 2$–10. For FCC parameters, the mass range can be extended to $m_{\mathrm{N}_1} \sim$ few TeV yielding competitive limits for such mass ratios (see Fig. 4.1).

The already existing bounds derived from the WBF process [86] can be reinterpreted as bounds on a two HNL model in the highly hierarchical limit.[2] It is important to note that this does not correspond to a decoupling in the traditional sense, as the "decoupled" and "non-decoupled" HNLs' mixing angles are explicitly related by the requirement that neutrino masses remain as observed experimentally.[3]

Many theoretical considerations point to neutrino sector models featuring degenerate HNL (see Section 1.2). As shown in Figs. E.8a and E.8e, WBF — unlike its decay experiment equivalent $0\nu\beta\beta$ [142, 143] — could not contribute any meaningful exclusion on mixing bounds.[4] However, in models such as the ARS (see Section 1.2.3), the relevant parameter space considered in this work is compatible with HNL induced leptogenesis.

For an HNL pair with mixing angles at the "seesaw line", there is little hope of detector discovery in the foreseeable future Appendices A and B, as the cross sections are ~ 20 orders of magnitude below those with mixings near 1.

4.2.2 General Implications

The general considerations of cancellations in the lepton number violating current (see Chapter 2) apply to all indirect LNV searches. This means that if an HNL is not allowed to go on-shell — resulting in HNL oscillations in degenerate models [60, 61] — such an amplitude level suppression will occur. As the requirement of on-shell HNLs greatly limits the accessible HNL mass range by the experiments energy, it

[2] With the caveat of the perturbativity bound (Eq. (1.20)) for heavy HNLs limiting the applicable mass range.

[3] Unless motivated more fundamentally, such a requirement presents the "theoretical impurity" of large fine tuning between parameters.

[4] For even stronger degeneracy the plot would look the same but with an order of magnitude weaker bounds per order of magnitude in degeneracy according to Eq. (2.14).

is unlikely that lepton number violating processes will be observable *at colliders* for HNLs with masses above few TeV.

We saw that it is imperative for indirect searches to be conducted in a meaningful neutrino sector model in order to obtain meaningful observables. The quasi-Dirac-like model (see Section 2.2) prooved to be a good approximation of the minimal neutrino model required to explain neutrino oscillations (see Section 2.3). Therefore, and due to its easy implementation — even compared to the Casas-Ibarra parametrisation — such a model would be a natural choice for searches with HNL mixings above the "seesaw line" $|V^2| = m_\nu m_{\mathrm{N}}^{-1}$.

4.3 Outlook

A natural next step in furthering this analysis would be to consider the case of three HNLs. As this greatly opens up the available parameter space, *the single HNL case would not hold as an upper limit.* One parameterisation for the mixing angles $V_{\ell I}$ inspired by the qDl condition (Eq. (1.23)) could for example be

$$V_{\ell 1} = \sqrt{r_{\mathrm{N12}}} V_{\ell 2} = i \sqrt{\frac{r_{\mathrm{N13}}}{2}} V_{\ell 3}, \tag{4.1}$$

with mass ratios $r_{\mathrm{N}IJ}$. Such a parametrisation would increase the cross section by a factor of eight in the limit of $r_{\mathrm{N12}} = 1$, $r_{\mathrm{N13}} \gg 1$. To restrict the available parameter space, one could conduct the search respecting bounds set by baryon asymmetry of the universe (see Section 1.2.3).

It has been pointed out in past literature [50] that unlike lepton number violating processes, lepton number conserving but lepton *flavour* violating processes (LFV) do not suffer from intrinsic amplitude level suppression. However, it is known that a degenerate HNL pair combines to form a Dirac particle (c.f. [144] and Appendix C). Therefore, when considering models relying on a degenerate HNL pair (see Section 1.2.3), also LFV searches — at least when considered as an indirect search — are not likely going to lead to collider based HNL discovery.[5] We note that this cancellation does not generalise to the three HNL case.

It will also be worthwhile to consider a similar analysis to the one conducted here $2 \to 4$ in a MG5aMC simulation. One important aspect to investigate is the question of how a tendency toward front-back scattering in the WW system for smaller mass ratios translates into angular distributions of the full pp scattering.

[5] This is especially true as larger implicit backgrounds have to be considered for such a study.

This will need to be investigated in a full $2 \to 4$ simulation of the process as this phenomenon only occurs for m_{N1} regime outside the full validity of the EWA, while all angular dependence is strongly suppressed for HNLs with $m_{\mathrm{N1}} \gtrsim$ few TeV. If indeed front-to-back scattering translates into large lepton pseudorapidities at pp level, the drop off for smaller r_{N} with respect to realistic detection prospects could be even more severe than anticipated. However, due to the detection limits at the (HL-)LHC, this question is more relevant for searches at FCC energy. To this end, existing HeavyN UFO libraries would have to be extended to accommodate complex mixing angles, which, unfortunately, was not possible due to time restrictions.[6]

As, demonstrated by Fuks et. al, NLO effects in QCD can have an impact on the exact numerical values $\mathcal{O}(10\,\%)$. It remains to be seen if loop-order corrections to the $W^{\pm}W^{\pm} \to \ell^{\pm}\ell^{\pm}$ system could potentially alter the expected signal more significantly. Especially penguin corrections to the $W\mathrm{N}\ell$ vertices (see Fig. E.1b), which have been shown to contribute for large HNL masses [138], and corrections to the Majorana propagator — similar to those responsible for running of light neutrino masses shown in Fig. E.1d — could be of interest here.

[6] If such a library were implemented, this would also greatly facilitate a three HNL study of the process.

Bibliography

[1] P. Langacker, *Introduction to the Standard Model and Electroweak Physics*, in *Theoretical Advanced Study Institute in Elementary Particle Physics: The Dawn of the LHC Era*, pp. 3–48, 2010, 0901.0241, DOI.

[2] M. D. Schwartz, *Quantum Field Theory and the Standard Model*. Cambridge University Press, 3, 2014.

[3] S. L. Glashow, *Partial-symmetries of weak interactions*, *Nuclear Physics* **22** (1961) 579.

[4] S. Weinberg, *A model of leptons*, *Phys. Rev. Lett.* **19** (1967) 1264.

[5] A. Salam, *Weak and Electromagnetic Interactions*, *Conf. Proc. C* **680519** (1968) 367.

[6] ATLAS collaboration, G. Aad et al., *Observation of a new particle in the search for the Standard Model Higgs boson with the ATLAS detector at the LHC*, *Phys. Lett. B* **716** (2012) 1 [1207.7214].

[7] CMS collaboration, S. Chatrchyan et al., *Observation of a New Boson at a Mass of 125 GeV with the CMS Experiment at the LHC*, *Phys. Lett. B* **716** (2012) 30 [1207.7235].

[8] Muon $g-2$ Collaboration collaboration, B. Abi, T. Albahri, S. Al-Kilani, D. Allspach, L. P. Alonzi, A. Anastasi et al., *Measurement of the positive muon anomalous magnetic moment to 0.46 ppm*, *Phys. Rev. Lett.* **126** (2021) 141801.

[9] T. Aaltonen, S. Amerio, D. Amidei, A. Anastassov, A. Annovi, J. Antos et al., *High-precision measurement of the w boson mass with the cdf ii detector*, *Science* **376** (2022) 170.

[10] C. N. Yang and R. L. Mills, *Conservation of isotopic spin and isotopic gauge invariance*, *Phys. Rev.* **96** (1954) 191.

[11] F. Englert and R. Brout, *Broken symmetry and the mass of gauge vector mesons*, *Phys. Rev. Lett.* **13** (1964) 321.

[12] P. W. Higgs, *Broken symmetries and the masses of gauge bosons*, *Phys. Rev. Lett.* **13** (1964) 508.

[13] P. W. Higgs, *Spontaneous symmetry breakdown without massless bosons*, *Phys. Rev.* **145** (1966) 1156.

[14] S. Coleman and E. Weinberg, *Radiative corrections as the origin of spontaneous symmetry breaking*, *Phys. Rev. D* **7** (1973) 1888.

[15] M. Sher, *Electroweak Higgs Potentials and Vacuum Stability*, *Phys. Rept.* **179** (1989) 273.

[16] A. Strumia and F. Vissani, *Neutrino masses and mixings and ...*, *arXiv e-prints* (2006) [hep-ph/0606054].

[17] N. Cabibbo, *Unitary symmetry and leptonic decays*, *Phys. Rev. Lett.* **10** (1963) 531.

[18] M. Kobayashi and T. Maskawa, *CP-Violation in the Renormalizable Theory of Weak Interaction*, *Progress of Theoretical Physics* **49** (1973) 652.

[19] W. Pauli, *Aufsätze und Vorträge über Physik und Erkenntnistheorie*, Die Wissenschaft. Vieweg+teubner Verlag, Jan., 1961.

[20] E. Fermi, *Tentativo di una teoria dei raggi β*, *Il Nuovo Cimento (1924-1942)* **11** (1934) 1.

[21] F. Reines and C. L. Cowan jr., *The neutrino*, *Nature* **178** (1956) 446.

[22] C. S. Wu, E. Ambler, R. W. Hayward, D. D. Hoppes and R. P. Hudson, *Experimental test of parity conservation in beta decay*, *Phys. Rev.* **105** (1957) 1413.

[23] M. Goldhaber, L. Grodzins and A. W. Sunyar, *Helicity of neutrinos*, *Phys. Rev.* **109** (1958) 1015.

[24] M. Aker, A. Beglarian, J. Behrens, A. Berlev, U. Besserer, B. Bieringer et al., *Direct neutrino-mass measurement with sub-electronvolt sensitivity*, *Nature Physics* **18** (2022) 160.

[25] C. Dvorkin et al., *Neutrino Mass from Cosmology: Probing Physics Beyond the Standard Model*, 1903.03689.

[26] R. Davis, D. S. Harmer and K. C. Hoffman, *Search for neutrinos from the sun*, *Phys. Rev. Lett.* **20** (1968) 1205.

[27] J. N. Bahcall, *Solar models: An Historical overview*, *AAPPS Bull.* **12** (2002) 12 [astro-ph/0209080].

[28] SNO collaboration, Q. R. Ahmad, R. C. Allen, T. C. Andersen, J. D. Anglin, G. Bühler, J. C. Barton et al., *Measurement of the rate of $\nu_e + d \to p + p + e^-$ interactions produced by ^8b solar neutrinos at the sudbury neutrino observatory*, *Phys. Rev. Lett.* **87** (2001) 071301.

[29] S. P. Mikheyev and A. Y. Smirnov, *Resonance Amplification of Oscillations in Matter and Spectroscopy of Solar Neutrinos*, *Sov. J. Nucl. Phys.* **42** (1985) 913.

[30] L. Wolfenstein, *Neutrino oscillations in matter*, *Phys. Rev. D* **17** (1978) 2369.

[31] Super-Kamiokande collaboration, Y. Fukuda et al., *Evidence for oscillation of atmospheric neutrinos*, *Phys. Rev. Lett.* **81** (1998) 1562 [hep-ex/9807003].

[32] B. Pontecorvo, *Mesonium and anti-mesonium*, *Sov. Phys. JETP* **6** (1957) 429.

[33] B. Pontecorvo, *Neutrino Experiments and the Problem of Conservation of Leptonic Charge*, *Zh. Eksp. Teor. Fiz.* **53** (1967) 1717.

[34] M. Drewes, *The Phenomenology of Right Handed Neutrinos*, *Int. J. Mod. Phys.* **E22** (2013) 1330019 [1303.6912].

[35] Z. Maki, M. Nakagawa and S. Sakata, *Remarks on the unified model of elementary particles*, *Prog. Theor. Phys.* **28** (1962) 870.

[36] S. Adrián-Martínez, M. Ageron, F. Aharonian, S. Aiello, A. Albert, F. Ameli et al., *Letter of intent for KM3net 2.0*, *Journal of Physics G: Nuclear and Particle Physics* **43** (2016) 084001.

[37] S. Weinberg, *Baryon and Lepton Nonconserving Processes*, *Phys. Rev. Lett.* **43** (1979) 1566.

[38] S. Antusch, O. Fischer, A. Hammad and C. Scherb, *Low scale type ii seesaw: present constraints and prospects for displaced vertex searches*, *Journal of High Energy Physics* **2019** (2019) 157.

[39] R. Franceschini, T. Hambye and A. Strumia, *Type-III see-saw at LHC*, *Phys. Rev. D* **78** (2008) 033002 [0805.1613].

[40] A. Atre, T. Han, S. Pascoli and B. Zhang, *The search for heavy majorana neutrinos*, *Journal of High Energy Physics* **2009** (2009) 030.

[41] S. Alekhin et al., *A facility to Search for Hidden Particles at the CERN SPS: the SHiP physics case*, *Rept. Prog. Phys.* **79** (2016) 124201 [1504.04855].

[42] A. M. Abdullahi et al., *The Present and Future Status of Heavy Neutral Leptons*, in *2022 Snowmass Summer Study*, 3, 2022, 2203.08039.

[43] P. Minkowski, $\mu \to e\gamma$ *at a Rate of One Out of* 10^9 *Muon Decays?*, *Phys. Lett. B* **67** (1977) 421.

[44] P. Ramond, *The Family Group in Grand Unified Theories*, in *International Symposium on Fundamentals of Quantum Theory and Quantum Field Theory*, 2, 1979, hep-ph/9809459.

[45] R. N. Mohapatra and G. Senjanovic, *Neutrino Mass and Spontaneous Parity Nonconservation*, *Phys. Rev. Lett.* **44** (1980) 912.

[46] T. Yanagida, *Horizontal Symmetry and Masses of Neutrinos*, *Prog. Theor. Phys.* **64** (1980) 1103.

[47] SINDRUM II collaboration, J. Kaulard et al., *Improved limit on the branching ratio of mu- –> e+ conversion on titanium*, *Phys. Lett. B* **422** (1998) 334.

[48] T. Asaka, S. Blanchet and M. Shaposhnikov, *The nuMSM, dark matter and neutrino masses*, *Phys. Lett. B* **631** (2005) 151 [hep-ph/0503065].

[49] M. Shaposhnikov, *A Possible symmetry of the nuMSM*, *Nucl. Phys. B* **763** (2007) 49 [hep-ph/0605047].

[50] J. Kersten and A. Yu. Smirnov, *Right-Handed Neutrinos at CERN LHC and the Mechanism of Neutrino Mass Generation*, *Phys. Rev.* **D76** (2007) 073005 [0705.3221].

[51] E. Akhmedov, *Majorana neutrinos and other Majorana particles:Theory and experiment*. 12, 2014. 1412.3320.

[52] R. N. Mohapatra and J. W. F. Valle, *Neutrino mass and baryon-number nonconservation in superstring models*, *Phys. Rev. D* **34** (1986) 1642.

[53] D. Wyler and L. Wolfenstein, *Massless neutrinos in left-hand symmetric models*, *Nuclear Physics B* **218** (1983) 205.

[54] G. Branco, W. Grimus and L. Lavoura, *The seesaw mechanism in the presence of a conserved lepton number*, *Nuclear Physics B* **312** (1989) 492.

[55] M. Gonzalez-Garcia and J. Valle, *Fast decaying neutrinos and observable flavour violation in a new class of majoron models*, *Physics Letters B* **216** (1989) 360.

[56] A. Roy and M. Shaposhnikov, *Resonant production of the sterile neutrino dark matter and fine-tunings in the nuMSM*, *Phys. Rev. D* **82** (2010) 056014 [1006.4008].

[57] M. B. Gavela, T. Hambye, D. Hernandez and P. Hernandez, *Minimal Flavour Seesaw Models*, *JHEP* **09** (2009) 038 [0906.1461].

[58] A. Pilaftsis, *Radiatively induced neutrino masses and large Higgs neutrino couplings in the standard model with Majorana fields*, *Z. Phys. C* **55** (1992) 275 [hep-ph/9901206].

[59] M. Drewes, J. Klarić and P. Klose, *On lepton number violation in heavy neutrino decays at colliders*, *JHEP* **11** (2019) 032 [1907.13034].

[60] J.-L. Tastet and I. Timiryasov, *Dirac vs. Majorana HNLs (and their oscillations) at SHiP*, *JHEP* **04** (2020) 005 [1912.05520].

[61] J.-L. Tastet, O. Ruchayskiy and I. Timiryasov, *Reinterpreting the ATLAS bounds on heavy neutral leptons in a realistic neutrino oscillation model*, *JHEP* **12** (2021) 182 [2107.12980].

[62] D. Aristizabal Sierra and C. E. Yaguna, *On the importance of the 1-loop finite corrections to seesaw neutrino masses*, *JHEP* **08** (2011) 013 [1106.3587].

[63] J. Lopez-Pavon, E. Molinaro and S. T. Petcov, *Radiative Corrections to Light Neutrino Masses in Low Scale Type I Seesaw Scenarios and Neutrinoless Double Beta Decay*, *JHEP* **11** (2015) 030 [1506.05296].

[64] E. H. Aeikens, P. M. Ferreira, W. Grimus, D. Jurčiukonis and L. Lavoura, *Radiative seesaw corrections and charged-lepton decays in a model with soft flavour violation*, *JHEP* **12** (2020) 122 [2009.13479].

[65] T. Asaka and M. Shaposhnikov, *The νMSM, dark matter and baryon asymmetry of the universe*, *Phys. Lett. B* **620** (2005) 17 [hep-ph/0505013].

[66] A. Boyarsky, O. Ruchayskiy and M. Shaposhnikov, *The Role of sterile neutrinos in cosmology and astrophysics*, *Ann. Rev. Nucl. Part. Sci.* **59** (2009) 191 [0901.0011].

[67] G. L. Fogli, S. N. Gninenko, D. S. Gorbunov and M. E. Shaposhnikov, *Search for gev-scale sterile neutrinos responsible for active neutrino oscillations and baryon asymmetry of the universe*, *Advances in High Energy Physics* **2012** (2012) 718259.

[68] CMS Collaboration, *A measurement of the Higgs boson mass in the diphoton decay channel*, *arXiv e-prints* (2020) [2002.06398].

[69] S. Tremaine and J. E. Gunn, *Dynamical Role of Light Neutral Leptons in Cosmology*, *Phys. Rev. Lett.* **42** (1979) 407.

[70] X.-D. Shi and G. M. Fuller, *A New dark matter candidate: Nonthermal sterile neutrinos*, *Phys. Rev. Lett.* **82** (1999) 2832 [astro-ph/9810076].

[71] X.-G. He, T. Li and W. Liao, *Symmetry, dark matter, and LHC phenomenology of the minimal νSM*, *prd* **81** (2010) 033006 [0911.1598].

[72] M. Shaposhnikov, *The nuMSM, leptonic asymmetries, and properties of singlet fermions*, *JHEP* **08** (2008) 008 [0804.4542].

[73] E. K. Akhmedov, V. A. Rubakov and A. Y. Smirnov, *Baryogenesis via neutrino oscillations*, *Phys. Rev. Lett.* **81** (1998) 1359 [hep-ph/9803255].

[74] M. Drewes, B. Garbrecht, P. Hernandez, M. Kekic, J. Lopez-Pavon, J. Racker et al., *ARS Leptogenesis*, *Int. J. Mod. Phys.* **A33** (2018) 1842002 [1711.02862].

[75] A. Abada, G. Arcadi, V. Domcke, M. Drewes, J. Klaric and M. Lucente, *Low-scale leptogenesis with three heavy neutrinos*, *JHEP* **01** (2019) 164 [1810.12463].

[76] M. Drewes and B. Garbrecht, *Leptogenesis from a GeV Seesaw without Mass Degeneracy*, *JHEP* **03** (2013) 096 [1206.5537].

[77] M. Drewes, Y. Georis and J. Klarić, *Mapping the Viable Parameter Space for Testable Leptogenesis*, *Phys. Rev. Lett.* **128** (2022) 051801 [2106.16226].

[78] M. Goeppert-Mayer, *Double beta-disintegration*, *Phys. Rev.* **48** (1935) 512.

[79] B. Pontecorvo, *Superweak interactions and double beta decay*, *Phys. Lett. B* **26** (1968) 630.

[80] M. J. Dolinski, A. W. P. Poon and W. Rodejohann, *Neutrinoless Double-Beta Decay: Status and Prospects*, *Ann. Rev. Nucl. Part. Sci.* **69** (2019) 219 [1902.04097].

[81] V. Cirigliano et al., *Neutrinoless Double-Beta Decay: A Roadmap for Matching Theory to Experiment*, 2203.12169.

[82] L. Cardani, *Neutrinoless Double Beta Decay Overview*, *SciPost Phys. Proc.* **1** (2019) 024 [1810.12828].

[83] T. Asaka, H. Ishida and K. Tanaka, *Neutrinoless double beta decays tell nature of right-handed neutrinos*, 2101.12498.

[84] T. Asaka, H. Ishida and K. Tanaka, *What if a specific neutrinoless double beta decay is absent?*, *PTEP* **2021** (2021) 063B01 [2012.13186].

[85] T. Asaka, H. Ishida and K. Tanaka, *Hiding neutrinoless double beta decay in the minimal seesaw mechanism*, *Phys. Rev. D* **103** (2021) 015014 [2012.12564].

[86] CMS collaboration, *Probing heavy Majorana neutrinos and the Weinberg operator through vector boson fusion processes in proton-proton collisions at $\sqrt{s}$ = 13 TeV*, 2206.08956.

[87] ATLAS collaboration, G. Aad et al., *Inclusive search for same-sign dilepton signatures in pp collisions at $\sqrt{s} = 7$ TeV with the ATLAS detector*, *JHEP* **10** (2011) 107 [1108.0366].

[88] ATLAS collaboration, G. Aad et al., *Search for heavy neutrinos and right-handed W bosons in events with two leptons and jets in pp collisions at $\sqrt{s} = 7$ TeV with the ATLAS detector*, *Eur. Phys. J. C* **72** (2012) 2056 [1203.5420].

[89] CMS collaboration, S. Chatrchyan et al., *Search for heavy Majorana Neutrinos in $\mu^{\pm}\mu^{\pm}$+ Jets and $e^{\pm}e^{\pm}$+ Jets Events in pp Collisions at $\sqrt{s} = 7$ TeV*, *Phys. Lett. B* **717** (2012) 109 [1207.6079].

[90] ATLAS collaboration, G. Aad et al., *Search for heavy Majorana neutrinos with the ATLAS detector in pp collisions at $\sqrt{s} = 8$ TeV*, *JHEP* **07** (2015) 162 [1506.06020].

[91] CMS collaboration, V. Khachatryan et al., *Search for heavy Majorana neutrinos in $\mu^{\pm}\mu^{\pm}$+ jets events in proton-proton collisions at $\sqrt{s}$ = 8 TeV*, *Phys. Lett. B* **748** (2015) 144 [1501.05566].

[92] CMS collaboration, V. Khachatryan et al., *Search for heavy Majorana neutrinos in $e^{\pm}e^{\pm}$+ jets and $e^{\pm}$ $\mu^{\pm}$+ jets events in proton-proton collisions at $\sqrt{s} = 8$ TeV*, *JHEP* **04** (2016) 169 [1603.02248].

[93] ATLAS collaboration, M. Aaboud et al., *Search for heavy Majorana or Dirac neutrinos and right-handed W gauge bosons in final states with two charged leptons and two jets at $\sqrt{s} = 13$ TeV with the ATLAS detector*, *JHEP* **01** (2019) 016 [1809.11105].

[94] CMS collaboration, A. M. Sirunyan et al., *Search for a heavy right-handed W boson and a heavy neutrino in events with two same-flavor leptons and two jets at $\sqrt{s}$ = 13 TeV*, *JHEP* **05** (2018) 148 [1803.11116].

[95] CMS collaboration, A. M. Sirunyan et al., *Search for heavy Majorana neutrinos in same-sign dilepton channels in proton-proton collisions at $\sqrt{s} = 13$ TeV*, *JHEP* **01** (2019) 122 [1806.10905].

[96] CMS collaboration, A. M. Sirunyan et al., *Search for heavy neutrinos and third-generation leptoquarks in hadronic states of two τ leptons and two jets in proton-proton collisions at $\sqrt{s}$ = 13 TeV*, *JHEP* **03** (2019) 170 [1811.00806].

[97] D. A. Dicus, D. D. Karatas and P. Roy, *Lepton nonconservation at supercollider energies*, *Phys. Rev. D* **44** (1991) 2033.

[98] A. Ali, A. V. Borisov and N. B. Zamorin, *Same-sign Dilepton Production via Heavy Majorana Neutrinos in Proton–proton Collisions*, in *10th Lomonosov Conference on Elementary Particle Physics*, pp. 74–79, 2003, hep-ph/0112043, DOI.

[99] O. Panella, M. Cannoni, C. Carimalo and Y. N. Srivastava, *Signals of heavy Majorana neutrinos at hadron colliders*, *Phys. Rev. D* **65** (2002) 035005 [hep-ph/0107308].

[100] J. N. Ng, A. de la Puente and B. W.-P. Pan, *Search for Heavy Right-Handed Neutrinos at the LHC and Beyond in the Same-Sign Same-Flavor Leptons Final State*, *JHEP* **12** (2015) 172 [1505.01934].

[101] B. Fuks, J. Neundorf, K. Peters, R. Ruiz and M. Saimpert, *Majorana neutrinos in same-sign $W^{\pm}W^{\pm}$ scattering at the LHC: Breaking the TeV barrier*, *Phys. Rev. D* **103** (2021) 055005 [2011.02547].

[102] F. del Aguila, J. A. Aguilar-Saavedra and R. Pittau, *Heavy neutrino signals at large hadron colliders*, *JHEP* **10** (2007) 047 [hep-ph/0703261].

[103] C. Degrande, O. Mattelaer, R. Ruiz and J. Turner, *Fully-Automated Precision Predictions for Heavy Neutrino Production Mechanisms at Hadron Colliders*, *Phys. Rev. D* **94** (2016) 053002 [1602.06957].

[104] D. Berdine, N. Kauer and D. Rainwater, *Breakdown of the narrow width approximation for new physics*, *Phys. Rev. Lett.* **99** (2007) 111601.

[105] E. Fuchs, S. Thewes and G. Weiglein, *Interference effects in BSM processes with a generalised narrow-width approximation*, *Eur. Phys. J. C* **75** (2015) 254 [1411.4652].

[106] A. Datta, M. Guchait and A. Pilaftsis, *Probing lepton number violation via majorana neutrinos at hadron supercolliders*, *Phys. Rev. D* **50** (1994) 3195 [hep-ph/9311257].

[107] G. L. Kane, *WINDOWS FOR NEW PHYSICS AT SUPER COLLIDERS*, in *The Physics of the 21st Century*, 12, 1983.

[108] S. Dawson, *The Effective W Approximation*, *Nucl. Phys. B* **249** (1985) 42.

[109] D. J. Gross and F. Wilczek, *Ultraviolet Behavior of Nonabelian Gauge Theories*, *Phys. Rev. Lett.* **30** (1973) 1343.

[110] H. D. Politzer, *Asymptotic Freedom: An Approach to Strong Interactions*, *Phys. Rept.* **14** (1974) 129.

[111] J. D. Bjorken and E. A. Paschos, *Inelastic Electron Proton and gamma Proton Scattering, and the Structure of the Nucleon*, *Phys. Rev.* **185** (1969) 1975.

[112] J. J. Ethier and E. R. Nocera, *Parton Distributions in Nucleons and Nuclei*, *Ann. Rev. Nucl. Part. Sci.* **70** (2020) 43 [2001.07722].

[113] C. v. Weizsäcker, *Ausstrahlung bei stößen sehr schneller elektronen*, *Zeitschrift für Physik* **88** (1934) 612.

[114] S. J. Brodsky, T. Kinoshita and H. Terazawa, *Two-photon mechanism of particle production by high-energy colliding beams*, *Phys. Rev. D* **4** (1971) 1532.

[115] Z. Kunszt and D. E. Soper, *On the Validity of the Effective W Approximation*, *Nucl. Phys. B* **296** (1988) 253.

[116] I. Esteban, M. C. Gonzalez-Garcia, M. Maltoni, T. Schwetz and A. Zhou, *The fate of hints: updated global analysis of three-flavor neutrino oscillations*, *Journal of High Energy Physics* **2020** (2020) 178.

[117] R. E. Ruiz, *Hadron Collider Tests of Neutrino Mass-Generating Mechanisms*, Ph.D. thesis, Pittsburgh U., 2015. 1509.06375.

[118] L. B. Okun, *Leptons and Quarks*. North-Holland, Amsterdam, Netherlands, 1982, 10.1142/9162.

[119] A. D. Martin, W. J. Stirling, R. S. Thorne and G. Watt, *Parton distributions for the lhc*, *The European Physical Journal C* **63** (2009) 189.

[120] A. Denner, H. Eck, O. Hahn and J. Kublbeck, *Feynman rules for fermion number violating interactions*, *Nucl. Phys. B* **387** (1992) 467.

[121] A. Denner, H. Eck, O. Hahn and J. Kublbeck, *Compact Feynman rules for Majorana fermions*, *Phys. Lett. B* **291** (1992) 278.

[122] J. Gluza and M. Zraek, *Feynman rules for majorana-neutrino interactions*, *Phys. Rev. D* **45** (1992) 1693.

[123] J. A. Casas and A. Ibarra, *Oscillating neutrinos and $\mu \to e, \gamma$*, *Nucl. Phys. B* **618** (2001) 171 [hep-ph/0103065].

[124] Z.-z. Xing, *Casas-Ibarra Parametrization and Unflavored Leptogenesis*, *Chin. Phys. C* **34** (2010) 1 [0902.2469].

[125] *Nufit 5.1*, 2021.

[126] A. Cabrera, Y. Han, M. Obolensky, F. Cavalier, J. Coelho, D. Navas-Nicolás et al., *Synergies and prospects for early resolution of the neutrino mass ordering*, *Scientific Reports* **12** (2022) 5393.

[127] I. Esteban, M. C. Gonzalez-Garcia, M. Maltoni, T. Schwetz and A. Zhou, *The fate of hints: updated global analysis of three-flavor neutrino oscillations*, *Journal of High Energy Physics* **2020** (2020) 178.

[128] *Ls3 schedule change*, Mar, 2022.

[129] A. Bastianin and M. Florio, *Initial guidelines for a social cost-benefit analysis of the FCC programme*, tech. rep., CERN, Geneva, Mar, 2019.

[130] R. Ruiz, A. Costantini, F. Maltoni and O. Mattelaer, *The Effective Vector Boson Approximation in high-energy muon collisions*, *JHEP* **06** (2022) 114 [2111.02442].

[131] M. Aleksa et al., *Calorimeters for the FCC-hh*, 1912.09962.

[132] M. Cacciari, G. P. Salam and G. Soyez, *The anti-k_t jet clustering algorithm*, *JHEP* **04** (2008) 063 [0802.1189].

[133] DELPHES 3 collaboration, J. de Favereau, C. Delaere, P. Demin, A. Giammanco, V. Lemaître, A. Mertens et al., *DELPHES 3, A modular framework for fast simulation of a generic collider experiment*, *JHEP* **02** (2014) 057 [1307.6346].

[134] O. Aberle, I. Béjar Alonso, O. Brüning, P. Fessia, L. Rossi, L. Tavian et al., *High-Luminosity Large Hadron Collider (HL-LHC): Technical design report*, CERN Yellow Reports: Monographs. CERN, Geneva, 2020, 10.23731/CYRM-2020-0010.

[135] FCC collaboration, A. Abada et al., *FCC Physics Opportunities: Future Circular Collider Conceptual Design Report Volume 1*, *Eur. Phys. J. C* **79** (2019) 474.

[136] B. Fuks, J. Neundorf, K. Peters, R. Ruiz and M. Saimpert, *Probing the Weinberg operator at colliders*, *Phys. Rev. D* **103** (2021) 115014 [2012.09882].

[137] E. Fernandez-Martinez, J. Hernandez-Garcia and J. Lopez-Pavon, *Global constraints on heavy neutrino mixing*, *JHEP* **08** (2016) 033 [1605.08774].

[138] K. A. Urquía Calderón, I. Timiryasov and O. Ruchayskiy, *Improved constraints and the prospects of detecting TeV to PeV scale Heavy Neutral Leptons*, 2206.04540.

[139] S. Pascoli, R. Ruiz and C. Weiland, *Heavy neutrinos with dynamic jet vetoes: multilepton searches at $\sqrt{s} = 14$, 27, and 100 TeV*, *JHEP* **06** (2019) 049 [1812.08750].

[140] CMS Collaboration collaboration, A. M. Sirunyan, A. Tumasyan, W. Adam, F. Ambrogi, E. Asilar, T. Bergauer et al., *Search for heavy neutral leptons in events with three charged leptons in proton-proton collisions at* $\sqrt{s} = 13$ TeV, *Phys. Rev. Lett.* **120** (2018) 221801.

[141] D. Alva, T. Han and R. Ruiz, *Heavy Majorana neutrinos from* $W\gamma$ *fusion at hadron colliders*, *JHEP* **02** (2015) 072 [1411.7305].

[142] M. Drewes and S. Eijima, *Neutrinoless double* β *decay and low scale leptogenesis*, *Phys. Lett. B* **763** (2016) 72 [1606.06221].

[143] P. Hernández, M. Kekic, J. López-Pavón, J. Racker and J. Salvado, *Testable Baryogenesis in Seesaw Models*, *JHEP* **08** (2016) 157 [1606.06719].

[144] S. Eijima, M. Shaposhnikov and I. Timiryasov, *Parameter space of baryogenesis in the* ν*MSM*, *JHEP* **07** (2019) 077 [1808.10833].

[145] C. Degrande, O. Mattelaer, R. Ruiz and J. Turner, *Fully automated precision predictions for heavy neutrino production mechanisms at hadron colliders*, *Physical Review D* **94** (2016) .

[146] D. Alva, T. Han and R. Ruiz, *Heavy majorana neutrinos from w*γ *fusion at hadron colliders*, *Journal of High Energy Physics* **2015** (2015) .

[147] A. Alloul, N. D. Christensen, C. Degrande, C. Duhr and B. Fuks, *FeynRules 2.0 a complete toolbox for tree-level phenomenology*, *Computer Physics Communications* **185** (2014) 2250.

[148] R. Mertig, M. Böhm and A. Denner, *Feyn calc - computer-algebraic calculation of feynman amplitudes*, *Computer Physics Communications* **64** (1991) 345.

[149] V. Shtabovenko, R. Mertig and F. Orellana, *New developments in FeynCalc 9.0*, *Computer Physics Communications* **207** (2016) 432.

[150] V. Shtabovenko, R. Mertig and F. Orellana, *FeynCalc 9.3: New features and improvements*, *Computer Physics Communications* **256** (2020) 107478.

[151] T. Stelzer and W. F. Long, *Automatic generation of tree level helicity amplitudes*, *Comput. Phys. Commun.* **81** (1994) 357 [hep-ph/9401258].

[152] J. Alwall, R. Frederix, S. Frixione, V. Hirschi, F. Maltoni, O. Mattelaer et al., *The automated computation of tree-level and next-to-leading order differential cross sections, and their matching to parton shower simulations*, *JHEP* **07** (2014) 079 [1405.0301].

[153] J. P. Ellis, *Tikz-feynman: Feynman diagrams with tikz*, *Computer Physics Communications* **210** (2017) 103.

Appendix

A More on the Single Heavy Neutral Lepton Model

Polarisation Decomposition

All data presented in this section is generated for the case of a single HNL with a mass of $m_{\mathrm{N}} = 150\,\mathrm{GeV}$ with a mixing angle $V_{\ell\mathrm{N}}$ such that $|V_{\ell\mathrm{N}}^2 m_{\mathrm{N}}| = 1\,\mathrm{eV} \simeq m_{\nu_e,\mathrm{upper}}$ (see Section 2.1). The resulting cross section decompositions are presented in Fig. A.1. They are shown as generated considering only contributions of the heavy mass state (Fig. A.1a), the light mass state (Fig. A.1b), and the combined contributions in the first flavour expansion (Fig. A.1c). The coincidence of the cross section generated with full polarisation vector summation rules and the sum of all polarised cross sections verifies the decomposition factors.

We see that for the heavy mass state contribution, the transversally polarised cross section dominates for very small centre of mass energies $\sqrt{M_{\mathrm{ww}}^2} \sim 2m_W$, but dies out quickly with growing $\sqrt{M_{\mathrm{ww}}^2}$. Meanwhile, the longitudinal polarisation grows with increasing $\sqrt{M_{\mathrm{ww}}^2}$, quickly dominating the overall cross section. For the light mass state contribution, the transversally polarised cross section is always the dominant contribution. Both transversal and longitudinal cross section become constant for large $\sqrt{M_{\mathrm{ww}}^2}$. The combined cross section is the result of destructive interference between heavy and light mass state. This can be easily seen from Fig. A.2, which shows the same data as presented in Fig. A.1, but ordered by polarisations. Here, Fig. A.2a compares the transversal cross sections of the light and heavy mass state in isolation and that of the combined cross section, while Fig. A.1c does the same for the longitudinal cross sections.

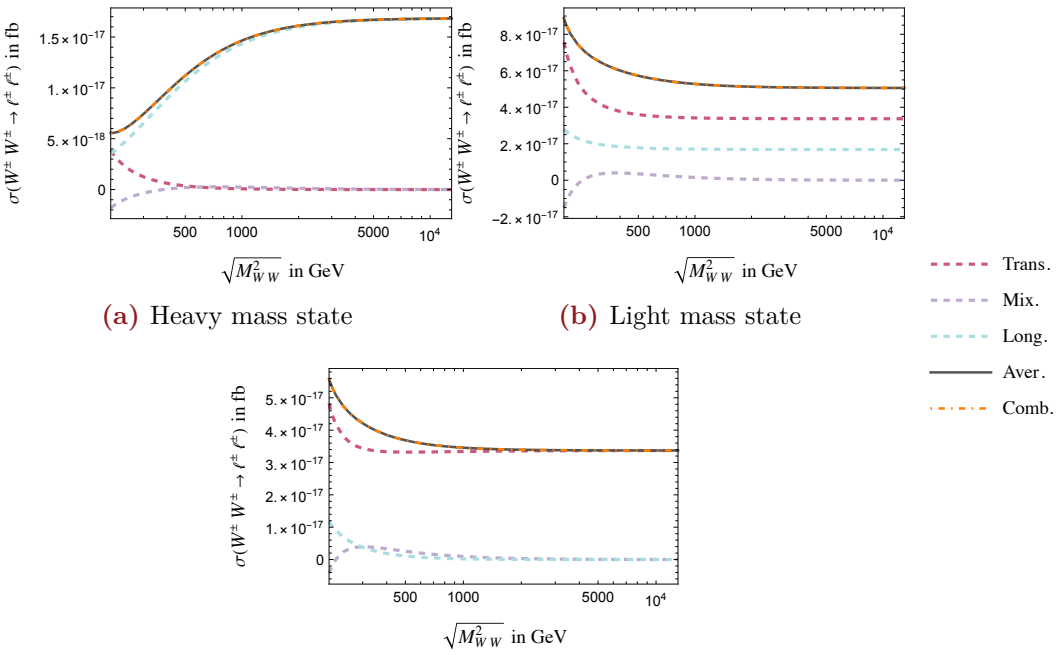

(a) Heavy mass state (b) Light mass state

(c) Combined

Figure A.1: Cross sections of $W^\pm W^\pm \to \ell^\pm \ell^\pm$ scattering as decompositions in the WW polarisations as Transversal $\leftrightarrow \sigma^{\mathrm{TT}}$, Mixed $\leftrightarrow \sigma^{\mathrm{LT}}$, and Longitudinal $\leftrightarrow \sigma^{\mathrm{LL}}$. The cross sections are given as a function of the centre of mass energy $\sqrt{M^2_{\mathrm{WW}}}$ for an HNL of mass 150 GeV. The average curve represents the cross section derived from the square amplitude with full massive vector boson polarisation sum rules, while the combined cross section is the sum of all polarised cross sections.

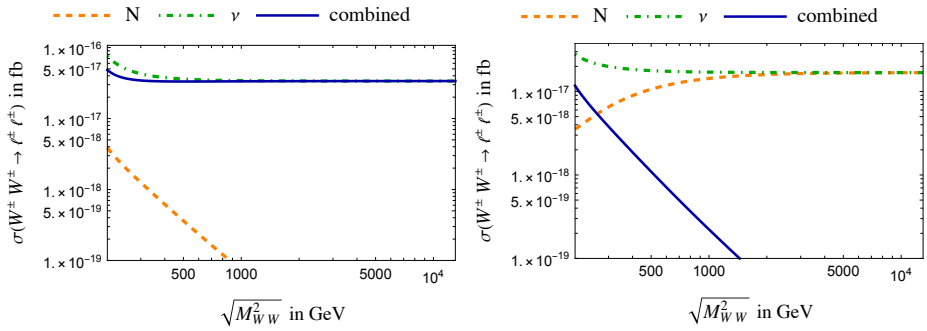

(a) Transversal (b) Longitudinal

Figure A.2: Polarised cross sections of $W^\pm W^\pm \to \ell^\pm \ell^\pm$ scattering as decompositions in the WW polarisations as Transversal $\leftrightarrow \sigma^{\mathrm{TT}}$ and Longitudinal $\leftrightarrow \sigma^{\mathrm{LL}}$. The cross sections are given as a function of the centre of mass energy $\sqrt{M^2_{\mathrm{WW}}}$ for an HNL of mass 150 GeV.

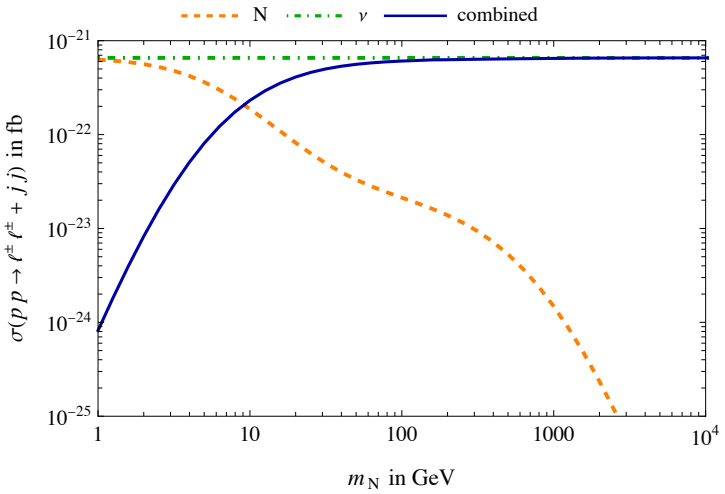

Figure A.3: Total cross section of $pp \to l^+ l^+ jj$ scattering as calculated in the effective W approximation. The mixing angle $V_{\ell \mathrm{N}}$ here is a function of the HNL mass as well, such that $|V_{\ell \mathrm{N}}^2 m_{\mathrm{N}}| = 1\,\mathrm{eV} \sim m_{\nu_e}$.

In this representation, it is easy to see that for large $\sqrt{M_{\mathrm{WW}}^2}$ the longitudinal components of the light and heavy mass state cancel so that the combined longitudinal cross section vanishes. The transversal cross section of the heavy mass state vanishes for large $\sqrt{M_{\mathrm{WW}}^2}$ while that of the light mass state remains constant. Therefore, the combined transversal cross section becomes asymptotically constant for large $\sqrt{M_{\mathrm{WW}}^2}$ as it approaches the value of the light mass state.

pp Level Cross Section

Figure A.3 shows the total cross section of $pp \to \ell^\pm \ell^\pm jj$ as calculated in the effective W approximation. The underlying neutrino sector model is that of a single HNL generating a light neutrino mass of 1 eV (see Section 2.1). We will not apply any rescaling to these cross sections as

i. the differential cross sections of this model compared to the phenomenological N_1 are substantially different (compare N Fig. E.3 and N_2 in Fig. E.4),

ii. the absolute value of this cross section would not change greatly — which is the main point of this plot.

The relative differences between the individual contributions are analogous to those of the $W^\pm W^\pm \to \ell^\pm \ell^\pm$ case (shown in Fig. 2.3). We see that also in the pp scattering

case the full cross section (shown in blue) is always smaller than that of the light neutrino contribution (dash-dotted green). The most significant difference occurs for the single HNL case (dashed orange) for $m_{\mathrm{N}} \sim 10^{1}$–$10^{2.5}\,\mathrm{GeV}$, where the curve describes a dent before eventually falling for growing m_{N}. This behaviour is due to the transversally polarised cross section (which dominates for small m_{N}) falling quicker for growing m_{N} than the longitudinally polarised cross section (dominant at larger m_{N}).[7] Since the numerical values in the PDF of the transversally polarised cross section are larger than that of the longitudinal equivalent, the regime in which the dominant polarisation changes presents itself as a dent in the curve. The absolute value of the cross section has decreased by about 4 orders of magnitude with respect to the $W^{\pm}W^{\pm} \to \ell^{\pm}\ell^{\pm}$ case.
Given the scale of 10^{-23}–$10^{-21}\,\mathrm{fb}$ of this cross section, there is no hope for detector discovery — assuming a single N model reconciled with light neutrino mass scales — in the foreseeable future.

B More on the Four Majorana State Model

Inverted hierarchy

In case of inverted hierarchy among the light neutrino mass states, the Casas-Ibarra Parametrisation (see Eq. (2.20)) for two HNLs yields

$$\begin{aligned} V_{\ell 1}^{\mathrm{CI}} &= i\frac{U_{\ell 1}\sqrt{m_{\nu 1}}\cos\omega - U_{\ell 2}\sqrt{m_{\nu 2}}\sin\omega}{\sqrt{m_{\mathrm{N}1}}} \\ V_{\ell 2}^{\mathrm{CI}} &= i\frac{U_{\ell 1}\sqrt{m_{\nu 1}}\sin\omega + U_{\ell 2}\sqrt{m_{\nu 2}}\cos\omega}{\sqrt{m_{\mathrm{N}2}}}. \end{aligned} \tag{B.1}$$

Here we have assumed the third neutrino mass state to be massless. With ν-fit data [125], this yields $U_{e1}^2 m_{\nu 1} = 33\,\mathrm{meV}$ and $U_{e2}^2 m_{\nu 2} = 12\,\mathrm{meV}$. If we compare this to $U_{e2}^2 m_{\nu 2} = 2.5\,\mathrm{meV}$ and $U_{e3}^2 m_{\nu 3} = 1.1\,\mathrm{meV}$ in the normal hierarchy case, we expect the observables to be qualitatively the same, and the absolute scale being separated by a factor of $33^2/2.5^2 = 175$. This conversion factor stems from the fact that observables scale as $V^4 \propto U^4 m_{\nu}^2$.

Figure B.1 compares the differential cross sections derived for normal and inverted hierarchy (NH and IH respectively) at the seesaw line ($\omega = 0i$) and in the case of strong enhancement ($\omega = 9i$). We se, that the above naive scaling translates into

[7] For a brief discussion of this find Section 3.1.1.

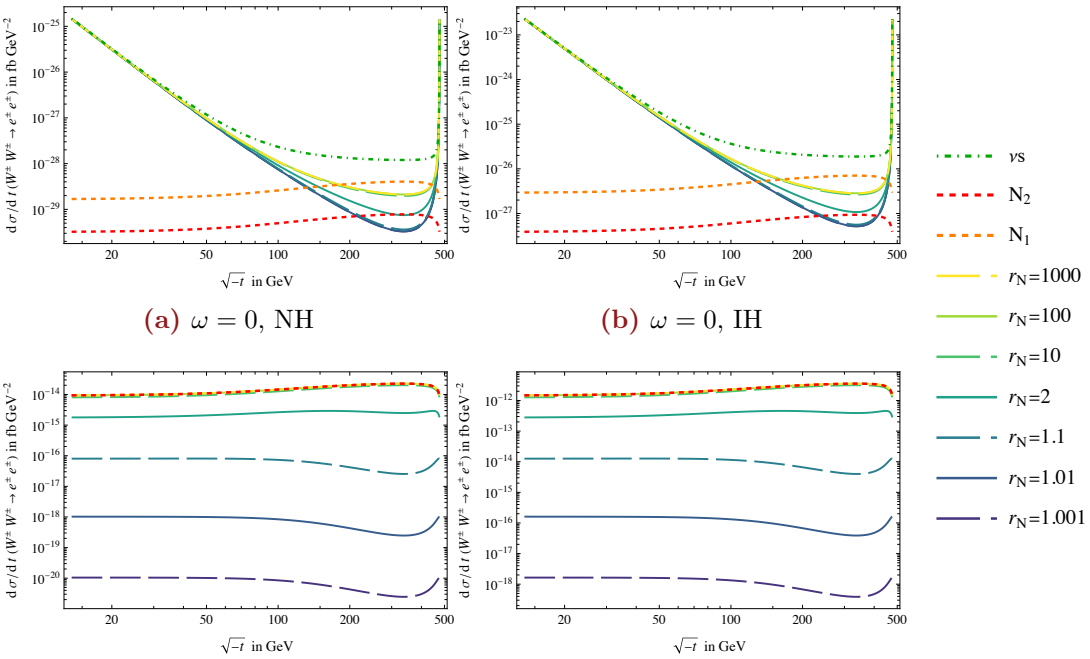

(a) $\omega = 0$, NH **(b)** $\omega = 0$, IH

(c) $\omega = 9i$, NH **(d)** $\omega = 9i$, IH

Figure B.1: Cross Section of $W^\pm W^\pm \to \ell^\pm \ell^\pm$ in case of normal (NH) and inverted (IH) light neutrino mass state hierarchy with two HNLs with mass ratio r_N. The mixing angles $V_{\ell N}$ are given in the Casas-Ibarra parametrisation with ω as indicated. The centre of mass energy is 490 TeV. In case $\omega = 9i$, the νs curve is orders of magnitude below the combined curves, and was left out for illustration purposes.

the observables, where all curves in the IH values are larger by about a factor of ~ 175, while the relative differences within the plots are the same in very good approximation. Importantly, in the large $\mathrm{Im}\,\omega$ limit, relevant for collider searches, only the absolute scale changes with $\mathrm{Im}\,\omega$, while the qualitative details of the differential cross section remain the same (see Fig. E.6). In this limit, the cross section scales with $\cosh(2\,\mathrm{Im}\,\omega) \simeq \frac{1}{2}\exp(2\,\mathrm{Im}\,\omega)$, so that the IH case can be recovered from the NH by appropriate rescaling

$$\mathrm{Im}\,\omega^{\mathrm{NH}} \simeq \mathrm{Im}\,\omega^{\mathrm{IH}} + \tfrac{1}{2}\log(175) = \mathrm{Im}\,\omega^{\mathrm{IH}} + 1.1\,. \tag{B.2}$$

pp Level Cross Section

The Figures in this section show the $pp \to \ell^\pm \ell^\pm jj$ cross section in a neutrino model where light neutrino masses are generated as perturbation of an HNL internal sym-

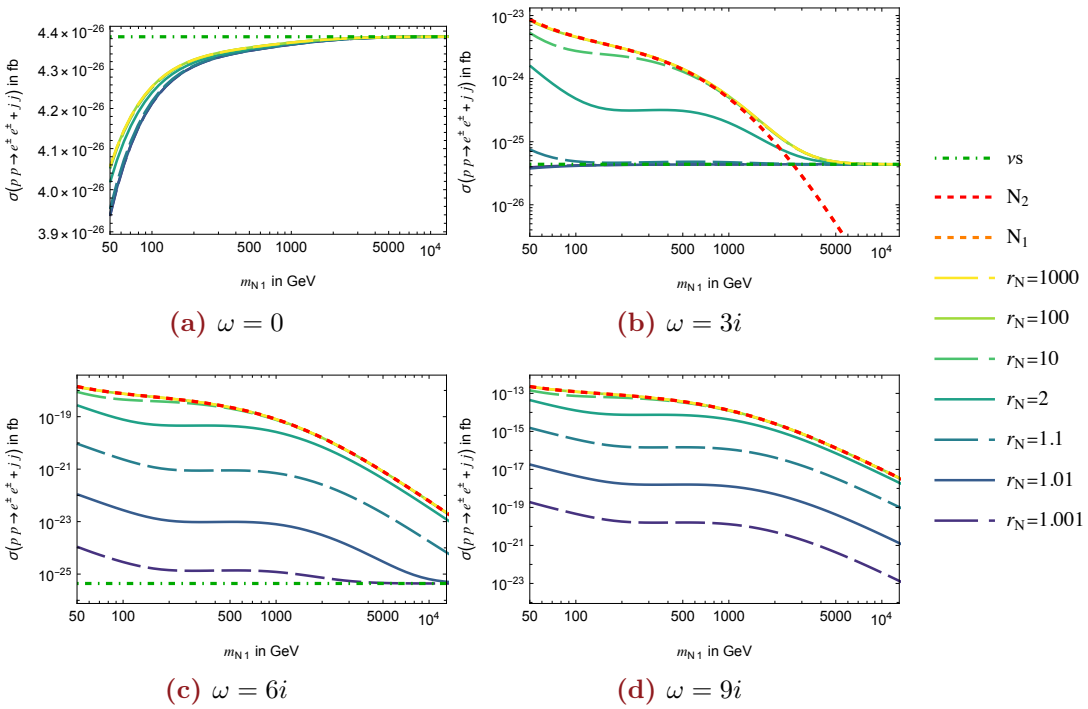

Figure B.2: Cross Section of $pp \to \ell^\pm\ell^\pm jj$ as calculated in the effective W approximation propagated by two HNLs with mass ratio r_N. The mixing angles $V_{\ell N}$ are given in the Casas-Ibarra parametrisation with ω as indicated. The centre of mass energy is $\sqrt{s} = 13\,\text{TeV}$. In case $\omega = 0$ ($\omega = 9i$), the N_I curves (νs curve) are orders of magnitude below the combined curves, and were left out for illustration purposes.

metry (see Section 2.3). In this section we will also not include any rescaling of the EWA results, due to analogous arguments presented in Appendix A.

Figure B.2 compares the cross section as a function of the lighter HNL mass m_N for different enhancement factors $\text{Im}\,\omega$. As in the WW case, for no enhancement the cross section is always dominated by the light neutrino contributions (Fig. B.2a). Here, the combined cross section converges with the light state cross section for very heavy Ns from below.
In the case of strong enhancement (Figs. B.2c and B.2d), the combined cross section is dominated by the heavy mass state contributions for significant parts of the shown m_N-range. For all shown mass ratios r_N we find that the combined cross section lies above the light mass state line with an upper limit determined by the heavy mass states, which is reached by highly hierarchical HNLs ($r_N \sim 10$). As can be seen explicitly in Fig. B.2c, for any ω there exists a critical mass m_N, where the

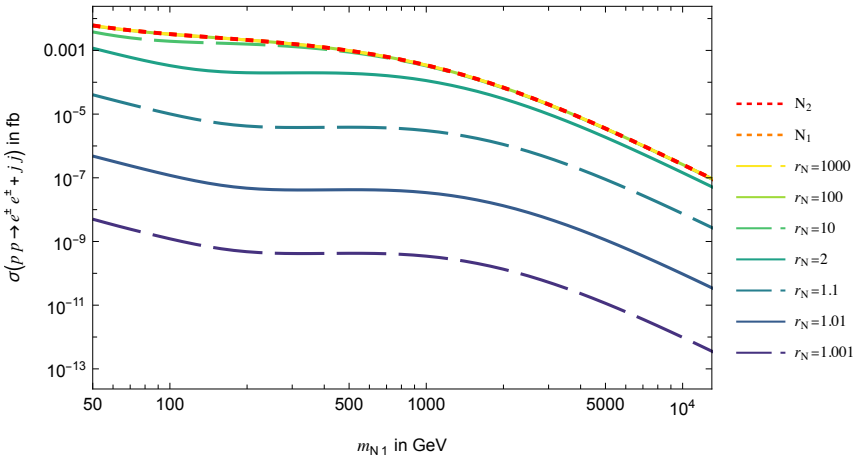

Figure B.3: Cross Section of $pp \to \ell^{\pm}\ell^{\pm}jj$ as calculated in the effective W approximation propagated by two HNLs with mass ratio r_{N}. The mixing angles $V_{\ell\mathrm{N}}$ are given in the Casas-Ibarra parametrisation with $\omega = 15i$. The centre of mass energy is $\sqrt{s} = 13\,\mathrm{TeV}$.

heavy mass state contribution falls below the light mass states'. For a constant ω, the cross section will consequently always converge with the light mass state line for very m_ν. In case of light enhancement (Fig. B.2b) we note that the combined cross section lies above the single HNL case ($\mathrm{N}_{1,2}$) and the light neutrino case (νs) for $m_{\mathrm{N1}} = 35TeV$, which is likely due to non-trivial cancellations between all four Majorana states involved. However, due to this only happening for mixings at the seesaw line, this curiosity is not relevant for the WBF process.

In Fig. B.3 we see the same cross section for an enhancement factor of $Im(\omega) = 15$. On the m_{N} scales shown here, the plot looks exactly identical to Fig. B.2d, while the absolute scale is about 10 orders of magnitude higher in the $\omega = 15i$ case.

All cases presented in Fig. B.2 have cross sections orders of magnitude below what would be observable at the HL-LHC ($\mathcal{L} = 3\,\mathrm{ab}^{-1}$) or indeed at the FCC ($\mathcal{L} = 30\,\mathrm{ab}^{-1}$). Only a strongly enhanced and sufficiently hierarchical HNL pair in the Casas-Ibarra parametrisation (see Fig. B.3) shows detection prospects. However, as described in Section 2.3, in this limit we enter the regime of the qDL approximation, the analysis of which is presented in Chapter 3.

C Lepton Flavour Violating Amplitudes

As highlighted in this work, lepton number conserving (LNC) but lepton flavour violating (LFV) — unlike lepton number violating (LNV) — processes do not suffer form an intrinsic amplitude suppression. The LFV case, corresponding to the LNV process $W^{\pm}W^{\pm} \to \ell^{\pm}\ell^{\pm}$, would be $W^{\pm}W^{\mp} \to \ell^{\pm}\ell'^{\mp}$. We will briefly present the argument in the following.

Case of a Single Heavy Neutral Lepton

For a single HNL, and single light mass state, the LNC current analog to $J^{\alpha\beta}$ in Section 2.1 is

$$\begin{aligned} K^{\alpha\beta}\left(p, m^2\right) &= \gamma^{\alpha} P_L \frac{\not{p} + m}{p^2 - m^2} \gamma^{\beta} P_L \\ &= \frac{\gamma^{\alpha} \not{p} \gamma^{\beta} P_L}{p^2 - m^2}. \end{aligned} \tag{C.1}$$

Which for LFV in the scenario including the neutrino with mass $-V_{\ell \mathrm{N}} V_{\ell' \mathrm{N}} m_{\mathrm{N}}$ becomes

$$\begin{aligned} &V_{\ell \mathrm{N}} V_{\ell' \mathrm{N}}^{*} K^{\alpha\beta}\left(\not{p}, m_{\mathrm{N}}\right) + K^{\alpha\beta}\left(\not{p}, -V_{\ell \mathrm{N}} V_{\ell' \mathrm{N}} m_{\mathrm{N}}\right) \\ &\qquad = \gamma^{\alpha} \frac{\not{p}}{m_{\mathrm{N}}^2} \gamma^{\beta} P_L \left(\frac{V_{\ell \mathrm{N}} V_{\ell' \mathrm{N}}^{*}}{1 - \left(\frac{p}{m_{\mathrm{N}}}\right)^2} - \frac{1}{1 - \left(V_{\ell \mathrm{N}} V_{\ell' \mathrm{N}}^{*} \frac{p}{m_{\mathrm{N}}}\right)^2} \right) \\ &\qquad = \gamma^{\alpha} \frac{\not{p}}{m_{\mathrm{N}}^2} \gamma^{\beta} P_L \left(-1 + \frac{V_{\ell \mathrm{N}} V_{\ell' \mathrm{N}}^{*}}{1 - \left(\frac{p}{m_{\mathrm{N}}}\right)^2} \right) + \mathcal{O}\left(\left(V^2 \left(\frac{p}{m_{\mathrm{N}}} \right)^2 \right)^2 \right). \end{aligned} \tag{C.2}$$

To first order, such a process is, thus, independent of even the mixing angle, as the numerator of the light neutrino contribution is not suppressed by the light neutrino mass. An HNL around $p^2 \simeq m_{\mathrm{N}}^2$ could become the dominant contribution to this process. Furthermore, for an appropriate complex phase of π between $V_{\ell \mathrm{N}}$ and $V_{\ell' \mathrm{N}}$, the two terms in the last line of Eq. (C.2) add constructively. On the downside, one cannot easily factor out the mixing angle — as commonly done in literature and also in this work — due to non-trivial scaling with VV' (not necessarily clear order between $0, 1, 2$ in $|\mathcal{M}|^2$). It is important to note, that for very large p this expansion breaks down, so that the amplitude does not grow indefinitely as Eq. (C.2) naively suggests.

Case of a Quasi-Dirac-Like Heavy Neutral Lepton Pair

In the case of a qDl HNL pair, the LNC current is

$$\begin{aligned} V_{\ell \mathrm{N}} V_{\ell' \mathrm{N}}^{*} K^{\alpha\beta}\left(\not{p}, m_{\mathrm{N}}\right) + \frac{V_{\ell \mathrm{N}} V_{\ell' \mathrm{N}}^{*}}{r_{\mathrm{N}}} K^{\alpha\beta}\left(\not{p}, r_{\mathrm{N}} m_{\mathrm{N}}\right) \\ = \gamma^{\alpha} \frac{\not{p}}{m_{\mathrm{N}}^{2}} \gamma^{\beta} P_{L} V_{\ell \mathrm{N}} V_{\ell' \mathrm{N}}^{*} \left(\frac{1}{\left(\frac{p}{m_{\mathrm{N}}}\right)^{2} - 1} + \frac{1}{r_{\mathrm{N}} \left(\left(\frac{p}{m_{\mathrm{N}}}\right)^{2} - r_{\mathrm{N}}^{2} \right)} \right) \\ \rightarrow \text{isolated 1 HNL case, for } r_{\mathrm{N}} \gg 1 \\ \rightarrow 2 \times \text{ isolated 1 HNL case, for } r_{\mathrm{N}} \simeq 1. \end{aligned} \tag{C.3}$$

Naively, this seems to suggest that in the Dirac-limit, LFV is allowed. However, it is a well known fact that in this limit SM lepton flavour is conserved due to more subtle cancellations. This can for example be derived by rewriting the seesaw Lagrangian combining the degenerate HNL pair into Dirac particles (c.f. [144]). This means that SM lepton flavour is conserved and deviations can be expected similarly to those in the LNV case.

D Software Usage

The physical observables in this thesis were calculated using the following workflow. The HeavyN package [145, 146] was used as an input for FeynRules [147]. The underlying Lagrangian was then translated into the relevant Feynman diagrams by the FeynArts Mathematica application and translated into an amplitude using the FeynCalc [148–150] application. The consequent manipulations of the amplitude were performed using Mathematica.

The reference cross sections for *pp* level rescaling were generated using the standard HeavyN FeynRules UFO libraries for MadGraph5_aMC at NLO [151, 152].

The Feynman diagrams in this thesis were drawn using the Feynman Diagrams with Ti*k*Z package [153].

E Extra Plots

Suplementary Feynman Diagrams

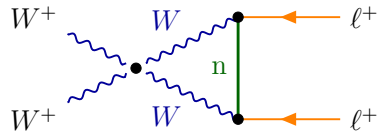

(a) $4W$ vertex

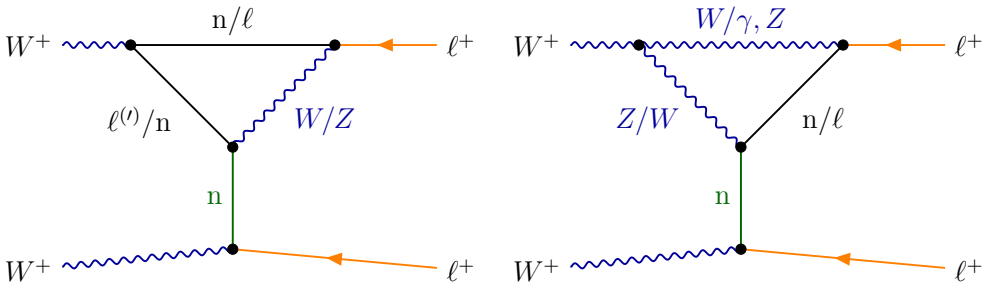

(b) Penguin diagrams

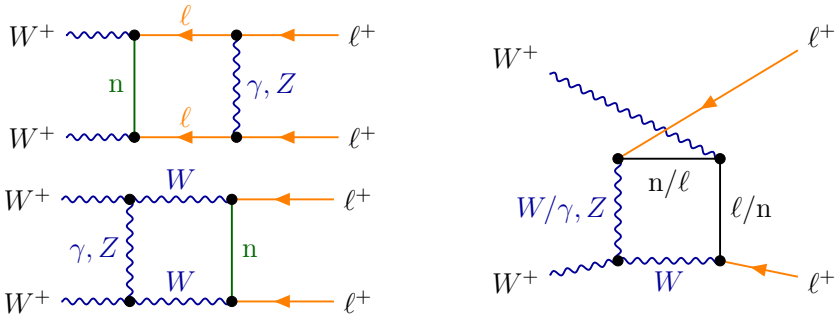

(c) Box diagrams

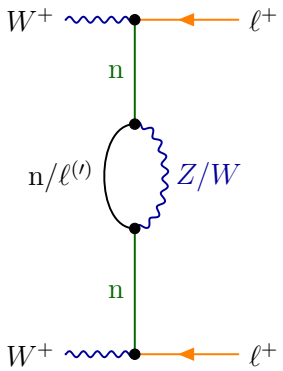

(d) Propagator corrections

Figure E.1: Feynman diagrams of $W^\pm W^\pm \to \ell^\pm \ell^\pm$ in the mass basis at 1-loop order. Here we have omitted trivial symmetry variations of the given diagrams. The fermion number directionality on the black plain lines is implicit. Further, all Z-boson propagators can also be mediated by a higgs.

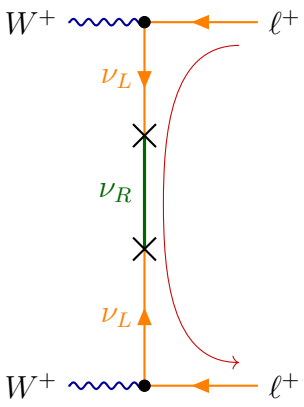

Figure E.2: Feynman Diagram of the two same sign W-bosons to two same sign leptons in the flavour basis to first order in V^2. The crosses mark an oscillation from standard model neutrino to right handed heavy neutral lepton, where the coupling is the Dirac mass $(m_D)_{\ell \mathrm{N}}$.

Observables for Different Parameters

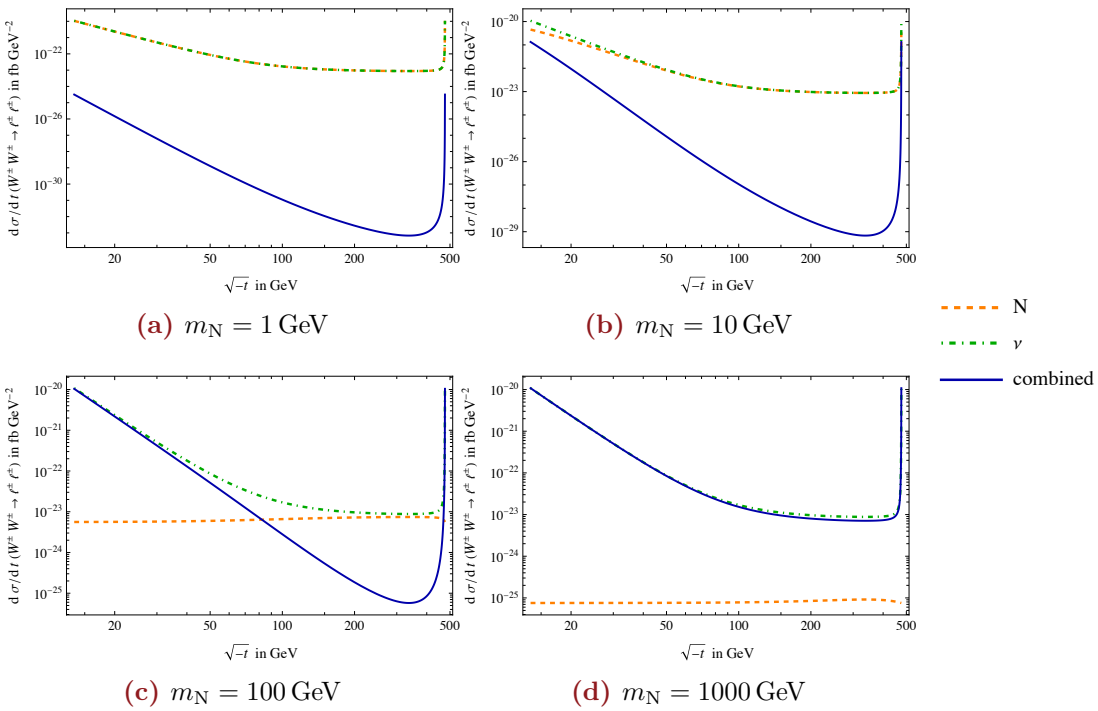

(a) $m_{\mathrm{N}} = 1\,\mathrm{GeV}$ **(b)** $m_{\mathrm{N}} = 10\,\mathrm{GeV}$

(c) $m_{\mathrm{N}} = 100\,\mathrm{GeV}$ **(d)** $m_{\mathrm{N}} = 1000\,\mathrm{GeV}$

Figure E.3: Differential cross section of $W^{\pm}W^{\pm} \to \ell^{\pm}\ell^{\pm}$ scattering in the case of a single HNL at a centre of mass energy of $\sqrt{M_{\mathrm{WW}}^2} = 490\,\mathrm{GeV}$ and for HNL masses m_{N}. The mixing angle here is a function of the HNL mass as well, such that $|V_{\ell \mathrm{N}}^2 m_{\mathrm{N}}| = 1\,\mathrm{eV}$. For further information see Section 2.1.

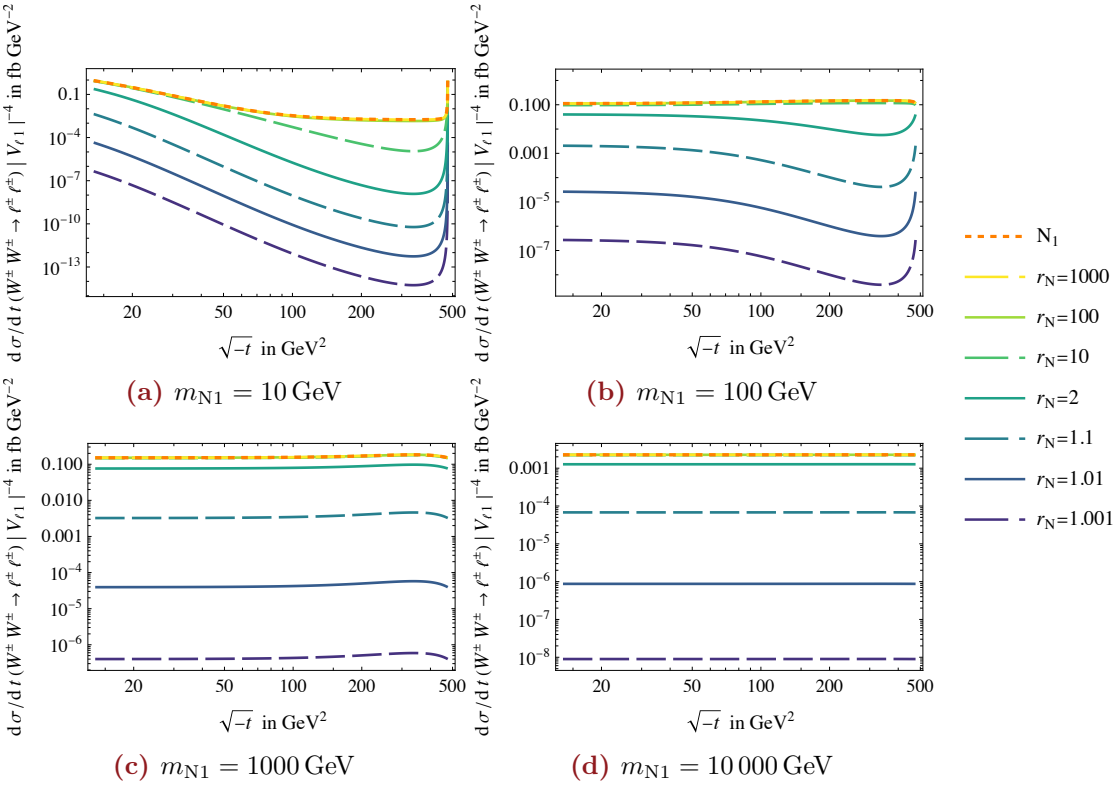

(a) $m_{\mathrm{N1}} = 10\,\mathrm{GeV}$ **(b)** $m_{\mathrm{N1}} = 100\,\mathrm{GeV}$

(c) $m_{\mathrm{N1}} = 1000\,\mathrm{GeV}$ **(d)** $m_{\mathrm{N1}} = 10\,000\,\mathrm{GeV}$

Figure E.4: Total differential cross section of $W^\pm W^\pm \to \ell^\pm \ell^\pm$ scattering with QDL HNL pair with mass ratio r_{N}. at a centre of mass energy is 490 GeV. For further information see Section 2.2.

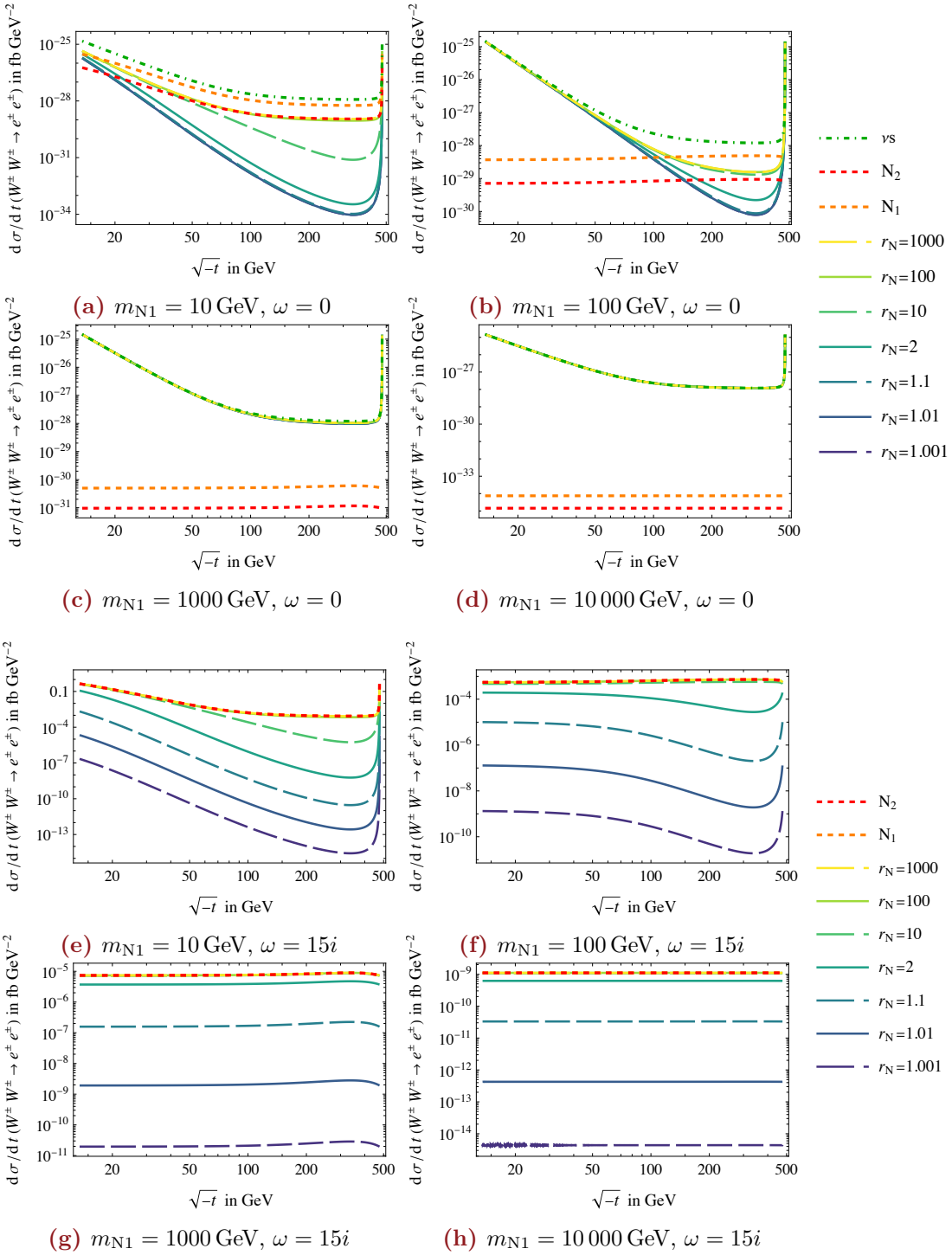

(a) $m_{N1} = 10\,\text{GeV}$, $\omega = 0$ (b) $m_{N1} = 100\,\text{GeV}$, $\omega = 0$

(c) $m_{N1} = 1000\,\text{GeV}$, $\omega = 0$ (d) $m_{N1} = 10\,000\,\text{GeV}$, $\omega = 0$

(e) $m_{N1} = 10\,\text{GeV}$, $\omega = 15i$ (f) $m_{N1} = 100\,\text{GeV}$, $\omega = 15i$

(g) $m_{N1} = 1000\,\text{GeV}$, $\omega = 15i$ (h) $m_{N1} = 10\,000\,\text{GeV}$, $\omega = 15i$

Figure E.5: Total differential cross section of $W^\pm W^\pm \to \ell^\pm \ell^\pm$ scattering, using Casas-Ibarra parametrisation of the mixing angle in case of two HNLs with mass ratio r_N for different lighter masses m_{N1}. Th centre of mass energy is 490 TeV. For further information see Section 2.2.

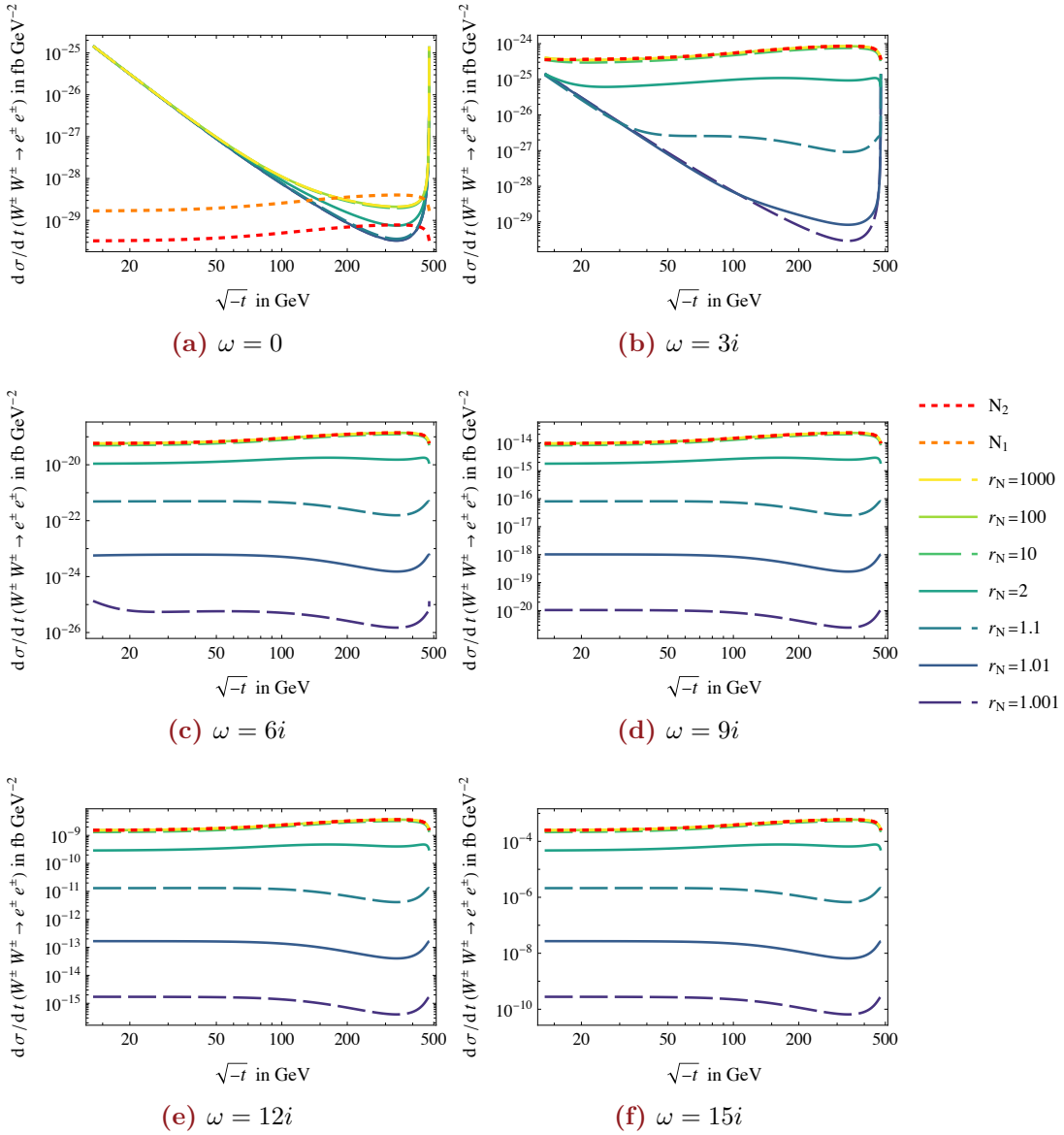

(a) $\omega = 0$ (b) $\omega = 3i$

(c) $\omega = 6i$ (d) $\omega = 9i$

(e) $\omega = 12i$ (f) $\omega = 15i$

Figure E.6: Total differential cross section of $W^\pm W^\pm \to \ell^\pm \ell^\pm$ scattering, using Casas-Ibarra parametrisation of the mixing angle in case of two HNLs with mass ratio r_N for different Casas-Ibarra parameters $\mathrm{Im}(\omega)$. The lighter HNL mass $m_{\mathrm{N}1} = 150\,\mathrm{GeV}$, and centre of mass energy 490 TeV. For further information see Section 2.2.

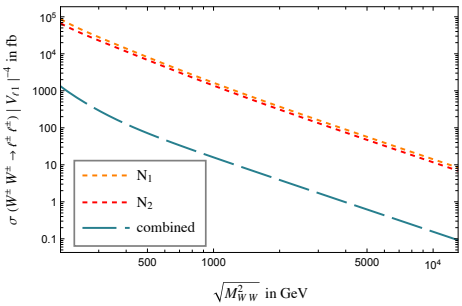

(a) Trans., $m_{\mathrm{N1}} = 150\,\mathrm{GeV}, r_{\mathrm{N}} = 1.1$

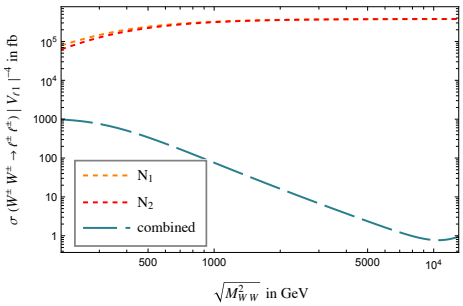

(b) Long., $m_{\mathrm{N1}} = 150\,\mathrm{GeV}, r_{\mathrm{N}} = 1.1$

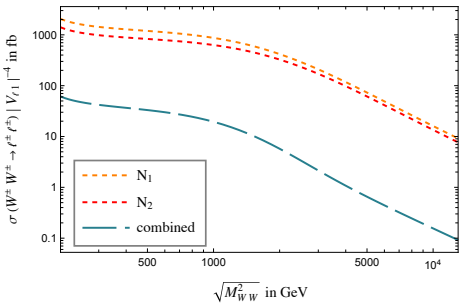

(c) Trans., $m_{\mathrm{N1}} = 1500\,\mathrm{GeV}, r_{\mathrm{N}} = 1.1$

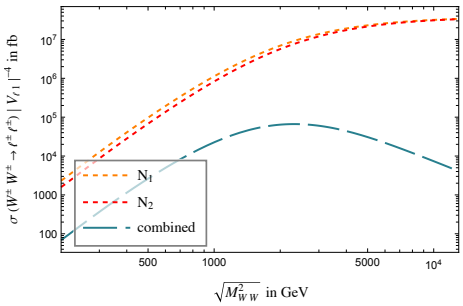

(d) Long., $m_{\mathrm{N1}} = 1500\,\mathrm{GeV}, r_{\mathrm{N}} = 1.1$

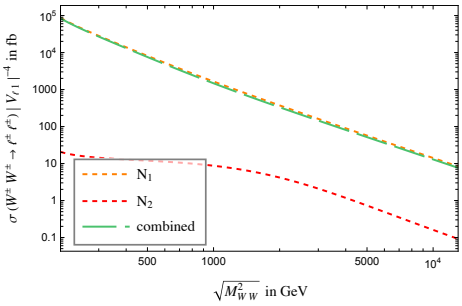

(e) Trans., $m_{\mathrm{N1}} = 150\,\mathrm{GeV}, r_{\mathrm{N}} = 10$

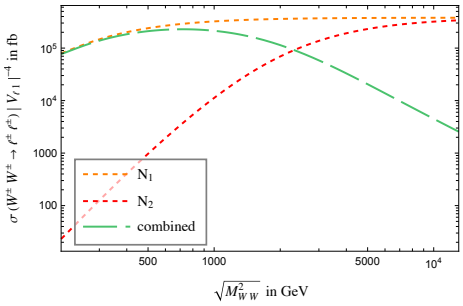

(f) Long., $m_{\mathrm{N1}} = 150\,\mathrm{GeV}, r_{\mathrm{N}} = 10$

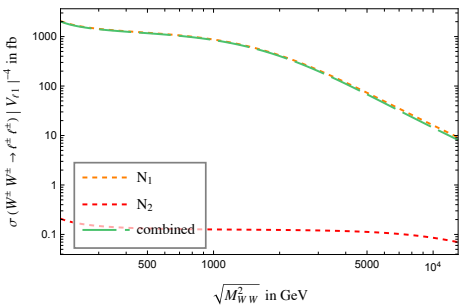

(g) Trans., $m_{\mathrm{N1}} = 1500\,\mathrm{GeV}, r_{\mathrm{N}} = 10$

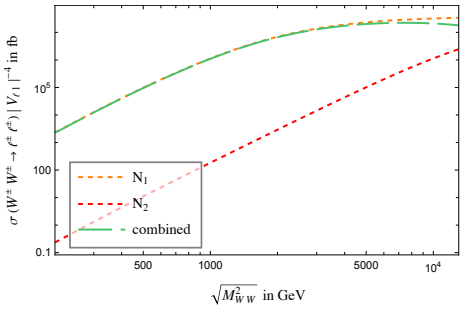

(h) Long., $m_{\mathrm{N1}} = 1500\,\mathrm{GeV}, r_{\mathrm{N}} = 10$

Figure E.7: Polarised cross sections of $W^{\pm}W^{\pm} \to \ell^{\pm}\ell^{\pm}$ scattering as decompositions in the WW polarisations as Trans. $\leftrightarrow \sigma^{\mathrm{TT}}$ and Long. $\leftrightarrow \sigma^{\mathrm{LL}}$. The cross sections are given as a function of the centre of mass energy $\sqrt{M_{\mathrm{WW}}^2}$. The data is given for the lighter HNL mass $m_{\mathrm{N1}} = 150\,\mathrm{GeV}$ (upper) and $m_{\mathrm{N1}} = 1500\,\mathrm{GeV}$ (lower) with the second HNL having a mass according to the mass ratios r_{N}.

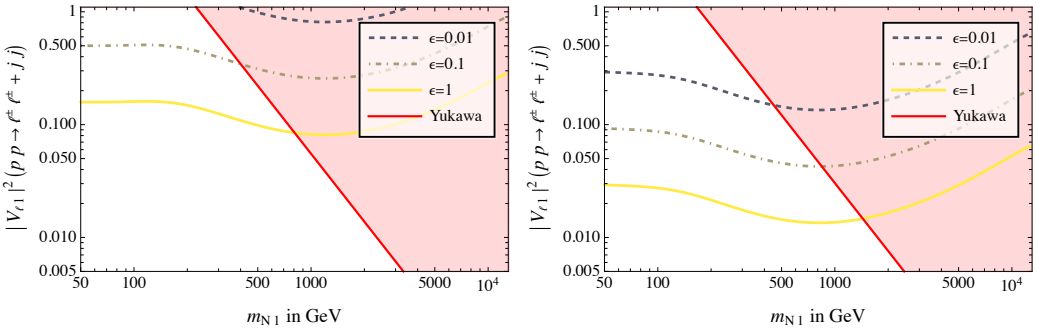

(a) $r_{\mathrm{N}} = 1.1$, $\sqrt{s_{\mathrm{LHC}}} = 13\,\mathrm{TeV}$ **(b)** $r_{\mathrm{N}} = 2$, $\sqrt{s_{\mathrm{LHC}}} = 13\,\mathrm{TeV}$

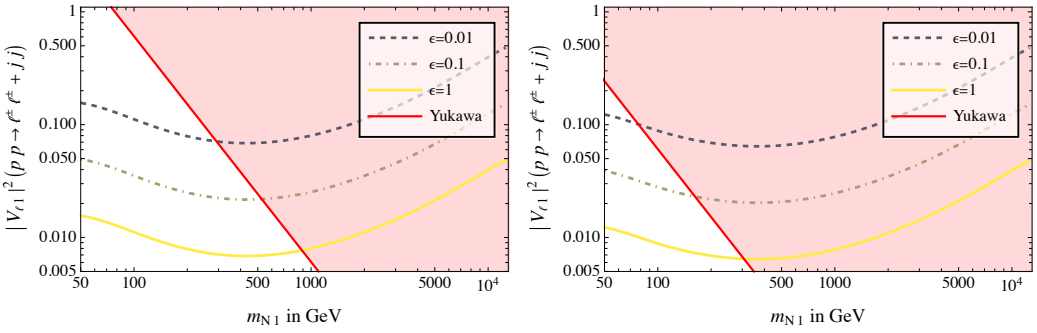

(c) $r_{\mathrm{N}} = 10$, $\sqrt{s_{\mathrm{LHC}}} = 13\,\mathrm{TeV}$ **(d)** $r_{\mathrm{N}} = 100$, $\sqrt{s_{\mathrm{LHC}}} = 13\,\mathrm{TeV}$

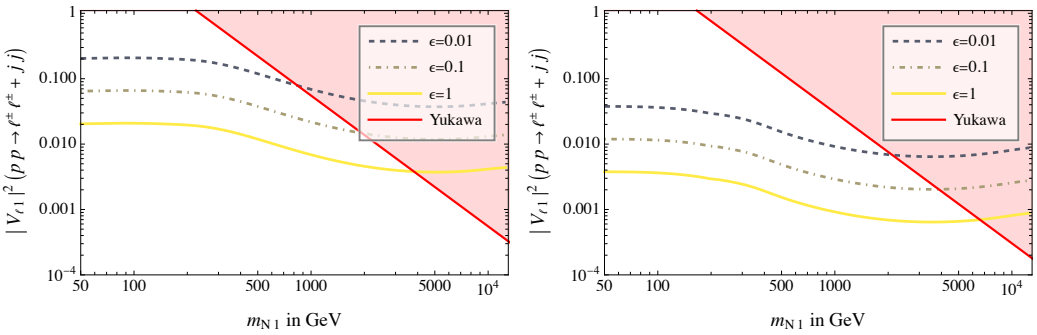

(e) $r_{\mathrm{N}} = 1.1$, $\sqrt{s_{\mathrm{FCC}}} = 100\,\mathrm{TeV}$ **(f)** $r_{\mathrm{N}} = 2$, $\sqrt{s_{\mathrm{FCC}}} = 100\,\mathrm{TeV}$

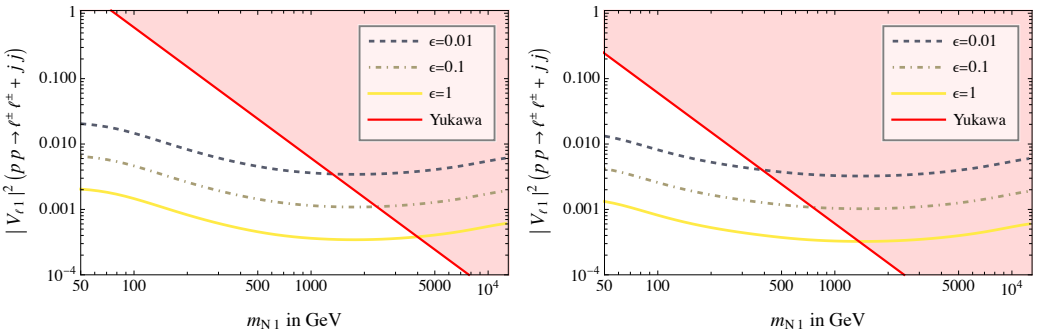

(g) $r_{\mathrm{N}} = 10$, $\sqrt{s_{\mathrm{FCC}}} = 100\,\mathrm{TeV}$ **(h)** $r_{\mathrm{N}} = 100$, $\sqrt{s_{\mathrm{FCC}}} = 100\,\mathrm{TeV}$

Figure E.8: *Optimistic* exclusion limits on the N_1 parameters via VBF-mediated $pp \to \ell^\pm\ell^\pm jj$ events in the model with two HNLs with mass ratio r_{N}. The exclusion limits are 95 % CL assuming zero background. In the upper (lower) plots, the centre of mass energy is $\sqrt{s_{\mathrm{LHC}}} = 13\,\mathrm{TeV}$ ($\sqrt{s_{\mathrm{FCC}}} = 100\,\mathrm{TeV}$) and the luminosity $3\,\mathrm{ab}^{-1}$ ($30\,\mathrm{ab}^{-1}$).